ACADEMIA MILITAR
MILITARY ACADEMY

Performance Assessment of a U-Shaped Dissipative Flat Bar Bending Device for Blast Protection

Tiago José Basílio Ferreira

Thesis to obtain the Master of Science Degree in

Military Engineering

Supervisor(s): PhD Lieutenant-Colonel David Lecompte
PhD Lieutenant-Colonel Pedro José Da Silva Gonçalves Matias

Examination Committee

Chairperson: PhD Prof. Paula Manuela Dos Santos Lopes Do Rego Figueiredo
Supervisor: PhD Lieutenant-Colonel David Lecompte
Member of the Committee: PhD Prof. Hugo Bento Rebelo
Member of the Committee: PhD Prof. Thomas Gasche

November 2023

Declaration

I declare that this document is an original work of my own authorship and that it fulfills all the requirements of the Code of Conduct and Good Practices of the Universidade de Lisboa.

Acknowledgments

This dissertation could not have been completed without the invaluable contributions from a wide array of institutions and people, for which I would like to express my deepest gratitude.

First of all, I extend my profound thanks to Lieutenant Colonel of Military Engineering Pedro Matias, whose generosity provided me with a remarkable opportunity and paved the way for the establishment of crucial connections that made this academic exchange possible.

I also which to express my gratitude to Lieutenant Colonel David Lecompte, my scientific advisor, for his valuable guidance and advice he extended throughout this project. Your availability, support, counsel, and the combination of your technical and human qualities have been instrumental in shaping this work.

I would like to express my heartfelt gratitude to Pedro Basto for his continuous availability and support during the thesis, as well as for his diligent efforts and unwavering commitment that significantly contributed to the success of this research.

I would like to express my appreciation to Aldjabar and Mohamed for their cooperation, camaraderie, and readiness to assist, especially during the planning and execution of the experimental phase, without which this would not have been feasible.

I would also like to extend my sincerest thanks to Bachir Belkassem, who consistently sought to actively engage with me through his thoughtful ideas and proposals. Your encouragement and contributions have been duly recognized and appreciated. Also, my sincerest thanks for your help with designing and preparing the pieces necessary for the experimental campaign. Without it, it would have not been possible.

Special thanks are also extended to Miguel Chambino for his companionship and support during my time in Belgium, making it a more pleasant and enjoyable experience.

To all the dedicated individuals within the Department of Military and Protective Engineering at the Royal Military Academy in Belgium, I offer a heartfelt thanks for your help, camaraderie, and support.

Finally, my deepest thanks to Catarina for her unconditional and emotional support, especially during the most difficult and stressful times, for never ceasing to believe in me, and for giving me the last push to finish and deliver this dissertation, thank you.

Abstract

Commercial ”shipping containers” have brought about a revolution in military logistics. Initially recognized as being a primary method for shipping supplies and materiel, these structures can be adapted to improve living conditions for soldiers during operations.

The increase of terrorist attacks and the high use of explosive devices as a weapon type makes the investigation of blast-resistant solutions for structures based on energy-dissipating methods important given that it can protect the occupants and contents from blast effects and allow rapid repair and reoccupation after an explosive attack.

This dissertation focuses on the study and characterization of an energy dissipative device denominated U-shaped dissipative flat bar bending device (UFBD) subject to blast loading conditions. This device is part of a design of a protective solution developed for ISO containers to mitigate the amount of energy released from a blast event, minimizing the damage to the container allowying a faster recovery of full functionality after an extreme event.

The UFBD is composed of a mechanism box with a pin inside and a flat bar which is positioned in direct contact around the pin. When a force is applied, the flat bar is forced to bend around the pin, dissipating energy through plastic deformation. The study and characterization of the UFBD subject to blast loading conditions were carried out through an experimental test campaign and numerical modelling in the LS-Dyna software.

The blast loading experimental campaign and the numerical simulations proved that the UFBD has the potential to work as an energy absorber device for blast loading conditions. It was verified that the flat bar moved around the pin and deformed as expected. The ability to dissipate energy through plastic deformations was validated through the plastic deformation of the flat bar after the blast.

Keywords: U-shaped dissipative flat bar bending device (UFBD); plastic deformation; experimental test campaign; numerical modelling; energy absorber; blast mitigation.

Resumo

Os ”contentores marítimos” comerciais provocaram uma revolução na logística militar. Inicialmente reconhecidos como valiosos a nível logístico, sendo um método primário para o transporte de abastecimento e material, estas estruturas podem ser adaptadas para melhorar as condições de vida dos soldados durante as operações.

O aumento dos ataques terroristas e a elevada utilização de engenhos explosivos como arma típica torna importante a investigação de soluções resistentes à explosão para estruturas baseadas em métodos de dissipação de energia que possam proteger os ocupantes e o conteúdo dos efeitos da explosão e permitir uma rápida reparação e reocupação após um ataque explosivo.

Esta dissertação centra-se no estudo e na caraterização de um dispositivo dissipativo de energia denominado dispositivo dissipativo de flexão de barras planas em forma de U (UFBD) sujeito a condições de carga de explosão. Este dispositivo faz parte do projeto de uma solução de proteção desenvolvida para contentores ISO para mitigar a quantidade de energia libertada por um evento de explosão, minimizando os danos no contentor e permitindo uma recuperação mais rápida da funcionalidade total após um evento extremo.

O UFBD é composto por uma barra plana de alumínio e uma caixa de mecanismo com um pino no interior, sendo a barra plana posicionada em contacto direto à volta do pino. Quando é aplicada uma força, a barra plana é forçada a dobrar-se em torno do pino, dissipando energia através de deformação plástica. O estudo e a caraterização do UFBD sujeito a condições de carga de explosão foram efectuados através de uma campanha de ensaios experimentais e de modelação numérica no software LS-Dyna.

A campanha experimental de carga de explosão e as simulações numéricas provaram que o UFBD tem potencial para funcionar como um dispositivo de absorção de energia para mitigação de explosões. Verificou-se que a barra plana se movia em torno do pino e se deformava como esperado. A capacidade de dissipação de energia através de deformações plásticas foi validada através da deformação plástica da barra plana após a explosão.

Palavras-chave: Dispositivo dissipativo de flexão de barras planas em forma de U (UFBD); deformação plástica; campanha de ensaios experimentais; modelação numérica; absorção de enrgia; mitigação de explosões.

Contents

List of Figures

List of Tables

Nomenclature

Greek symbols

α	Angle of incidence
$\bar{\varepsilon}^{p^n}$	Effective plastic strain
β	Hardening coefficient
$\dot{\varepsilon}$	Strain rate
ϵ_p	Effective plastic strain
ϵ_p/ϵ_0	Normalized plastic strain
ϵ_d	Densification phase or densification strain
ϵ_y	Elastic phase
ν	Poisson's ratio
ρ	Density of the material
σ_0	Reference yield stress
σ_0	Plateau Stress or reference yield stress
$\sigma_y(\varepsilon^p_{eff}, \dot{\varepsilon}^p_{eff})$	Dynamic yield stress
$\sigma^s_y\left(\varepsilon^p_{eff}\right)$	Yield stress computed from the sum of the static stress
ε	Equivalent plastic strain
ε^p_{eff}	Effective plastic strain
ε_{ref}	Strain reference
$\dot{\varepsilon}^*$	Normalized effective strain rate
$\dot{\varepsilon}^p_{eff}$	Strain rate

Roman symbols

A	Model parameter

B Model parameter

b Decay wave coefficient

C Model parameter or Strain rate parameter of the Cowper-Symonds model

C_r Reflection coefficient

E Elastic modulus

E_t Tangent modulus

H^d_{EXP} detonation energy of the explosive considered

H^d_{TNT} Detonation energy of TNT

i_s Impulse of the positive phase

i_s Impulse

i_s^- Impulse of the negative phase

i_s^- Negative impulse

L_1 Model parameter

L_2 Model parameter

m Model parameter

n Model parameter

P Strain rate parameter of the Cowper-Symonds model

P_0 Atmosphere pressure

P_r Reflected overpressure

P_{so} Peak incident overpressure

P_{so}^- Minimum value of pressure

Q_1 Model parameter

Q_2 Model parameter

q_s Drag load

R distance between the structure and the center of the explosive charge

R_A distance from the affected surface

$SIGY$ Yield stress

T Material toughness or material temperature

t Time

T_0 Room temperature

t_0 Positive phase duration

t_0^- Negative phase duration

t_A Time necessary for the shock wave to reach the element

T_m Melting temperature

T_r Room temperature

W Weight of the explosive charge

W_{EXP} Weight of the explosive considered

W_{TNTe} TNT equivalent weight

Z Scale distance

Subscripts

i Computational index

ref Reference condition

Acronyms

BRWB Blast-resistant wood building

BUT Bending under tension

CBT Continuous bending under tension

DIC Digital Image Correlation

DLG Deflagration load generator

EDCAs Energy-dissipating component assemblies

EDST Explosive driven shock tube

FVDs Fluid viscous dampers

IED improvise explosive devices

ISO International Standards Organization

LPG Liquefied Petroleum Gas

RHS Rectangular hollow sections

ST Simple tension testing

TNT Trinitrotoluene explosive

UFBD U-shaped dissipative flat bar bending device

UFC Unified Facilities Criteria

VBIED Vehicle-borne improvised explosive devices

Chapter 1

Introduction

1.1 Context and motivation

Much like their impact on global commercial logistics, commercial ”shipping containers” have revolutionized military logistics. Even today, more than forty years after the International Standards Organization (ISO) standardized their sizes, military logistics operations continue to benefit not only from the movement of internal supplies but also from a wide array of enhanced and specialized applications of containerized systems designed to match the standard ”container-sized” specifications [1].

The use of ISO containers by the military was firstly recognized as a logistic value and evident in the 1990/1991 Operations Desert Shield/Desert Storm, during which ISO containers were a primary method for shipping supplies and materiel. Evidence of the ”container contribution” was reported by a General Accounting Office at that time at the completion of Operation Desert Storm, the Department of Defense (DoD) faced the overwhelming task of returning about 35 000 containers of materiel to supply depots and units in the United States and Europe [1].

Later, an effort was made for dedicated containers to transport and deploy tactical or support capabilities and, in 1991, the Army’s ”Force Provider” concept, now referred to as Force Provider Expeditionary (FPE), was created to improve living conditions for soldiers during Operations Desert Shield/Storm. It can provide food facilities, hygiene services, climate-controlled billeting, and morale and recreation facilities for military personnel in field locations (Figure 1.1) [1].

(a) Quadcon container at Kin Red Port, Okinawa.

(b) TRICON Kitchen System,container-based all-electric kitchen.

Figure 1.1: The use of containers in the military environment [1].

Recently, the use of containers has been visible in the military environment in Central African Republic (RCA). In some cases, the accommodation of newly arriving personnel is in the form of containerized accommodation inside the MINUSCA camps (Figure 1.2). The containerized accommodation normally has an individual bathroom with 24/7 running water, electricity, and wifi [2].

Figure 1.2: Containers used in Camp Moana where the MINUSCA units are located.

Terrorist attacks frequently target military structures like barracks, combat vehicles, and civilian buildings of significant importance. Therefore, it is reasonable to anticipate that these tragic incidents may occur during peacetime or in theaters of operation.

Terrorism attacks have been perpetuated over the years (Figure 1.3). Although the number of terrorist attacks decreased by 28% from its peak in 2015, terrorist attacks have become more deadly in 2022, killing on average 1.7 people per attack in 2022 compared to 1.3 people per attack in 2021, registering the first increase in lethality in five years (26 percent more people per attack) [3].

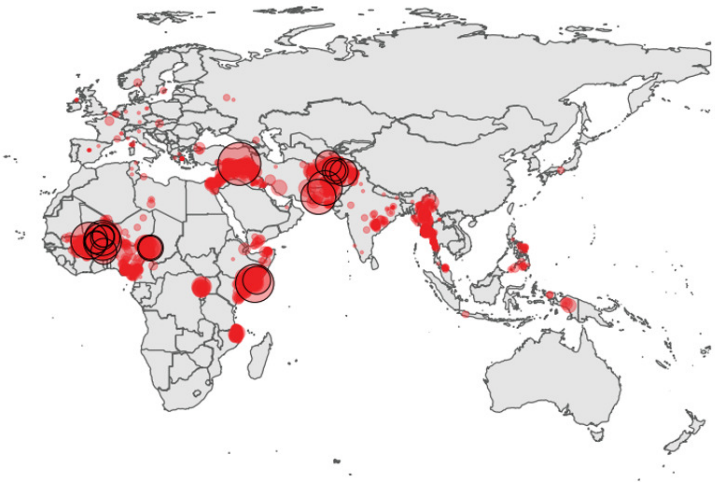

Figure 1.3: Terrorist incidents map [3].

According to Figure 1.4, the main mechanism used for terrorism attacks are mainly explosives, which can guarantee a big amount of damage to structures and human lives.

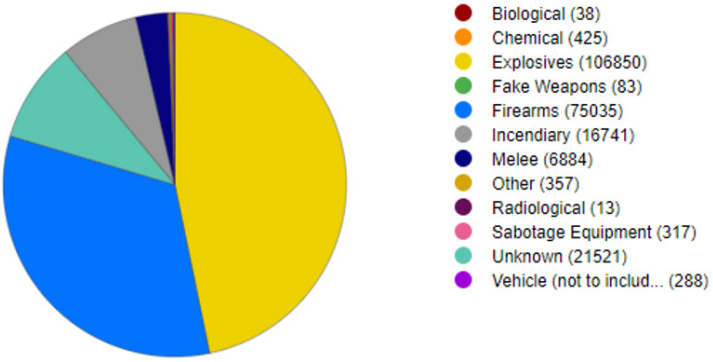

Figure 1.4: Weapon type in terrorism attacks [4].

Apart from terrorism attacks, the risk of accidental explosions is also a reality. One example is the massive chemical detonation on August 4, 2020, in the Port of Beirut, Lebanon (Figure 1.5). The port of Beirut is one of the largest ports in the Middle East with a 1.2 km^2 area of terminals for passengers, general cargo, and containers, and is a strategic geographic location at the nexus of three continents: Europe, East Asia, and Africa. An uncontrolled fire in an adjacent warehouse triggered an explosion involving approximately 2,750 tons of Ammonium Nitrate, resulting in one of the most catastrophic blasts in recent memory, causing immediate injuries to more than 6,500, while inflicting severe damage on the densely populated residential and commercial zones nearby [5].

Figure 1.5: Explosion of Beirut.

As is evident from the ongoing global terrorist threat, which increasingly employs explosives as an attack weapon, and the accidental explosion in Beirut, it is clear that there are threats present in both military and civilian environment. Consequently, engineers and government authorities face an ongoing challenge in their efforts to reduce these threats and develop more effective solutions for safeguarding structures against the destructive impact of explosions.

The concept of protection is far from being absolute. There are situations in which it is possible to find a balance between the level of protection and the cost, seeking to obtain an optimal result. In some cases, certain losses may be considered minor when weighed against the potential loss of human lives, underscoring their significance. To establish a suitable level of protection, a comprehensive risk assessment is crucial, encompassing several key factors: the type of threat, the probability of an attack or accident, and the resulting consequences. Furthermore, it is imperative to clearly identify the response of both civilian and military structures (such as train stations, airports, combat vehicles, etc.) when subjected to blast loads [6].

For many buildings, particularly critical infrastructure (ex: power plants, water treatment works, hospitals), the ability to sustain operations after an explosive attack is essential. Conventional approaches to fortifying structures are frequently characterized by high design and construction costs, making them unsuitable for enhancing existing buildings. The incorporation of energy-dissipating methods within a modular system holds the potential to protect the occupants and contents from blast effects and allow the rapid repair and reoccupation after an explosive attack [7].

The research for a energy-dissipating method that can offer protection for a ISO container by absorbing energy from a blast load alloying a fast recovery after the event is the motivation of this Master dissertation.

1.2 Background work

One mechanism that has shown good results to work as a dissipative device for blast loading is the energy-dissipating component assemblies (EDCAs) [7, 8]. The concept is based on the creation of panels connected to a steel frame compliant with the ISO container standards using the EDCAs. When the blast occurs, the panels may deform and the energy from the blast is transferred to the EDCAs, which extend and plastically deform, limiting the energy transferred to the structure. The steel frame needs to be designed to resist the blast loads and the EDCAs and panels need to be replaced after the blast since the main structure is supposed to stay undamaged (Figure 1.6) [8, 9].

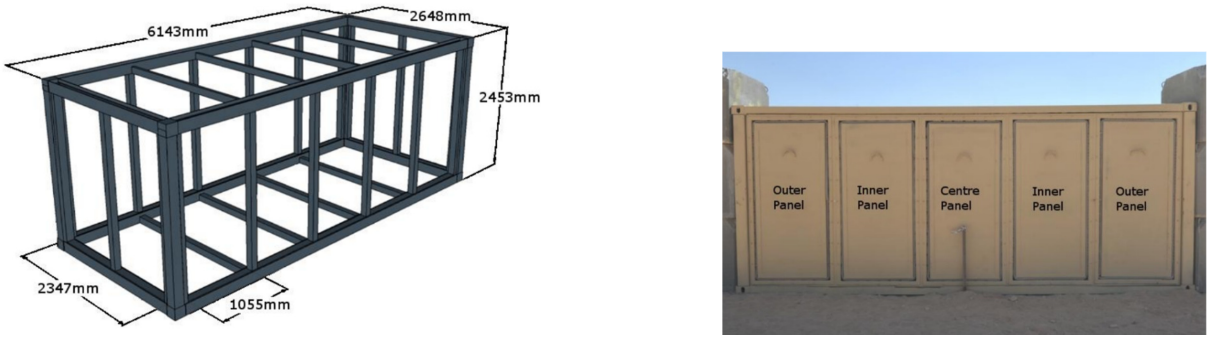

(a) Steel frame compliant.

(b) ISO container made of front panels and a steel frame compliant.

Figure 1.6: Concept idea for an ISO container obtained from [7, 8].

Basto [10] build on the EDCA concept and proposed a different solution for a dissipative system for the general concept. This new system created by Basto relies on front panels and a steel frame compliant [7] with the ISO container standards. The concept is not new but rather builds on the designs already proposed in existing literature [7, 8] (Figure 1.6), namely on the EDCAs. In Baston's solution the front panels have no structural purpose and are supposed to have a blast and ballistic resistance. Conceptually, the system works by adding a net of horizontal flat bars behind the panels, each one connected to two mechanism boxes with a pin inside. The end of the flat bar is bent over a pin inside the mechanism box, rigidly installed on the steel structure, so the flat bars do not move without an applied force. The panels are rigidly connected to the net of the flat bars locked by the pin and simply supported by the steel structure (Figure 1.7). When exposed to the blast load, the deformation of the panels will induce plastic deformation of the net of horizontal bars, transforming the kinetic energy of the blast into energy associated with plastic deformation [10]. The consideration of a single flat bar connected to a single mechanism box by a single pin is referred in this work as the U-shaped dissipative flat bar bending device.

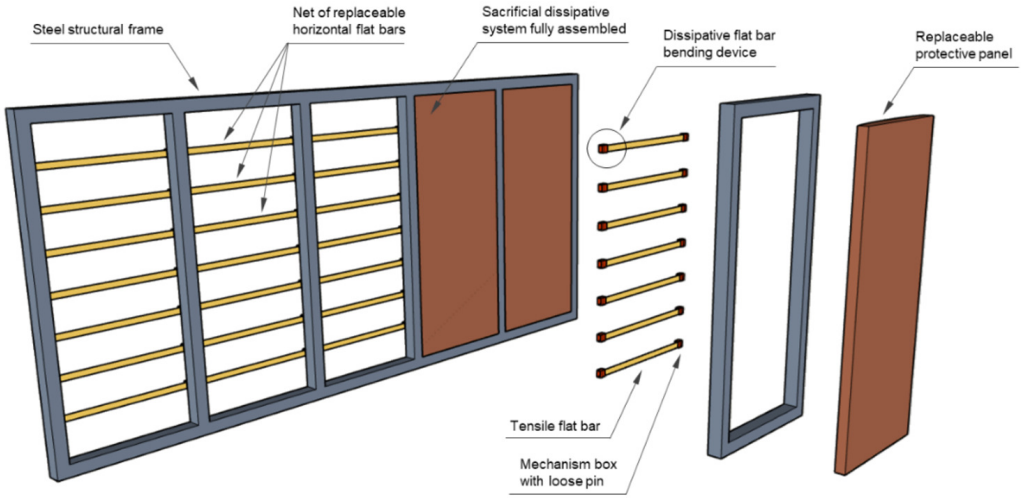

Figure 1.7: Schematic of the protective panel system concept [10].

The concept behind the U-shaped dissipative flat bar bending device (UFBD) is the ability to convert the kinetic energy from a blast wave into plastic deformation energy. The UFBD for blast protection was designed with the purpose of a faster recovery of full functionality after the occurrence of an extreme event due to blast loading by improving the capacity of being easily replaceable. Also, the relatively low mass compared to other systems is another particularity considered in the design of this system [10].

To be less expensive and easier to manufacture and maintain, the proposed system uses only commercially available materials that can be found in any general construction. As a result, a design with commercially available standard steel sections was considered only requiring minor additional work on cutting and bending work. The material considered for the design is the S235 standard steel [10].

The UFBD is composed by three separate components with the following geometries (Figure 1.8):

- Mechanism box: RHS 60x40x4 mm^3 with a length of 60 mm (EN 10219-1/2);
- U-shaped flat bar, 3 options: 50x4, 50x3 and 40x3 mm^2 (EN 10058);
- Loose pin: rod Ø10 mm (EN 10060).

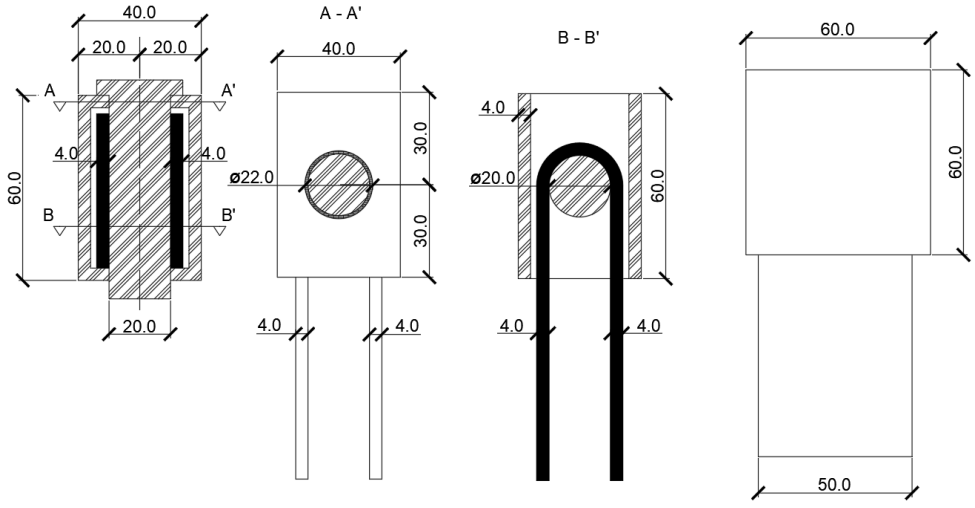

Figure 1.8: Preliminary design of the Dissipative Flat Bar Bending Device [10].

1.2.1 Description of the UFBD and preliminary design

According to José Basto [10], the force required to initiate the unbending/bending mechanism is called the plateau force F_{plt}. It is applied to the U-shaped flat bar creating two plastic hinges formed simultaneously in the opposed initial curved sections of the U-shape (immediately after the contact between the bar and the loose pin axis), described in Figure 1.9.

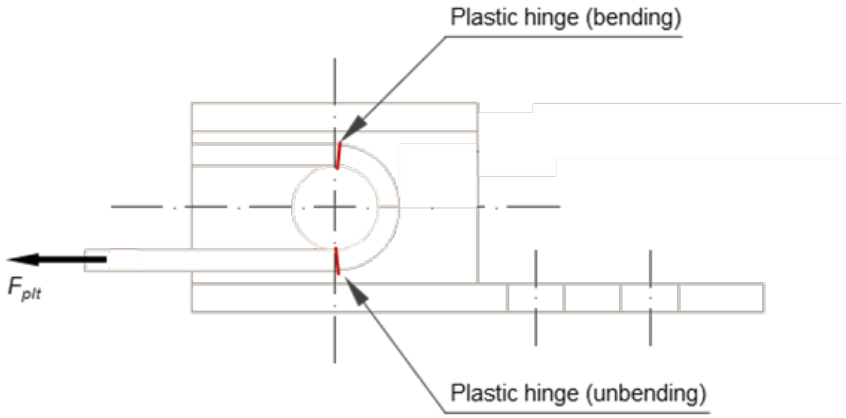

Figure 1.9: Design model of the mechanism box [10].

The system considers a gap between the U-shaped flat bar and the mechanism box on the loose side. It is admitted that the bending only occurs when contact between the bar and the mechanism box wall is reached, forcing the bar to conform to the bending mechanism, whereas the unbending starts immediately after the first plastic hinge is formed. After the initial stage of the bending/unbending mechanisms, both plastic hinges are assumed to occur simultaneously [10].

1.2.2 Proof of concept results

A proof of concept experimental campaign was conducted by Basto [10] in order to initially characterize the behavior of the U-shaped dissipative flat bar bending device. Quasi-static tests considering different load conditions were conducted using standard laboratory tensile test equipment (Figure 1.10). Different loading speeds ranging from 10 to 50 cm/min were considered and the resultant standard force and displacement were measured. Lubrification between the pieces in the mechanism box was used in order to obtain consistent results for the load-deformation curve. It is also admitted that lubrification is always a part of the basic maintenance of a steel mechanism against corrosion.

Figure 1.10: Testing set-up [10].

For the laboratory tests, different U-shaped flat bar geometries (50x4, 50x3, and 40x4 mm^2) were tested considering different loading speeds ranging from 10 to 50 cm/min. The experimental results can be found in Appendix A. It was possible to observe from the experimental results that the load-displacement curve presents a typical elastic-plastic behavior, as expected, typical of a Type I structure, which is characteristic of a dissipative device [10]. The load-displacement curves display a good consistency among the tests.

A numerical model of the UFBD was also developed using LS-DYNA software. The geometry considered for the numerical model is the same used for the experimental campaign, using only the 50x4 mm^2 U-shaped flat bar cross-section dimensions. A comparison of the numerical results resulting from an explicit analysis with the experimental results for a 50x4 U-shaped flat bar specimen is illustrated in Figure 1.11.

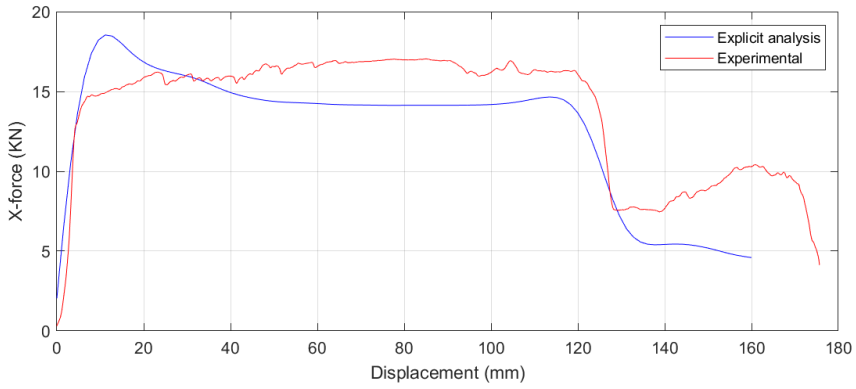

Figure 1.11: Comparison of the numerical results with the experimental results of 50x4 U-shaped flat bat specimen (Adapted from [10]).

The curve resulting from the numerical results is considered to have, in generally, a good correlation

with the experimental results, describing a clear initial elastic region and plastic plateau region, as well as the decrease in peak of the load to around 50% of its value after the displacement of 120.0 mm. An initial peak of force is noticed in the numerical results that are not observed in the experimental results. In the plastic plateau region, the numerical results underestimate the resultant force by 17.6% [10].

The UFBD describes a behavior typically of a dissipative device validated by the quasi-static tests performed in the experimental campaign. However, when considering dynamic tests, the high-speed plastic deformation of material could differ significantly from quasi-static collapse, and the UFBD could not work, or the behavior can be different from that of a dissipative device. Due to that fact, further investigation regarding the characterization of the UFBD for dynamic conditions is needed and is the objective for this master dissertation.

1.3 Objectives and Methodology

The main objective of this master dissertation is to study a single flat bar connected to a single mechanism box, designated as U-shaped Dissipative Flat Bar Bending Device (UFBD), subject to blast loading conditions. To this end, numerical and experimental studies are conducted to achieve the proposed objective. The methodology outlined for this study involves conducting laboratory-scale experiments to obtain initial experimental data, which can complement Basto's work on UFBD characterization. In the initial stage, a numerical analysis of the UFBD's behavior is carried out, taking into consideration Basto's experimental findings and the numerical model he presented. Taking into account specific considerations for experimental blast loading tests, an adapted UFBD is prepared for testing. Subsequently, a dedicated numerical model is developed to evaluate the modified UFBD's response to blast loads. Finally, the adapted UFBD undergoes laboratory testing to validate the numerical results and its performance when subjected to blast loads.

1.4 Dissertation Outline

The present dissertation is divided in seven chapters. The first chapter refers to the background, motivation, and organization of this master dissertation.

The second chapter presents the characteristics of the explosion and blast loading characterization. Considering that this dissertation involves experimental tests using explosive charges, it is essential to have a comprehensive understanding of explosion behavior and the methods for characterizing it.

The third chapter provides a concise literature review of energy dissipation systems for ISO containers. It also offers a brief overview of energy absorption device classification and characterization. Additionally, it touches on the study of material strain rate effects during plastic deformation and important factors to consider in UFBD characterization. The classification and characterization of the UFBD are essential for studying and comprehending its operation, which is necessary to fulfill the proposed objectives for this master's dissertation.

The fourth chapter describes the procedures for studying the UFBD and all the considerations taken to test it for blast loads. The development of the numerical and experimental part is based on the considerations taken in this chapter.

The fifth chapter addresses the numerical investigation of the UFBD's behavior, using Basto's experimental results as a reference. Various modifications to the numerical model presented by Basto are examined to validate a numerical model capable of meeting the objectives outlined in this thesis. Subsequently, a numerical model is developed to assess the UFBD's performance under explosion loads, building upon the prior adaptations. The results obtained from this chapter are subsequently validated through the experimental tests detailed in the following chapter.

The sixth chapter outlines the experimental results conducted to validate the proposed device's performance under blast loads. This chapter covers tensile tests, quasi-static tests, and blast loading tests, all of which serve to validate the numerical work conducted in the preceding chapter.

The seventh chapter presents the conclusions drawn from this work and outlines some proposals for future research in the field of UFBD.

Chapter 2

Explosion and blast loading characterization

2.1 Definition and classification

2.1.1 Definition

An explosion can be defined as a rapid, large-scale, and sudden release of energy [11]. Also, it can be defined as a result of a high and fast increase of pressure and temperature and a release of gases under pressure resulting in a pressure wave that can interact with the material around by moving them [12].

Considering their nature, an explosion can be classified as physical, nuclear, or chemical. A physical explosion can be formed by the releasing energy of mixing two different liquids at different temperatures, volcanic eruptions, and a sudden release of energy caused by the bursting of a container with gas under pressure. A nuclear explosion is caused by the formation of different atomic nuclei. The interaction by redistributing protons and electrons between them causes a huge release of energy. A chemical explosion can be defined simply as a fast oxidation of fuel elements such as carbon and hydrogen atoms [11].

A chemical explosion can also be classified by its propagation velocity as deflagration at subsonic velocity and as a detonation at supersonic velocity [12]. In the case of deflagration, the diffusion of heat during the reaction causes the propagation of deflagration waves. An explosion by detonation is characterized as a shock wave supported by a flame due to shock-induced heating, which propagates at a supersonic velocity and is characterized by a high-pressure level that can move, change, or shatter nearby materials [12, 13].

For the present dissertation, the explosion by detonation was selected as blast load type. This is the characteristic explosion of military grade explosives and explosive ordinance (e.g. artillery and mortar shells) as well as improvise explosive devices (IED), used either against military forces as for terrorism purposes.[14]. The blast load characterization for the detonations is described in the next section.

2.1.2 Classification

According to the UFC 3-340-02 [15], an explosion can be classified according to its confinement degree and relative location from the target structure. Table 2.1 shows the different scenarios that can be considered.

Table 2.1: Types of explosions according to their confinement degree/location (Adapted from [15]).

Types of explosions	**Confinement degree/Location**
Confined or inside explosions	Fully vented explosions Partial vented explosion Fully confined explosion
Unconfined explosions or outside explosions	Free air burst explosion Air burst explosion Surface burst explosion

The confined or inside explosions can be defined as totally vented, partially confined, and totally confined. When considering an explosion inside a building, the pressures related to the initial shock wave tend to suffer an amplification due to the reflection phenomenon inside the structure. Also, an increase in pressure and increase of time during the structure solicitation can occur due to the confinement degree given by the structure, due to the high level of temperatures, and also due to the accumulation of gases resulting from the chemical reaction [16, 17].

A fully vented confined explosion occurs when one or more surfaces are exposed to the atmosphere, originating a blast wave that tends to propagate out of the confinement, and the shock wave is almost immediately vented [16].

A partial vented or partial confined explosion occurs when a structure has all its surface exposed to the atmosphere. In this case, the initial shock wave tends to be vented to the atmosphere after a certain period [16].

A fully confined explosion occurs when there is no contact between the initial shock wave and the atmosphere due to the structure configuration [16].

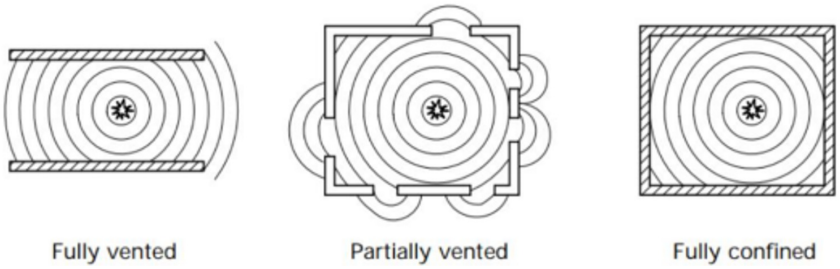

Figure 2.1: Types of confined explosions (Adapted from [16]).

Unconfined explosions can be classified according to their relative position as free air burst, air burst, and surface burst explosions. A free air burst explosion occurs above the ground, and the shock wave doesn't suffer from any type of amplification until it reaches the surface of the building [14]. In air burst explosion, due to the height that the detonation occurs in relation to the ground, some intermediate reflections occur when the shock wave reaches the ground before reaching the building [6]. A phenomenon

denominated as Mach wave, with higher pressures than double the initial shock wave pressure, occurs when the velocity of the reflected wave is higher than the initial one, overlapping with it and propagating together [14, 16].

In a surface burst explosion, a planar incident pressure can be considered before contact with the structure since the initial wave in contact with the ground is reflected and amplified, creating a reflected wave [14, 16].

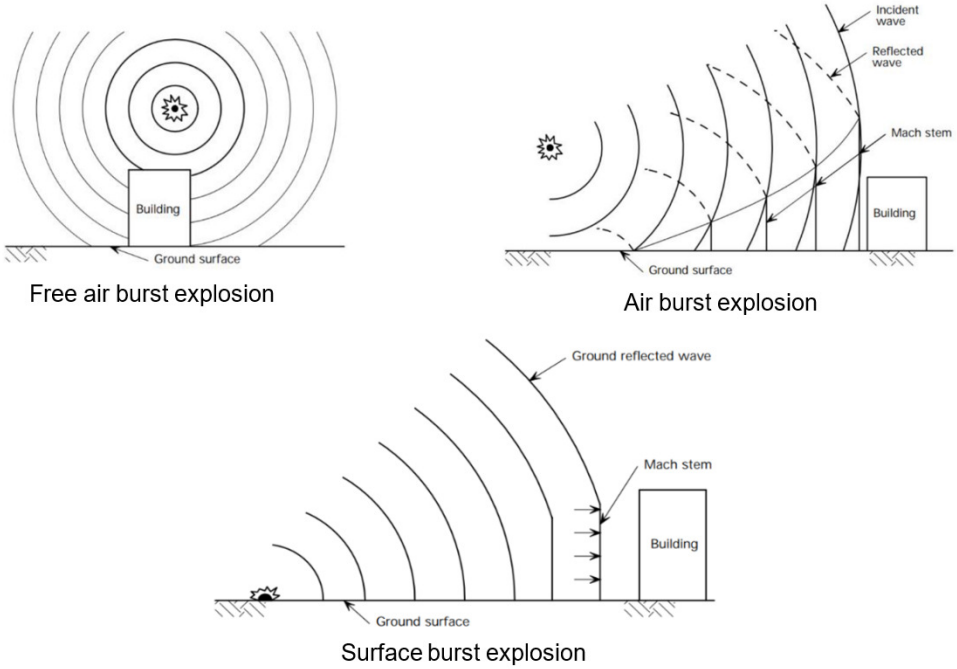

Figure 2.2: Types of unconfined explosions (Adapted from [16]).

2.2 Shock wave characterization

2.2.1 Pressure-time profile

The detonation of an explosive material (liquid or solid) produces a violent and rapid chemical reaction, which converts into a highly dense, pressurized, and warm gas. The expansion of resultant material from the explosion expands at high speeds intending to reach equilibrium with the surrounding atmosphere. This phenomenon produces a shock wave that is characterized by supersonic velocity propagation and radial form of extremely compressed air [18, 19]. Figure 2.3 shows a blast wave's typical pressure profile in time for a point submitted to a free air burst explosion.

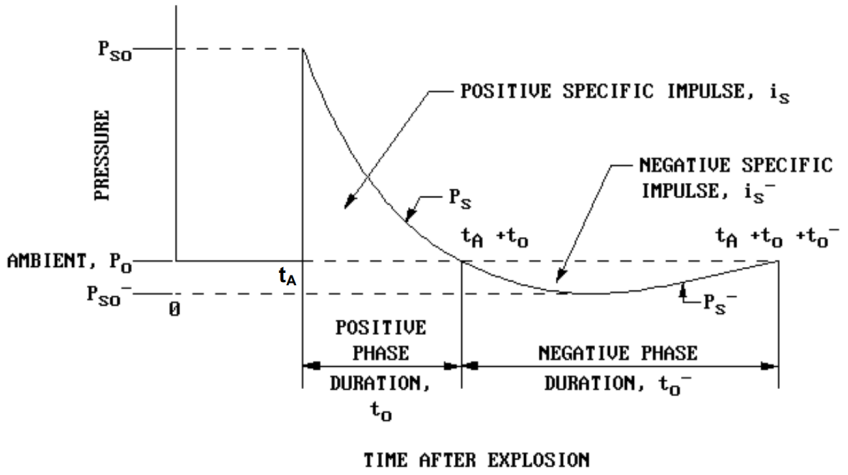

Figure 2.3: Typical pressure profile of a blast wave in time [15].

Initially, the element has an evolving pressure corresponding to the atmosphere pressure designated as P_0. Then, the element is submitted to an instantaneous increase of pressure, designated as peak incident overpressure P_{so}, related to the initial interaction between the element and the shock wave. The time necessary for the shock wave to reach the element is defined as t_A. A rapid exponentially decay of peak incident overpressure with time occurs and a return to ambient air pressure in time is reached, t_0 represents the positive phase duration. The area below the pressures curve represents the impulse acting on the structure due to the detonation and is designated as i_s. The acting impulse tends to be more relevant when considering external explosions. The increasing distance to the detonation epicenter causes a decrease in peak overpressure and shock wave velocity of propagation [20–22].

After considering the positive phase of the pressure curve, a negative phase with a longer duration than the positive phase, designated as t_0^-, occurs as the pressure stays below P_0. P_{so}^- is the minimum value of pressure. The correspondent area to the negative phase represents the negative impulse i_s^-. It is sometimes possible to see falling walls and glass in the direction of the explosion because of negative phase. Since the primary damage in a structure is caused by the positive phase, the negative phase is usually not considered [23].

The typical pressure profile of a blast in time can be represented by the modified Friedlander equation:

$$P_s(t) = P_{so} \cdot \left(1 - \frac{t}{t_0}\right) \cdot e^{-b \cdot \left(\frac{t}{t_0}\right)} \tag{2.1}$$

In which, P_{so} [kPa] represents the peak incident overpressure, t_0 [ms] represents the positive phase duration, t [ms] the time considered between the arrival time of the shock wave t_A [ms] and the time considered for the analysis, and b represents the decay wave coefficient [24].

2.2.2 Parameters of the blast load

There are some approaches well-known by the international community regarding the characterization of shock waves. The most known from the international community are the Kinney and Graham expressions and the Kingery and Bulmash expressions. The abacus from the American norm UFC 3-340-02 [15], for example, uses the Kingery and Bulmash expressions [20].

Peak incident overpressure

According to Kinney and Graham [20] the peak incident overpressure is defined by the follow equation:

$$P_{so}(\text{MPa}) = \frac{808 \times \left[1 + \left(\frac{Z}{4.5}\right)^2\right] \times P_o}{\sqrt{\left[1 + \left(\frac{Z}{0.048}\right)^2\right]} \times \sqrt{\left[1 + \left(\frac{Z}{0.32}\right)^2\right]} \times \sqrt{\left[1 + \left(\frac{Z}{1.35}\right)^2\right]}} \tag{2.2}$$

Impulse incident overpressure

The impulse incident due to the positive and negative phase results from the integration of equation 2.1, which describes the typical pressure profile of a blast wave in time, represented in Figure 2.3. Represented as i_s, the impulse of the positive phase, and i_s^-, the impulse of the negative phase, these parameters can be obtained from the equations 2.3 and 2.4 below.

$$i_s = \int_t^{t+t_0} P(t)\, dt = \frac{P_{so} \cdot t_0}{b} \cdot \left[1 - \frac{1 - e^b}{b}\right] \tag{2.3}$$

$$i_s^- = \int_{t+t_0}^{t+t_0+t_0^-} P(t)\, dt = -\frac{P_{so} \cdot t_0}{b^2} \cdot e^{-b} \tag{2.4}$$

Kinney and Graham [20] proposed an empirical expression, see equation 2.5, for the positive phase that can predict the impulse incident overpressure considering only the scaled distance.

$$i_s\ [\text{MPa} \cdot \text{ms}] = \frac{0.0067 \times \sqrt{1 + \left(\frac{Z}{0.23}\right)^4}}{Z^2 \times \sqrt[3]{1 + \left(\frac{Z}{1.55}\right)^3}} \tag{2.5}$$

Positive phase duration

Kinney and Graham [20] presented an equation that can predict the duration of the positive phase.

$$t_0\ [\text{ms}] = \frac{980 \times \left[1 + \left(\frac{Z}{0.54}\right)^{10}\right] \times \sqrt[3]{W}}{\sqrt{\left[1 + \left(\frac{Z}{0.02}\right)^3\right]} \times \sqrt{\left[1 + \left(\frac{Z}{0.74}\right)^6\right]} \times \sqrt{\left[1 + \left(\frac{Z}{6.9}\right)^2\right]}} \tag{2.6}$$

Shock wave reflection

A blast wave can interact with different surfaces around during its propagation. When a blast wave interacts with a solid surface, shock wave reflection and amplification occur. This phenomenon causes peak reflected overpressure, P_r, always higher than the peak incident overpressure (P_{so}). As a result, the resultant pressure values differ from those described. Depending on the angle of incidence of the shock wave, three different cases can occur. The first case can be defined as normal reflection when the direction of the wave is perpendicular to the surface. An oblique reflection can also occur when the wave propagation direction reaches the surface at an oblique angle. The third case is related to a phenomenon described as Mach reflection, which occurs when the shock wave reaches the surface at a specific angle [16, 24].

From the three cases described above, normal reflection is critical for a structure. This phenomenon is characterized as a blast wave reaching the contact surface perpendicularly and reaching a higher value of peak incident overpressure [16, 20]. Figure 2.4 describes the pressure-time variation for the incident and reflected pressure.

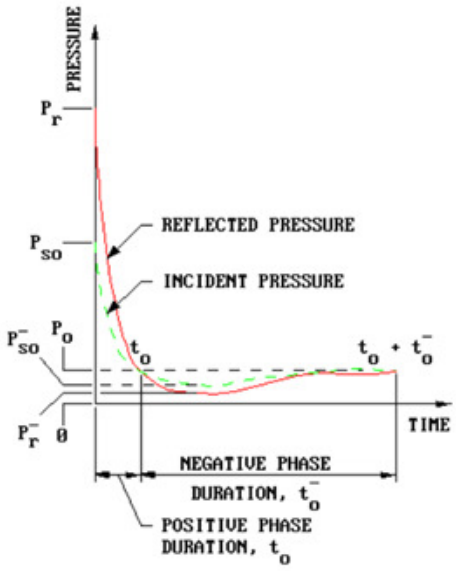

Figure 2.4: Pressure-time variation for the incident and reflected pressure [14].

The reflected overpressure can be defined using the Rankine and Hugoniot method (equation 2.7). This method considers the perfect gas behavior for the air and the suction effect due to the shock wave [25].

$$P_r\,[\text{MPa}] = 2 \cdot P_{so} \cdot \frac{7 \cdot P_o + 4 \cdot P_{so}}{7 \cdot P_o + P_{so}} \tag{2.7}$$

In Table 2.2, different values for the peak reflected overpressure could be observed for different relations of W – R (weigh oh explosive and distance from the target surface).

Table 2.2: Peak reflected overpressure Pr (MPa) for different W-R relations [15].

RW	100 Kg TNT	500 Kg TNT	1000 Kg TNT	2000 Kg TNT
1m	165.8	354.5	464.5	602.9
2.5m	34.2	89.4	130.8	188.4
5m	6.65	24.8	39.5	60.19
10m	0.85	4.25	8.15	14.7
15m	0.27	1.25	2.53	5.01

For design purposes, reflected overpressure can be idealized by an equivalent triangular impulse of maximum peak pressure P_r and time duration t_0. The relative impulse can be defined by the equation 2.8.

$$i_r = \frac{1}{2} \times P_r \times t_0 \tag{2.8}$$

According to [25], equation 2.8 can be simplified using equation 2.9 to obtain the relative impulse.

$$\frac{i_r}{i_s} \approx \frac{P_r}{P_{SO}} \tag{2.9}$$

Figure 2.5 describes the influence of the peak incident overpressure P_{so} and the angle of incidence α on the peak reflected pressure P_r. The maximum value of peak reflected pressure is reached in the case of normal reflection at a distance R_A from the affected surface. The presence of an angle between the blast wave propagation and the affected surface affects the resulting reflection originating lower values of peak reflected pressure [23].

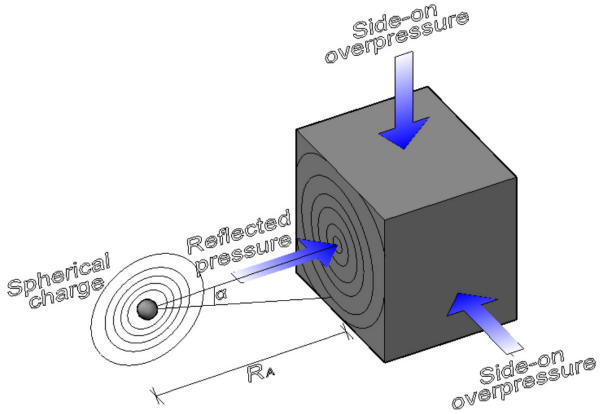

Figure 2.5: Pressure-time variation for the incident and reflected pressure [23].

Considering a reflection coefficient C_r, the peak reflected pressure P_r could be described as a function of the peak incident overpressure P_{so} and the angle of incidence α resorting to the equation 2.10 [23]. Also, the oblique reflection can be described in Figure 2.5 [16].

$$P_r = P_{so} \times C_r \tag{2.10}$$

A relation between the incident angle and the reflection coefficient can be found in the American norm UFC3-340-02 (Figure 2.6).

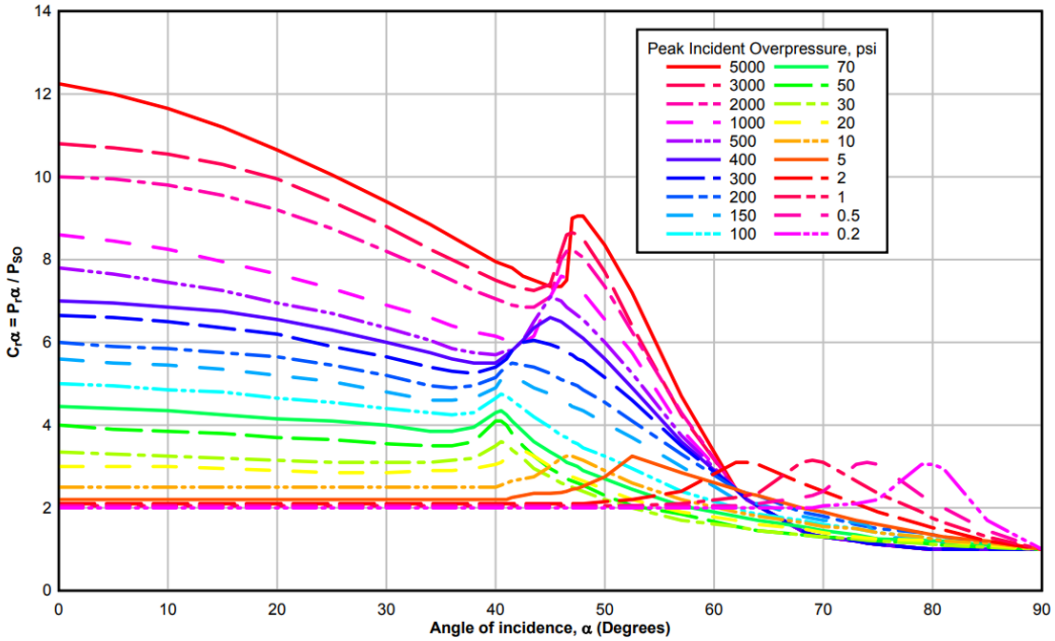

Figure 2.6: Relation between the reflected pressure coefficient and angle of incidence [14].

Mach reflection can occur for incident angles between 0º to 40º, characterized as occurring when the shock wave reaches the surface at a specific angle. This phenomenon is characterized by the junction of the incident wave and the reflected wave, where the reflected wave cannot pass the incident wave. Figure 2.7 describes the origin and propagation of a Match reflection [16].

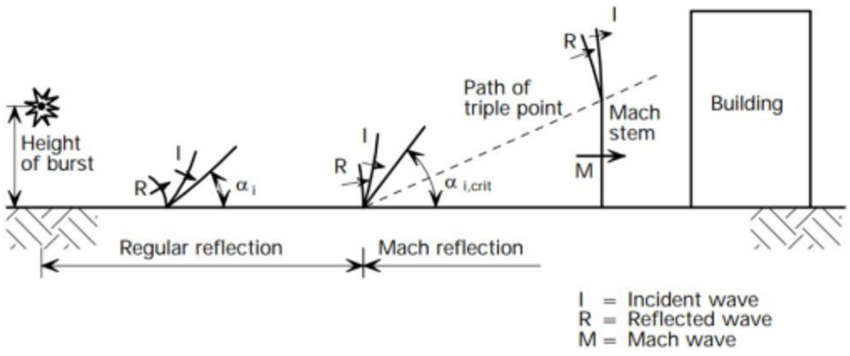

Figure 2.7: Mach reflection phenomenon (Adapted from [16]).

Mach reflection can be described as the worst-case scenario due to the substantial increase in the reflected overpressure that is caused. Hight values of overpressure than the predicted ones for a regular reflection usually occur in the presence of this phenomenon, depending on the initial peak overpressure [16].

2.2.3 TNT equivalence method

The use of TNT is well known and studied by the international community, and there are many documents and publications about the study of TNT and its explosion characteristics. Also, most of the shock wave propagation studies were conducted using TNT. Since there are plenty of different explosives that can reproduce different shock waves and blast energy, and the same amount of explosive can reproduce different explosions of different magnitude for different explosives, the use of TNT as an explosive reference to the study of a shock wave propagation is usually implemented [13, 14, 16].

The TNT equivalent weight, W_{TNTe} (kg), can be obtained based on the detonation energy of the explosive considered H^d_{EXP} (MJkg^{-1}), the detonation energy of TNT H^d_{TNT} (MJkg^{-1}), and the weight of the explosive considered W_{EXP} (kg). Equation 2.11 represents the determination of the TNT equivalent weight:

$$W_{\mathrm{TNT}_e} = \frac{H^d_{\mathrm{EXP}}}{H^d_{\mathrm{TNT}}} \times W_{\mathrm{EXP}} \tag{2.11}$$

Some examples of the TNT equivalent weight related to different explosives are illustrated in table 2.3:

Table 2.3: TNT equivalency for different types of explosives (Adapted from [6]).

Examples of explosions	**TNT equivalency**
PETN	1.3
Improvised explosives	0.4-1.0
RDX	1.2
Composition B (60%RDX, 40%TNT)	1.1

2.2.4 Scaled distance

Hopkinson (1915) and Cranz (1926) formulated an expression to deduce the shock wave propagation as a function of a scale parameter designated as scale distance, Z. This relation is based on the principle that it is possible to reproduce similar shock waves considering the same scaled distance of two explosions in the same environment and two charges of the same type of explosive with the same geometry, but with different sizes. The equation 2.12 that describes this phenomenon is illustrated below:

$$Z = \frac{R}{\sqrt[3]{W}} \tag{2.12}$$

where Z (m/Kg$^{\frac{1}{3}}$) represents the scale distance, R (m) is the distance between the structure and the center of the explosive charge, and W (Kg) is the weight of the explosive charge [13, 26].

2.3 Peak dynamic pressure

After the propagation of the blast wave, a blast-induced effect occurs due to dynamic pressures. Dynamic pressures occur due to increased air flux and products resulting from the blast. Being a function of

the peak incident pressure resulting from the blast, the blast-induced effect overrides the overpressure originated by the shock wave. The resultant pressures produce suctions on the surrounding elements non directly submitted to the blast load, creating lateral forces designated as drag loads on the intersecting elements [13, 21]. The relation between the peak dynamic pressure and the peak incident pressure can be found in the UFC 3-340-02 [14].

Some analytical solutions for the definition of the drag load q_s were proposed by Rankie and Hugoniot [25]. The equations 2.13 and 2.14 (Rankine-Hugoniot [25]) define the drag load q_s, based on the peak incident pressure of the explosion (P_{so}), in which P_0 corresponds to the atmospheric pressure.

$$q_s = \frac{5}{2} \cdot \frac{P_{so}^2}{2(P_o + P_{so})} \tag{2.13}$$

$$q_s = 0.022 \times (P_{so})^2 \tag{2.14}$$

Also, Newmark's equations for low pressures and seal-level atmospheric conditions can be used to define the drag load [21].

2.4 Closing remarks

Since the experimental campaign that was performed required the use of explosive charges for the dynamic blast loading tests, understanding the behavior of shock waves and the parameters that characterize the blast load from the explosive is assumed to be essential to understanding the entire phenomenon. The explosive charge that was used for the experimental dynamic tests was the C4, and the TNT equivalence method was used as a reference to understand the shock wave propagation.

2.5 Explosive Driven Shock Tube

An explosive driven shock tube, also designated as EDST [27], is basically a simple tube set between the explosive charge and the main target. Different cross-section geometries can be considered for the tube. An EDST can be considered a suitable laboratory scale tool able to produce well selected pressure-impulse combinations. The confinement and the multiple reflections permit to obtain realistic blast pressure profile with high impulse with small charges and generate a planar blast load at its end [27, 28].

The consideration of an EDST in the study of the UFBD when subjected to blast loads allows the simulation of a realistic blast pressure profile with high impulse with small charges in small-scale laboratory testing, reducing costs and permitting to obtain initial results before performing live blast tests.

Chapter 3

Definition and characterization of an energy absorber device

3.1 Blast protection for ISO containers - literature review

In both military and civilian environments, the use of container systems for transporting goods and merchandise or for any other purpose is widespread. In military theaters of operations, the safety of both personnel and equipment in unstable regions is a major concern. In temporary military constructions, ISO containers are commonly used as survival shelters to protect personnel and equipment (Figure 3.2. In the civil environment, the use of containers is more related to the industry, specifically in petroleum refining facilities (Figure 3.1) [29].

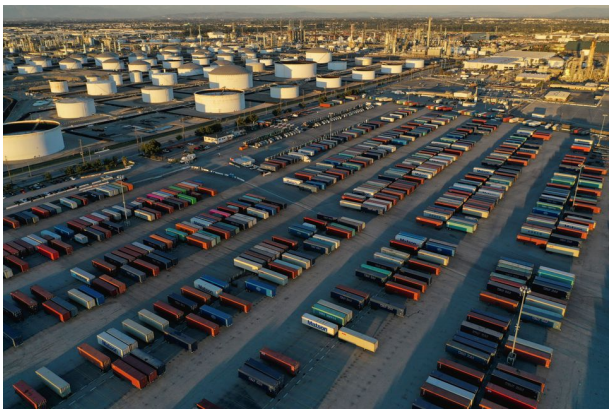

Figure 3.1: Cargo shipping containers adjacent to storage tanks at Marathon Petroleum's Los Angeles Refinery [30].

In order to fulfill their role for military use, ISO containers need to meet specific requirements as regards to their resistance to different threats, namely improvised explosive devices (IED), mortar strikes, and vehicle-borne improvised explosive devices (VBIED). In the civil environment, requirements are more often related to accidental explosions involving large quantities of LPG (Liquefied Petroleum Gas)

and other highly flammable products, causing severe damage to construction and people [31].

Figure 3.2: Military applications of container systems [32, 33].

Studies on the resistance of ISO containers when submitted to a blast load have been carried out, and the results show that they suffered severe damage when submitted to a design blast load. The low resistance capacity of an ISO container, when submitted to a blast load, could put in danger the material or personnel inside [29, 34–36].

In order to improve the resistance of such structures, Børvik et al. [34, 37] and Anderson et al. [38] proposed different blast-resistant solutions and performed blast load structural tests on ISO containers.

Børvik et al. [34, 37] proposed a ballistic and blast-resistant solution based on a wall for a standard 20 ft ISO container used as shelter in international operations using an extruded aluminum panel made of aluminum alloy AA6005-T6 by Hydro Aluminum, filled with a local granular material, fixed to one of the faces of the container (Figure 3.3). The threats considered for the study were a blast load from 4000 kg TNT at 120 m stand-off distance and the ballistic impact from a 7.62 mm AP projectile at a velocity of 820 ± 10 m/s.

(a) Aluminum panel filled with gravel.

(b) Mounting process of the aluminum panels.

Figure 3.3: Aluminum panels made of aluminum alloy AA6005-T6 by Hydro Aluminum, filled with a local granular material [34, 37].

Anderson et al. [38] performed full-scale blast tests on a blast-resistant wood building (BRWB) at BakerRisk's Box Canyon Test Facility and on a 20 ft ISO shipping container using a deflagration load generator (DLG). When subjected to two consecutive blast tests with increased overpressure and

impulse, the BRWB performed better than the ISO shipping container.

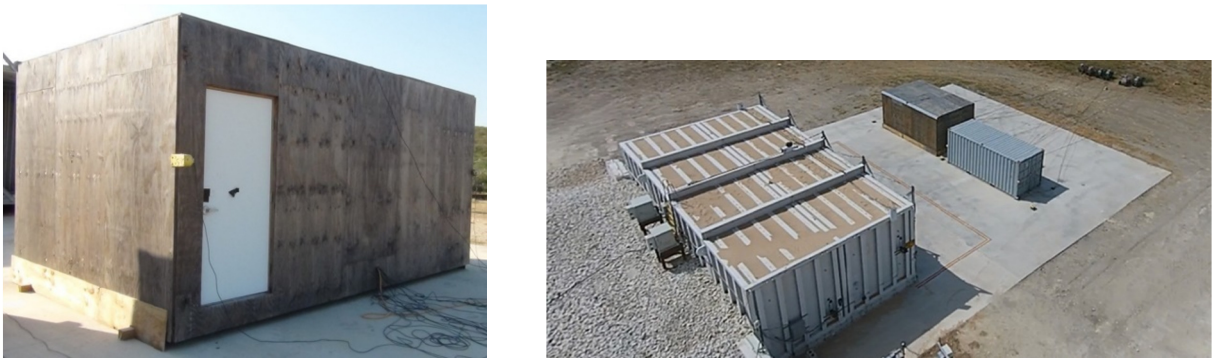

(a) BRWB. (b) Full-scale Experimental tests.

Figure 3.4: Blast-Resistant Wood Building (BRWB) [38].

Commercial solutions are already available in the market for protection against blast and ballistic impact for ISO containers. The Changzhou Magindustry company [39] specializes in offshore/onshore service modules and products. Publicly available technical specifications indicate a blast-proof shelter solution design as 12psi + 200ms blast resistant rate and designed with blast proof door and Windows.

The Ebtech Industrial [40] describes solutions for blast and ballistic containers on modified Standard ISO containers for blast and ballistic protective buildings to shield personnel, resources, and assets. Their products offer protection for many different threats and structures for different applications, achieved by using proprietary and unique energy-absorbing wall and frame systems, steel structures, composite materials, or fortifying existing facility structures with custom-designed support systems. Different protection systems can be incorporated in the main structure depending on the type of protection required. Publicly available technical specifications indicate solutions for blast protection for 10 psi + 125 psi-msec Free Field Blast Pressure and ASCE Medium Response, and ballistic materials certified by third-party laboratories towards NIJ, UL 752 and STANAG standards.

According to Børvik et al. [34], a structure used as a shelter for international operations equipped with add-on protection should fulfill four requirements. The first requirement, related to the threat, defines that the protection should be capable of resisting blast load and ballistic threats according to the respective norms. The second requirement relates to the structural requirements. Add-on protection should be capable of attaching to the structure without structural adaptations, and the protection should not collapse or deform the structure during the blast. The third requirement relates to the manufacturing requirements. The protection should not limit the functionality of the structure. The materials used need to be commercially available and cost-effective, with low to zero maintenance, enabling fast repair of the damaged parts. The fourth requirement relates to the logistic requirements. The protection should be capable of transportation with limited manpower for assembly and low mass/weight and volume.

Finding a protection system that can accomplish all these requirements is difficult. Some of the requirements can be in direct conflict, particularly when requiring very cost-effective, and low-mass and volume materials. Reducing the areal density of a protection system through knowledge-based design may increase the protection's price or volume [34].

Energy dissipation systems can solve mobility problems and improve the capacity of being replaceable after an explosion, restoring the material capacities. The main principle of this type of protective system is the ability to convert the kinetic energy from a blast wave into plastic deformation energy instead of relying mainly on the mass of the protective system [41]. Concentrating damage in easily replaceable protection components instead of the primary structure elements, allowing the structure to be repaired and re-occupied faster and continue the operation after an attack, is another main principle of energy dissipation systems [8].

Some studies about energy dissipative systems have been developed. One mechanism that has shown good results to work as a dissipative device for blast loading is the energy-dissipating component assemblies (EDCAs) [7, 8]. The concept is the creation of panels connected to a steel frame compliant with the ISO container standards using the EDCAs. When the blast occurs, the panels may deform, and the energy from the blast is transferred to the EDCAs, which extend and plastically deform, limiting the energy transferred to the structure. The steel frame needs to be designed to resist the blast loads, and the EDCAs and panels need to be replaced after the blast since the main structure is supposed to stay undamaged [8, 9].

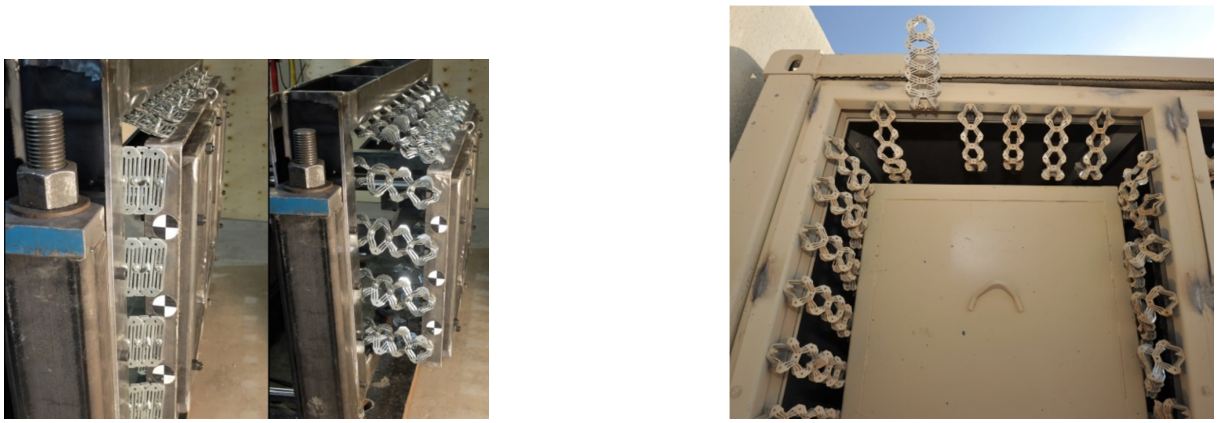

(a) EDCAS prior to, and post small-sclale testing.

(b) Final state of EDCAs after full-scale test.

Figure 3.5: Experimental testing in EDSAs Experimental [8].

These devices were studied, and were concluded that they can limit the energy of the blast load transferred to the structure and enable the protection of the contents and occupants from a blast, allowing the reorganization and recovery of the structure after an explosive attack [8]. Compared to other protective systems based on one high mass/weight relation, the EDCAs allow a significant reduction in system mass and permit a faster reorganization and recovery after a blast.

The particularity of the EDCAs, when compared to other energy-dissipative devices, relays how energy is dissipated. Instead of dissipating energy using compression of a crushable sacrificial material, the device dissipates energy through the tensile deformation of the assemblies.

It is expected that the proposed device in this master dissertation has a similar behavior. With much less required mass and capable of dissipating most of the blast wave, decreasing the impact on the structure, the proposed device is expected to allow a faster recovery of full functionality after an extreme event.

3.2 Energy absorber systems, an overview

An energy absorber can be simply defined as a system that converts, totally or partially, kinetic energy into another form of energy. The converted energy can be considered reversible, considering pressure energy in compressible fluids and elastic strain energy in solids, or irreversible in the case of plastic deformation energy [41]. One of the objectives when designing an energy absorber is the capacity to absorb most of the kinetic energy and deform itself in an irreversible way to avoid or at least ensure that human injuries and equipment damage are minimal [42]. Many different components can be used in energy absorbers, such as steel drums, circular tubes, tubular rings, square tubes, corrugated tubes, multicorner columns, frusta, struts, honeycomb cells, sandwich plates, and some other special shapes such as stepped circular thin-walled tubes and top-hat thin-walled sections. These components can also be used filled with liquids, foam, wood shavings, and sand, arranged in various geometries. Energy absorbers can be applied in various situations, such as crashworthiness of vehicles, crash barrier design, safety of nuclear reactors, collision damage to road bridges and offshore structures, and oil tankers [41].

3.2.1 Sacrificial claddings

Sacrificial claddings are usually constructed out of thin mild steel sheets [43]. The main objective of this type of system is to protect the underlying structure by reducing the peak force transferred, allowing the main structural elements to remain elastic. Sacrificial claddings work as passive architectures dissipating the blast wave energy and improving the target's resistance against such solicitation. They are made of three components (Figure 3.7): a crushable core, sandwiched between a front plate and a rear plate [44–47]. The front plate is responsible for the fluid-structure interaction between the blast wave and the sacrificial cladding [48], while the core is responsible for the energy absorption of the mechanism [49]. For the core, different materials have been studied and considered. Polymer foam [50–52], metal foam [44, 53, 54], hybrid foam [55], honeycomb [46, 56], and tubular structures [57, 58] are materials that can be considered for the core in sacrificial claddings due to their elastic and plastic properties. Cellular materials have been extensively studied for the core, and their behavior is well-known and can be described with a generic stress-strain curve (Figure 3.6) that represents these materials' behavior under compression. The behavior of cellular materials in sacrificial claddings is defined by three phases: the elastic phase, the plastic phase, where the stress remains constant as the strain increases, and the densification phase caused by the contact between the edge of the cells stopping the compression and rising the stress significantly [59].

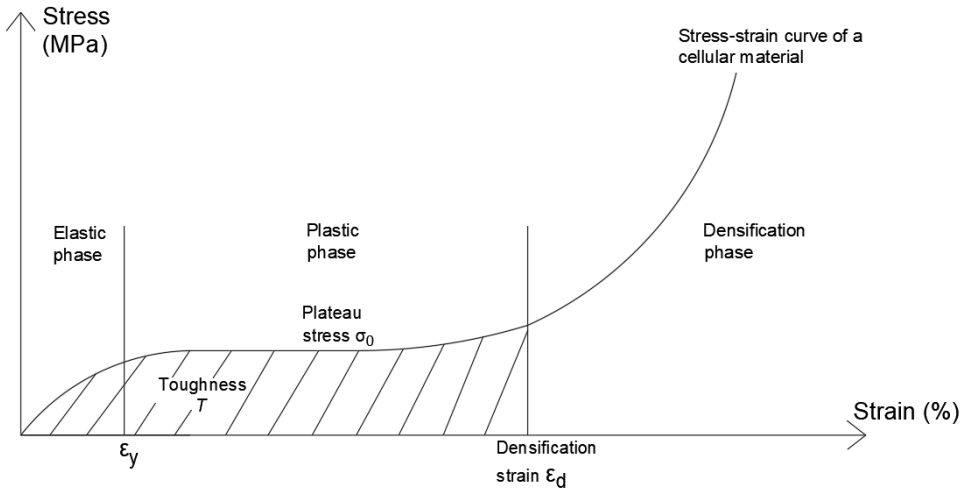

Figure 3.6: Generic stress-strain curve for the behavior of cellular materials in sacrifitial claddings (Adapted from [59]).

The curve represented in Figure 3.6 is described using three parameters [59]:

- Material toughness T, corresponding to the energy dissipated by the cellular material under compression described by the integration of the stress/strain curve;

- Plateau stress σ_0, corresponding to the load between the end of the elastic phase of the material ϵ_y and the beginning of its densification phase ϵ_d;

- Densification strain ϵ_d, corresponding to the strain at which the struts and plates of the cellular material come into contact, leading to the densification of the sample.

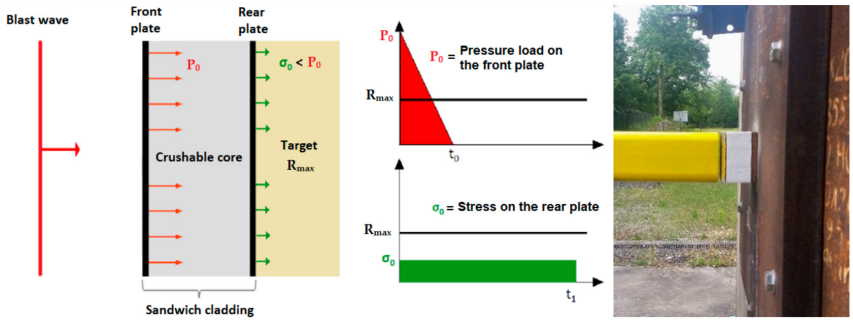

Figure 3.7: Sacrificial cladding submitted to an ideal planar shock wave [59].

Collapsible Energy Absorbers

The use of collapsible energy absorbers is usually related to applications in the crashworthiness of vehicles (cars, lifts, aircraft, ships), crash barrier design, safety of nuclear reactors, collision damage to road bridges and offshore structures and oil tankers [41]. The concept of crashworthiness is normally applied to the vehicle industry and is defined as the capability of a vehicle structure and its components to protect the occupants in case of a crash without any serious injury or death. The vehicle structure should be capable of absorbing the maximum impact energy with less damage to the main structure and avoid injury to the passenger. This concept can also be applied to the collapsible energy absorbers

in general, where the objective is the capacity to absorb most of the kinetic energy and deform itself in an irreversible way to avoid or at least ensure that human injuries and equipment damage are minimal. The concept of impact mechanics in the energy absorbers refers to the fact that the dynamic plastic deformation of a collapsible energy absorber structure differs and is more difficult to understand than the corresponding quasi-static deformation. This occurs due to two important physical phenomena, inertia and strain rate effects, the dynamic plastic collapse. The impact mechanics of a collapsible energy absorber are visible in the energy absorption capacity and crash response of a thin-walled circular tube under quasi-static or dynamic axial loading (Figure 3.8) [60].

(a) Under quasi-static loading

(b) Under dynamic loading

Figure 3.8: Final deformation shape of circular tube [60].

In the literature, there are numerous types of collapsible energy absorbers. Alghamdi [41] has reviewed the most common collapsible energy absorbers investigated in the literature and the most common ones include tube deformation modes such as inversion, splitting, lateral indentation, lateral flattening, axial crushing, axial crushing of frusta, crushing of struts and sandwich panels as well as other structures. Although most of these systems were developed for vehicle collisions, some have also been adopted and proved to be useful as sacrificial cladding for blast protection.

(a) Symmetric

(b) Extensional

(c) Asymmetric mixed

Figure 3.9: Deformation modes of square tubes [60].

Blanc ([59]) performed an experimental analysis of a sacrificial cladding filled with different brittle materials, from concrete foam to granular media, for blast protection. They were subjected to blast loading using an explosive-driven shock tube (EDST). The compression of the core was recorded using high-speed cameras while a sensor measured the load transmission. It was verified that the concrete foam and granular media can act effectively as a crushable core in a macroscopic point but differ significantly in terms of energy dissipation mechanisms. The concrete foam behaves similarly to any kind of stochastic foam or usual crushable core and is admitted as a potential energy-absorbing material when

its density is chosen according to the potential threat. However, its efficiency is low compared to a traditional honeycomb, and the material has other limitations that can affect its behavior. The granular media was shown to be also an efficient energy dissipative material in a macroscopic approach. However, it also showed to be quite impossible to quantitatively investigate how the energy is dissipated, and further investigation is needed.

Figure 3.10: Sacrificial cladding submitted to an ideal planar shock wave [59].

3.2.2 Mechanical devices

Energy absorption mechanisms often fall into two categories: mechanical or hydraulic, and occasionally, a combination of both. Mechanical energy absorption methods commonly employ a fundamental spring mechanism alongside a friction system to mitigate or dissipate the forces generated by the spring [61].

Mechanical devices such as fluid viscous dampers (FVDs) have been proven to be successful for protecting electronic systems on military platforms when submitted to high levels of blast loading from explosives and for the vibration isolation of piping systems, forging hammers, and other equipment [62]. Recently, fluid viscous dampers have been applied to protect engineering structures by dissipating seismic energy [63]. A fluid damper can be simply defined as a device that dissipates energy by applying a resisting force over a finite displacement or input motion. The process of energy dissipation primarily involves heat transfer, where the mechanical energy dissipated by the damper results in the heating of the damper's fluid and mechanical components. This heat energy is then safely transferred to the surrounding environment through typical mechanisms, such as convection and conduction (Figure 3.11) [64]. When submitted to dynamic blast loading, this system can absorb large amounts of blast energy during the structural response and kinetic energy is conserved after the blast load occurs. Damping energy originated reduces the strain energy and is considered very effective in reducing the inelastic demand by adding large amounts of viscous damping energy dissipation [65].

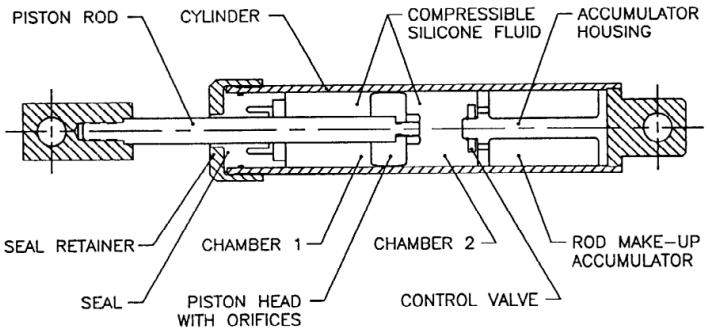

Figure 3.11: Fluid inertial damper [64]

Considering the case study, the UFBD is an energy absorber device that can be classified as a mechanical device capable of dissipating the kinetic energy due to the traction of the flat bar into plastic deformation energy originated by the movement of the flat bar around the pin inside the mechanism box.

3.3 Characterization of an energy absorber device

In 1984, Calladine and English [9] defined the behavior of two different types of plastically deforming structures in energy absorbing situations under impact loading, designed as Type I and Type II. Type I can be considered a bilinear model, and Type II is a curve characterized by its peak and exponential decay. The Load-deflection curve that characterizes each type of device is illustrated in Figure 3.12.

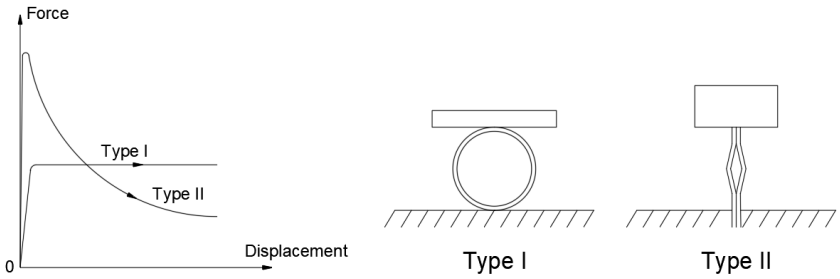

Figure 3.12: Classification of energy absorbing structures according to Calladine and English (Adapted from [9]).

Calladine and English [9] demonstrated that the deformations of type II structures are much more sensitive to changes in the impact velocity than that of the type I structure. Considering the same kinetic energy, smaller deformations are associated with higher impact velocities, a phenomenon characteristic of Type II structures. These conclusions were obtained from a study of impact using a hammer with different masses and weights for seven different weights. The behavior of the each structure considered in the study is illustrated in Figure 3.13.

Figure 3.13: Experimentnal test on type I and type II specimen before and during deformation (Adapted from [9]).

The results obtained by the authors were analyzed, through a sensitivity analysis based on the impact velocity. This led to the development of a theoretical model based on inertia and another based on the strain rate, aiming to separately estimate the maximum observed displacement. Comparing the theoretical model with the experimental results, it was verified that the analytical results did not match the experimental results [9].

Zhang and Yu [66] improved the model by considering a mechanism of 4 plastic hinges illustrated in Figure 3.14. A detailed discussion on the velocity sensitivity of type II structures using theoretical techniques was provided. The authors provide an analysis of the ”velocity sensitive” of type II structures considering a quantitative account of the effects of strain rate and inertia on a type II structure to provide a comparison with the results obtained by Calladine and English.

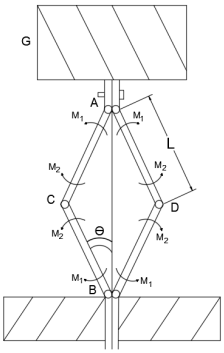

Figure 3.14: The four-hinge mechanism of type II specimens (Adapted from [66]).

For type I structures, Reid and Reddy [67] used cross-layered systems of metal tube that can be classified as type I structure and carried out experimental studies using low-speed impact in a drop hammer apparatus. Experiments on one-dimensional ring systems in a high-speed impact apparatus were also considered. The main objective was to study the main mechanism which controls the deformation of this type of structure, considering the effects of strain rate and inertia.

Tam e Calladine [68] conducted more analytical and experimental studies. The authors concluded that for Type I structures, the energy is linearly absorbed in function of the displacement due to the proportional relation between the rotation of the plastic hinges and deformation. In Type II structures, a high quantity of energy is absorbed for the existent geometry for a small deformation.

The conclusions proposed by these experimental studies pointed to a behavior where Type II structure, subjected to a high initial velocity, will lead to the formation of plastic hinges and rotations, which

result in high strain rates and high transversal acceleration. The deformation process for Type II structures can be described in two phases: first, the compression of the structure, and then, the rotation of the plastic hinges. For the first phase, inertia effects are the dominant effects, and for the second, the behavior depends on the sensitivity of the resultant deformation [68].

Su et al [69, 70], studied the effects of inertia and elasticity on a Type II structure when subjected to impact loading. An elastic-perfectly plastic constitutive relation for the material was considered to predict the peak load, which is important in designing energy absorbers characteristic of Type II structures. Figure 3.14 illustrates the mathematical model considered. Observing the strain rates and the elasticity of the material, it was possible to conclude that inertia is the main effect in Type II structures, not only in the first phase but also during the entire structure response. The high strain rate combined with high inertia causes a high resistance peak in the structure, originating lower displacements. It was observed that strain-rate effects play an equally important role as inertial effects on the dynamic behavior of this type of structure.

According to Guruprasad and Mukherjee [43], for energy absorption to be effective is important to "reduce the peak force and to extend the duration of the deformation." Type I structures are capable of absorbing large amounts of energy at a constant stress level which is preferred for energy absorption [71].

Considering the case study, it is fair to say that the UFBD can be classified as a mechanical device since the energy dissipation mechanism consists of converting kinetic energy into plastic deformation energy through a proportional relation between the rotation of the plastic hinges and the deformation of the flat bar during the moving of the flat bar around the pin inside the mechanism box of the UFBD. The load-displacement curve of the proposed device describes a curve similar to a bilinear model, typical of a Type I structure.

3.4 Effects of strain rates

When considering strain rate effects, it is known from the literature [72] that the material's yield stress and the stress-strain relationship do not have significant changes when considering quasi-static loading. However, it changes if the strain rate increases. Increasing strain rate values increases the material's yield stress and changes the material's stress-strain behavior in the plastic domain.

According to the literature [72], the material models that consider the strain rate dependency of the material's plastic curve are commonly used in finite element models to simulate dynamic extreme loading conditions using explicit analysis. Cowper-Symond, Johnson.Cook and Zerilli-Armstron are the most common material models to consider the strain rate effects. The main difference between them is how they consider the strain-rate effects. The main problem of these models is that they are based on material parameters that cannot be simply measured and determined, special experimental and optimization processes are needed to extract these parameters ([73–77]) and should be identified individually for each material under consideration.

The Johnson-Cook constitutive model considers the effect of an isotropic kinematic hardening, strain

rate, and temperature dependence of the material submitted to impact loading. Thermal softening due to adiabatic heating at higher deformation rates is also considered. The capacity to be applicable to different materials is one of the advantages of this model [78]. Equation 3.1 defines the Johnson-Cook constitutive model and determines the current yield stress of the material,

$$\sigma = (A + B \cdot \epsilon_p^n) \cdot \left(1 + C \cdot \ln\left(\frac{\dot{\epsilon}_p}{\dot{\epsilon}_0}\right)\right) \cdot \left(1 - \left(\frac{T - T_r}{T_m - T_r}\right)^m\right) \tag{3.1}$$

Where A, B, C, n, and m are model parameters, ϵ_p is the effective plastic strain, $\dot{\epsilon}_p/\dot{\epsilon}_0$ is the normalized plastic strain, T is material temperature, T_r is the room temperature, and T_m is the melting temperature. When the experiments are conducted at room temperature, the temperature effect can be neglected, and the following simplification in Equation 3.2 can be admitted [78].

$$\sigma = (A + B \cdot \epsilon_p^n) \cdot \left(1 + C \cdot \ln\left(\frac{\dot{\epsilon}_p}{\dot{\epsilon}_0}\right)\right) \tag{3.2}$$

The Cowper-Symonds material model considers the influence of strain rate only in the yield stress and does not consider temperature effects. Due to that fact, the plastic curves (flow stress as a function of strain) are parallel. Therefore, the larger the strain rate, the higher the flow-stress curve [72]. Equation 3.3 defines the yield stress according to the Cowper-Symonds material model,

$$\sigma_y = \left(\sigma_0 + \beta \cdot \frac{E_t \cdot E}{E - E_t} \cdot \varepsilon_{eff}^p\right) \cdot \left(1 + \left(\frac{\dot{\varepsilon}}{C}\right)^{\frac{1}{P}}\right) \tag{3.3}$$

Where, σ_0 is the reference yield stress, E is the material's elastic modulus, E_t is its tangent modulus, β is the hardening coefficient, ε_{eff}^p is the effective plastic strain and $\dot{\varepsilon}$ is the strain rate. C and P are the strain-rate parameters of the Cowper-Symonds material model.

The consideration of material models that account for the influence of strain rate is important for the study of the UFBD when subject to dynamic blast loading charges since the pressure induced by the shock wave can impose high deformation rates in the materials.

3.5 Bending Under Tension

The Bending Under Tension (BUT) is associated with the sheet metal forming process. It is one of the tests used to experimentally determine the friction values on the rounded edge of the die in sheet metal forming. The experimental BUT tests of Trzepiecinski and Lemu [79] were conducted using a specialized friction simulator, as illustrated in Figure 3.15. This apparatus was affixed to a universal tensile testing machine and featured a framework housing a horizontal tension member equipped with a load cell. One end of the specimen was secured at the terminus of the horizontal tension member, while the other end was anchored to a vertical tension member, also equipped with a load cell. The specimens utilized for the friction tests were specifically cut in accordance with the rolling direction of the sheet metal. These specimens were subjected to stretching at a constant rate of 0.25 mm per second. Each strip specimen possessed a width (w) of 10 mm and a length (L) of 135 mm. These strips were wound around a fixed

cylindrical roll with a radius (R) of 20 mm.

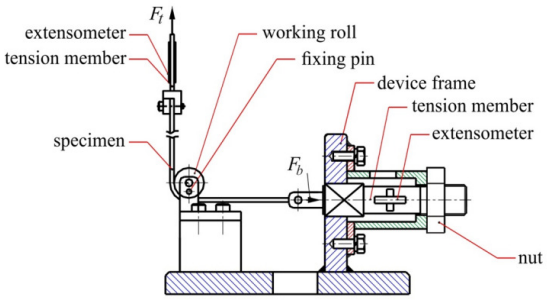

(a) Schematic view of the testing device

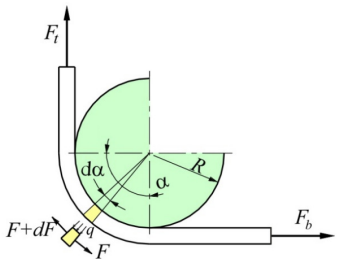

(b) Forces acting on an elemental cut of the strip

Figure 3.15: Schematic view of the BUT [79].

According to Trzepiecinski and Lemu [79], the evaluation of friction varies in space and time. It depends on the pressure applied due to the sheet elongation (influenced by the yield stress and strain hardening effects of the sheet and the die radius diameter), lubrification conditions, and surface roughness of the specimens. Considering the study performed by Trzepiecinski and Lemu, using lubrification and a roughness average of 0.32 µm for the roll, the values for the friction coefficient depending on the effect of the specimen elongation can be found in Figure 3.16.

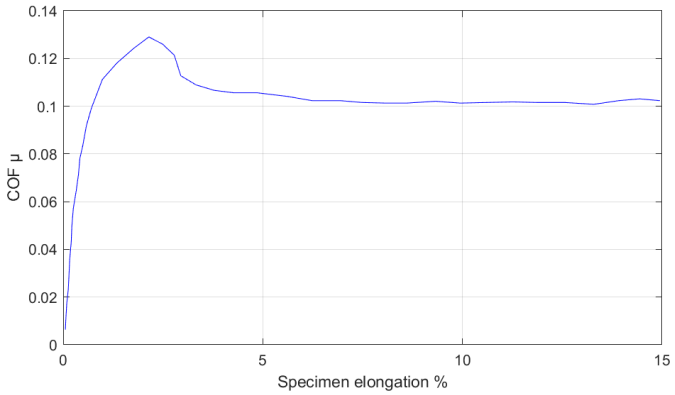

Figure 3.16: Friction coefficient according to the specimen elongation (Adapted from [79]).

According to Lian, Yang and Cao [80], the static friction coefficient can be defined as the first increase linearly to a peak of the curve and exponentially decrease to a steady value for the dynamic friction coefficient.

The BUT is of great importance in the study of the UFBD because it is the system in the literature that most closely resembles the function of the proposed device. The study of the influence of friction on the BUT can, to some extent, be likened to the influence of friction on the movement of the flat bar around the pin inside the UFBD mechanism box.

3.6 Continuous Bending Under Tension

Timothy J. Barrett and Marko Knezevic [81] performed a study focusing on modeling the behavior of materials subjected to Continuous Bending Under Tension (CBT) with a specific emphasis on understanding the post-necking strain hardening response of ductile sheet metals. The objective of the study is to identify the post-necking hardening behavior of ductile sheet metals, which is crucial for understanding material behavior.In Figure 3.17 is represented the CBT testing machine and the description of the main components used for the experiments. It is also illustrated the main process variables considered.

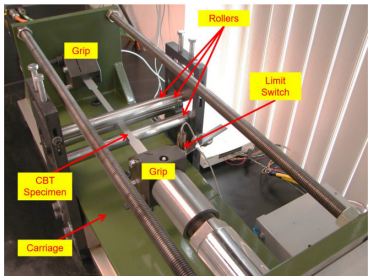

(a) Main components of the CBT testing machine

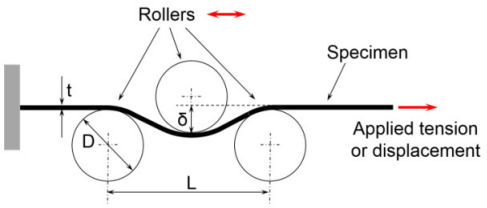

(b) Definition of the main process variables: bending depth, δ, sheet thickness, t, diameters of rollers, D, and distance between the bottom rollers, L

Figure 3.17: Schematic view of the CBT testing machine [81].

It was verified that the strength of the material primarily depends on the accumulated strain during pre-deformation and the effects on the stress state due to cyclic pre-deformation are secondary. The engineering true stress-strain curves based on the secondary simple tension testing (ST) are represented in the literature and illustrated in Figure 3.18.

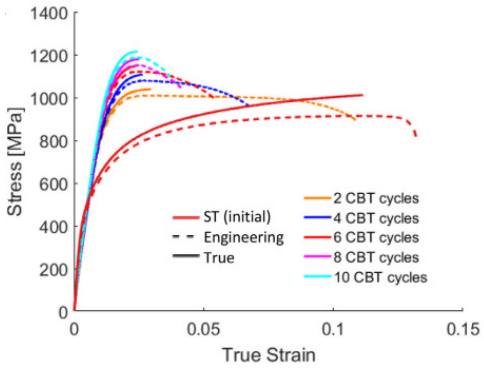

Figure 3.18: True stress-strain and engineering stress-strain curves of a DP 780 steel specimens recorded during secondary ST tests under a strain rate of 0.001 s^{-1} [81].

It was concluded that the strength of the material increases with the CBT cycles. The evolution of the elastic slope, yield strength, and strain at fracture for the tested specimens is also presented in the literature. It was also concluded that the formation of the back-stress fields during CBT is the mechanism responsible for reduction of the macroscopic elastic slope from the initial value of the specimen and the density of dislocations increases with plastic deformation in CBT rising the back-stress fields [81].

The evidence concerning the Continuous Bending Test (CBT) holds importance in the analysis of the UFBD's functioning as it lays the groundwork for the exploration of the pre-deformation of the flat bar during its motion around the pin within the mechanism.

Chapter 4

U-shaped dissipative flat bar bending device

The U-shaped dissipative device was conceived as a mechanical dissipative device, with a Type I behavior, displaying the ability to convert energy through a mechanical processing dissipating kinetic energy resulting from the pushing of the flat bar into plastic deformation energy due to the plastification of the flat bar.

4.1 Dynamic blast load testing

The work conducted in the subsequent chapters is intended to test the UFBD under dynamic conditions when subjected to blast loads acting perpendicular to the motion of the flat bar. The solution to test the proposed device under blast loading conditions was designed considering an existing steel frame previously used in the Royal Military Academy laboratory to test aluminum plates under blast loading. The design adopted involves fixing the mechanism box on one side of the steel frame and fixing the aluminum flat bar on the other by clamping two pieces of steel (Figure 4.1).

(a) UFBD configuration before the blast

(b) Steel frame configuration

Figure 4.1: Experimental test of the UFBD before the blast.

For the blast loading tests, the following parts were considered (Figure 4.2):

- Three aluminum flat bars: 2 mm thickness x 85 mm height x 511 (120+31+360+89) mm length;

- Pin: 20 mm diameter (20 mm steel) x 100 mm height. The pin has been placed in direct contact with the flat bar since the beginning;

- Rectangular profile simulating the mechanism box: 5 mm thickness (50x60x100 mm). Between the flat bar and the mechanism box wall there is an 8mm gap.

- Two L profiles: 50 mm x 50 mm and 5 mm thickness;

- Two rectangular pieces of standard steel: 50 mm x 200 mm and 5 mm thickness;

Figure 4.2: Details of the mechanism box and the two rectangular pieces of steel.

To assemble the device's parts, bolts were considered for the connection. The Pin is fixed to the mechanism box using the box walls and two bolts. The UFBD is connected to the main structure using two L profiles and two bolts. The remaining parts are connected to the main structure using bolts. The flat bar was shaped and prepared before assembling to the mechanism box and connecting to the main structure. To guarantee that the flat bar is perfectly parallel, the flat bar is clamped to the structure using two rectangular pieces of steel. The flat bar's 89 mm length is considered to guarantee, through a molding, the proper fixation of the bar to the main structure. All parts are attached to the main structure (steel frame) using an aluminum frame. The aluminum frame is important to guarantee the proper fixation of the UFBD and the steel plates to the steel frame. The importance of the steel plates is explained in more detail in the set-up (6.3) in Chapter 6. The explanation of the whole process is illustrated in Figure 4.3.

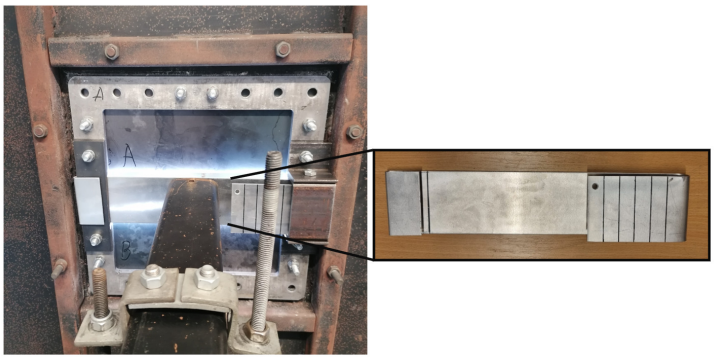

Figure 4.3: Detail of the set-up and the aluminum flat bar configuration.

The UFBD used for the blast loading tests was modified from the initial device employed in the Basto experimental studies. This modification of the device was necessary to accommodate it within the existing steel frame for conducting the experimental blast loading tests. Using a rectangular profile for the mechanism simplifies the device's construction and facilitates the attachment of other components to it, connecting them to the pre-existing steel frame. The pin is constructed from standard steel with a smooth surface to minimize friction with the flat bar. It is securely fastened to the mechanism using two bolts that prevent its rotation. The UFBD used in Basto's experimental tests involves the use of a pin with unrestricted rotation. The decision to immobilize the pin's rotation was made for practical reasons, as it simplifies the construction process of the device. As the mechanism's operation includes the use of lubrication, it is initially assumed that there is minimal friction between the components. Therefore, a pin with restricted rotation is acceptable. Furthermore, based on the numerical study conducted in Subsection 5.2.2 concerning the influence of the pin's rotation on the device's operation, it was observed that when lubrication is used to prevent friction between the components, the rotation of the pin has a negligible impact on the numerical results when compared to a fixed pin. Thus, it can be disregarded.

The design adopted to achieve the objectives of this dissertation also involves the use of an aluminum flat bar, as opposed to the steel flat bar used in Basto's experimental tests. This was required as the experimental conditions of the shock tube laboratory required the use of smaller blast loads and therefore a more ductile material was required. Also, the aluminum adopted for the experimental campaign is a well-characterized material with the commercial code EN AW-1050 H24, and its properties for small-scale blast loading tests are well-known and described in the existing literature [28, 82–84] related to the testing of aluminum plates subject to blast loading charges using a explosive driven shock tube (EDST).

To test the UFBD under dynamic conditions when exposed to blast loads perpendicular to the motion of the flat bar, the use of a shock tube was considered. The EDST used in the experimental tests is the same one as examined in Braz's [84] research. It features a cross-section of (80x80 mm^2) and was used for a 10g C4 load detonated 5 centimeters from the entrance of the EDST. This shock tube was chosen for testing the UFBD under blast loading conditions due to the detailed study and description of the reflected pressure curves at the end of the tube found in Braz's work. The description of the reflected pressure curves enables their implementation in a numerical model to validate the performance of the UFBD when exposed to blast loads. The numerical simulation of the UFBD for blast loading conditions in Subsection 5.3.2 validates the use of the considered tube to validate the function of the device. Considering the EDST employed in the experimental campaign, the height of the bar is set to 85 millimeters to cover the EDST section. As a result, the height of the rectangular profile of the mechanism box is adjusted to 100 millimeters to ensure the proper operation of the mechanism.

4.2 Quasi-static testing

The design chosen for the UFBD was subjected to quasi-static tests to assess its performance. This allowed to compare results with previous quasi-static tests, to calibrate the respective numerical models and to validate Calladine and English [9] hypothesis that Type I structures quasi-static test are good predictors of dynamically loaded structures.

The description of the design adopted for the UFBD is presented below (Figure 4.4):

- Aluminum flat bar: 2 mm thickness x 85 mm height x 511 (120+31+360+89) mm length;

- Pin: 20 mm diameter (20 mm steel) x 100 mm height. The pin has been placed in direct contact with the flat bar since the beginning;

- Rectangular profile simulating the mechanism box: 5 mm thickness (50x60x100 mm). Between the flat bar and the mechanism box wall, there is an 8 mm gap.

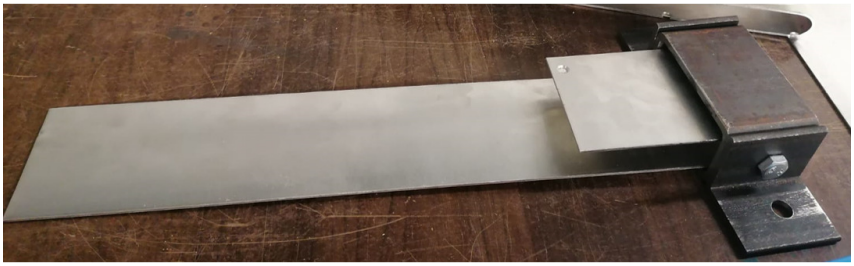

Figure 4.4: U-shaped dissipative flat bar bending device (UFBD) used for the experimental campaign.

4.3 Numerical modeling dynamic blast load testing

4.3.1 Initial numerical model

Basto [10] presented a numerical model using Ls-Dyna to recreate the experimental results he conducted for characterizing the UFBD. The numerical model takes into account the initial design, which includes the following components:

- Mechanism box: RHS 60x40x4 mm^3 with a length of 60 mm (EN 10219-1/2);

- U-shaped flat bar, 3 options: 50x4, 50x3 and 50x2 mm^2 (EN 10058);

- Loose pin: rod Ø10 mm (EN 10060).

The initial design of the UFBD incorporates the use of grease to mitigate friction between the components. It also includes the use of a pin with unrestricted rotation around its own axis to eliminate friction between the components. The application of grease and the unrestricted rotation of the pin are also incorporated in the numerical model presented by Basto.

The numerical analysis of UFBD under blast loads is also one of the proposed objectives for this master's dissertation. To achieve this, the study involves adjustments to the existing numerical model. To construct a numerical model capable of assessing the adapted UFBD design for blast loads, it was necessary to first examine modifications to the pre-existing model. Throughout this work, the pre-existing model is referred to as the initial numerical model. The primary purpose of the initial numerical model

used in this study is to perform a numerical analysis of the mechanism's behavior, with Basto's experimental results as a reference. Additionally, the initial numerical model incorporates the use of lubrication in its operation. However, the pin is defined as stationary without the ability to rotate around its axis. This adaptation, compared to the pre-existing model, aligns with the design adaptions made to the UFBD for blast load testing.

To conduct a numerical investigation of UFBD under blast loads, a new numerical model is developed, considering adaptations from the initial numerical model. The primary purpose of this numerical model is to initially analyze the behavior of the adapted UFBD through numerical simulations of quasi-static tests. Subsequently, it is employed for modeling dynamic blast load tests.

Chapter 5

Numerical analysis of the U-shaped dissipative device

5.1 Introduction

Considering the work performed in the research project of Basto [10], the main objective of the present work is to study the performance of the U-shaped dissipative flat bar bending device when submitted to blast loading. Taking this into consideration, a numerical study was initially conducted prior to the experimental campaign to avoid additional costs regarding the experimental campaign research and development and optimize the final product. The existing numerical model presented by Basto was further developed, using the Finite Element Model software Ls-Dyna.

LS-DYNA is a versatile finite element software designed to analyze the static and dynamic behavior of structures, even when they experience significant deformations. This includes structures that interact with fluids. The primary approach used for solving problems in LS-DYNA relies on explicit time integration methods. The explicit time integration method allows for the accurate capture and modeling of scenarios involving high-velocity impacts, rapid changes in loading, crashes, and explosions. It plays a pivotal role in dynamic simulations [85].

The work presented in this chapter is divided in two parts:

- The first part (Section 5.2) refers to the work developed to validate the numerical model design against the results obtained during the initial quasi static tests conducted by Basto. Considering the conclusions of Calladine and English for Type I devices, it has been assumed that the static tests would provide suitable validation and calibration for a numerical model, allowing initial numerical simulation of dynamic loading, an assumption which was validated by the shock tube laboratory tests conducted (described in Chapter 6).

-The first part (Subsections 5.2.4 and 5.2.5) also includes the numerical simulations of quasi-static tests for the study of the behavior of the mechanism with an aluminum flat bar instead of standard steel. This was required as the experimental conditions of the shock tube laboratory required the use of smaller blast loads and therefore a more ductile material was required.

- The second part (Section 5.3) refers to the work developed to perform numerical simulations of dynamic blast loading, which included the numerical simulations of quasi-static tests for the new design adopted for the blast loading experimental campaign. The numerical study of the proposed device presented in this work follows the following line of reasoning in Figure 5.1.

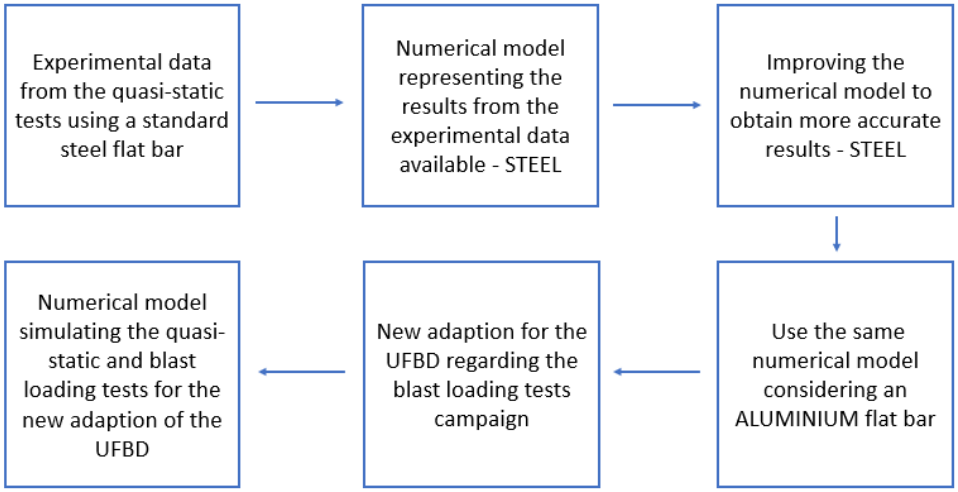

Figure 5.1: Description of the numerical study.

5.2 Initial calibration of numerical model

5.2.1 Initial numerical model - Steel

Geometry

The initial numerical model considers the following parts (Figure 5.2):

- Flat bar: 4 mm thickness x 50 mm height x 311 (160 + 31+120) mm length;

- Pin: 10 mm radius x 50 mm height. The pin has been placed in direct contact with the flat bar since the beginning;

- 2 Rectangular boxes simulating the box walls: 10 mm thickness x 50 mm height x 60 mm length. These solid elements are placed with a 2 mm gap from the initial position of the flat bar.

- Rigid load applier: Rigid load applier: 4mm thickness x 50mm height x 8mm length. The dimensions are not important for the case study since does not influence the numerical results.

The initial numerical model considers only the rectangular boxes to simulate the mechanism box since the only parts that influence the device's behavior are the mechanism box walls. Therefore, the remaining parts can be disregarded, reducing the computational costs.

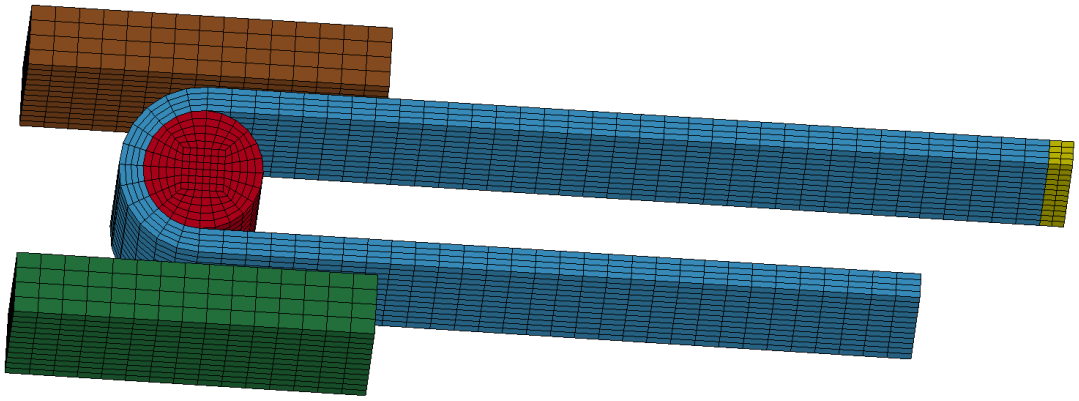

Figure 5.2: Red: Pin; Blue: Steel flat bar; Brown and green: Box walls; Yellow: Rigid load applier.

The proposed numerical model considers 3D solid elements, and a constant-stress solid element with one integration point is used for modeling the following parts (ELFORM=1). For the deformable parts (flat bar), hourglass was defined, and Flanagan-Belytschko with exact volume integration form (stiffness form) was applied. The model comprises 9477 nodes, assembled in 7104 elements with a single integration point.

Material models

The proposed model's definition of the material models is based on considerations. Considering that the rigid pin and rigid rectangular boxes are not supposed to deform permanently due to the plasticity phenomenon, a material model that does not consider permanent deformations was applied. Therefore, it is assumed that the rigid rectangular boxes and the rigid pin remain in the elastic region during the simulation, and the keyword `MAT_011_ELASTIC` is defined. This measure also allows a reduction of the computational time.

A rigid load applier connected to the flat bat was considered to simulate the prescribed motion considered in the quasi-static tests [10]. Since this solid element only applies a prescribed motion to the flat bar, the Keyword `MAT_020_RIGID` is defined. Therefore, for the flat bar, the keyword `MAT_024_PIECEWISE_LINEAR_PLASTICITY` was defined using a bilinear model based on the stress-strain curve for the standard steel obtained from the quasi-static tests [10]. Strain rate effects are not considered in the initial numerical model as a simplification. As mentioned in Section 3.4, when considering strain rate effects, it is known that the material's yield stress and the stress-strain relationship do not have significant changes when considering quasi-static loading. However, the study of the influence of strain rate on the mechanism's behavior is further explored in Subsection 5.2.3. The bilinear model that represents the constitutive law for the flat bar and the material properties of the material models are represented in Figure 5.3.

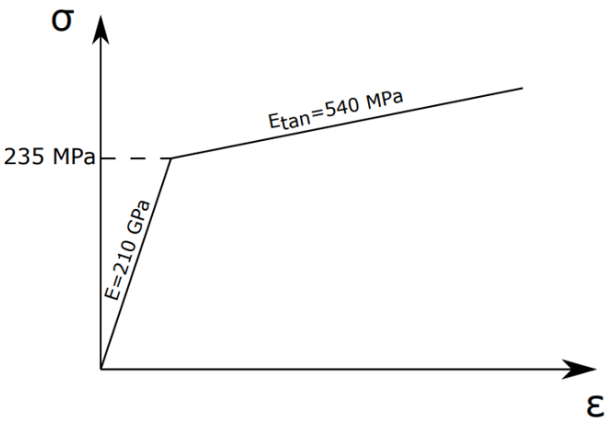

001_ELASTIC (Steel)

Mass density (Kg/m3)	Young's modulus (MPa)	Poisson's ratio
7850	2.100e+005	0.40

020_RIGID (Steel)

Mass density (Kg/m3)	Young's modulus (MPa)	Poisson's ratio
7850	2.100e+005	0.30

024_PIECEWISE_LINEAR_PLASTICITY (Steel)

Mass density (Kg/m3)	Young's modulus (MPa)	Poisson's ratio	Yield stress (MPa)	Tangent modulus (MPa)
7850	2.100e+005	0.30	304.00	540.00

Figure 5.3: Numerical stress-strain curve and material properties for the material models.

Contact

The model considers the contact between the flat bar and the pin and rectangular boxes. Therefore, the keyword `AUTOMATIC_SURFACE_TO_SURFACE` was defined. The definition of contact permits the interaction of the structural domains instead of just passing through each other. This option considers the contact with the different parts by defining a ”Slave” and a ”Master”. Since the flat bar is the part that is supposed to deform during the simulation, the flat bar part was defined as ”Slave”. For the ”Master”, a set of parts composed by the the rectangular boxes and the pin was defined using the keyword `SET_PART`.

The keyword `AUTOMATIC_SURFACE_TO_SURFACE` also considers the influence of friction for the contact established. For the case study, a static and dynamic friction coefficient was defined for the contact between the considered parts (Figure 5.4). The definition of the friction coefficients was based on a study of a similar mechanism found in the literature known as Bending Under Tension (BUT) [79, 86–88].

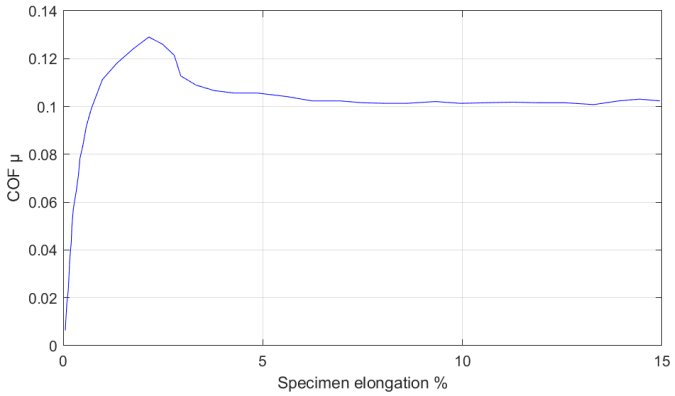

Figure 5.4: Friction coefficient according to the specimen elongation (Adapted from [79]).

According to Trzepiecinski and Lemu [79], the maximum static friction coefficients have a value between 0.12 and 0.14 and a value of 0.1 for the dynamic coefficient.

The experimental data from quasi-static tests for the U-shaped dissipative flat bar bending considers the application of lubrification to minimize friction. Due to that fact and considering Trzepiecinski and Lemu [79] (Figure 5.4), a value of 0.1 for the static and dynamic friction coefficient is adopted.

Boundary conditions and load

According to the design of the UFBD, the rigid holders simulating the mechanism box need to be fixed, and rotations and translations are not allowed.Therefore, the keyword `SPC_SET` was defined, and translational and rotational constraints in all directions were applied. Furthermore, while the rotation of the pin around its axis is an inherent part of the UFBD's design, it was decided that, considering the adaptation of the device for blast load testing, the pin would be fixed and rotations and translations are not allowed. Nonetheless, the impact of pin rotation on the initial numerical results will be examined in Subsection 5.2.2.

The keyword `PRECRIBED_MOTION_RIGID` was defined to simulate the force applied in the flat bar during the quasi-static tests, and a 160 mm displacement in the X direction was applied to the rigid load applier. Since in Ls-Dyna [89], all loads (e.g., velocities, displacements, pressure) are time-dependent, a definition of a load curve is needed. The objective of the numerical simulation is to obtain the final load-displacement curve. Therefore, a time-displacement curve is defined using the keyword `DEFINE_CURVE`. In other words, a 160mm displacement in the X direction was applied to the rigid load applier using a linear time displacement starting at zero and reaching 160mm of displacement for 0.1 seconds. The model considers the time termination for the simulations to be 0.1 seconds.

5.2.2 Initial numerical results

A force-displacement curve is needed to compare the results from the experimental tests (Appendix A). To obtain the force values in the numerical simulation is necessary to define the keyword `DATABASE_ASCI_option`. This keyword has different cards corresponding to different databases depending on the elements to study (e.g., Airbag statistics, material energies wall forces, SPC reaction forces, etc.) [89]. The `RCFORC` card was defined to measure the force applied to the flat bar. This card represents the resultant interface forces, and for the case study, the force is measured considering the resultant force due to the movement of the flat bar applied in the Master (rigid pin) in the X direction. Figure 5.5 illustrates the force-displacement curve from the initial numerical model and a comparison to the results from two quasi-static tests (Appendix A).

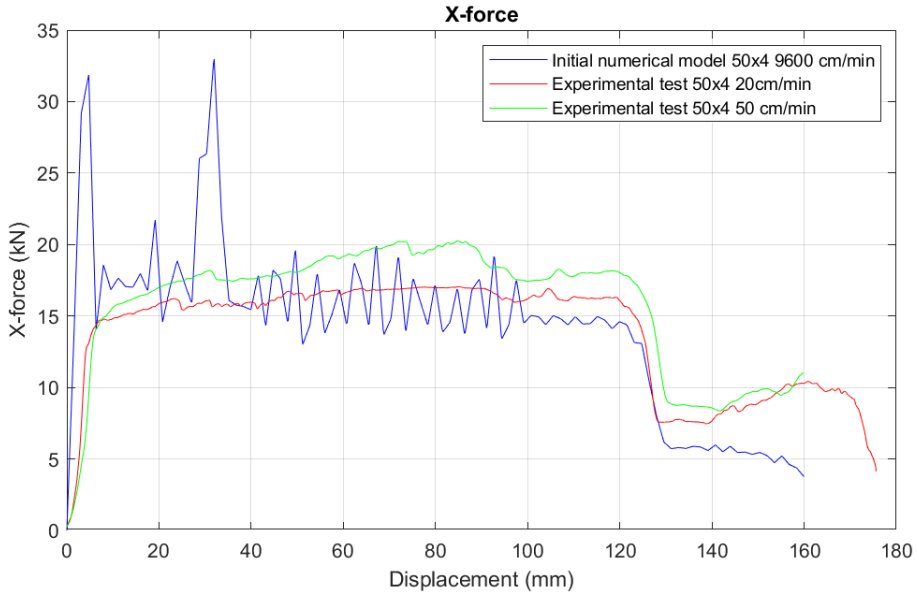

Figure 5.5: Force-displacement curve from the initial numerical model and a comparison to the results from two quasi-static tests.

From the graph presented in Figure 5.5, it is possible to observe that the numerical model represents relatively well the behavior of the mechanism. In Table 5.1 is represented a comparison of the numerical results and the experimental ones for the same flat bar thickness.

Table 5.1: Comparison of numerical (initial numerical model 50x4 9600 cm/min) and experimental results.

	Average plateau force (kN)	Initial numerical model 50x4 9600 cm/min (kN)	Error (numerical) (%)
Experimental test 50x4 20 cm/min	16.62	15.65	1.22
Experimental test 50x4 50 cm/min	18.86	15.65	14.84

The numerical model has relatively good accuracy for a first simulation when comparing to the experimental results.

The visible peaks at the beginning are related to the contact established when the small side of the flat bar reaches the corner of the rectangular box due to the force applied. Some bending phenomena of the flat bar can be visible due to this contact, and an increase of resultant force is reached. The lower peaks are related to the visible contact between the flat bar and the corners and walls of the rectangular boxes, especially due to the contact between the active length of the small side of the flat bar and the corner of the rectangular box. Before the decrease in peak of the force, the peaks tend to disappear. This phenomenon is related to the final active length of the small side of the flat bar passing through the corner of the rectangular box. Finally, the high slope of the curve with the low values of force at the end corresponds to the final active length of the flat bar reaching the pin.

The numerical model does not consider the effects of strain rate as a simplification. Despite the consideration of strain rate effects do not have significant changes on the material's yield stress and

the stress-strain relationship when considering quasi-static loading, the strain rate values increase the material's yield stress and changes the material's stress-strain behavior in the plastic domain. Therefore, it underpredicts stiffness, and the values of plateau force are underestimated.

The numerical model also considers a velocity of 1600 mm/s, which corresponds to 9600 cm/min. The justification for that is the high computational costs (approximately 80 h when considering a velocity of 50 cm/min for example) needed to represent the same velocities considered in the experimental tests. When compared to the velocities of the experiments (Appendix A), the numerical model uses a velocity with a value around 10^2 of difference. However, despite the large difference in the velocities considered, according to the results from Figure 5.5 it is possible to conclude that the velocity does not have influence on the results, which confirms the early assumptions based on Calladine and English. To verify that assumption, a feasibility test was performed. For that, the initial numerical model was considered with four different velocities. First, with 50 cm/min (8.333 mm/s) velocity with a time termination of 19.2 seconds, a second model with 100 cm/min (16.667 mm/s) velocity with a time termination of 9.6 seconds, a third model with 4800 cm/min (800 mm/s) velocity with a time termination of 0.2 seconds, and finally, the initial model with the velocity considered before (1600 mm/s corresponding to 9600 cm/min). The numerical results for the four models are represented in Figure 5.6.

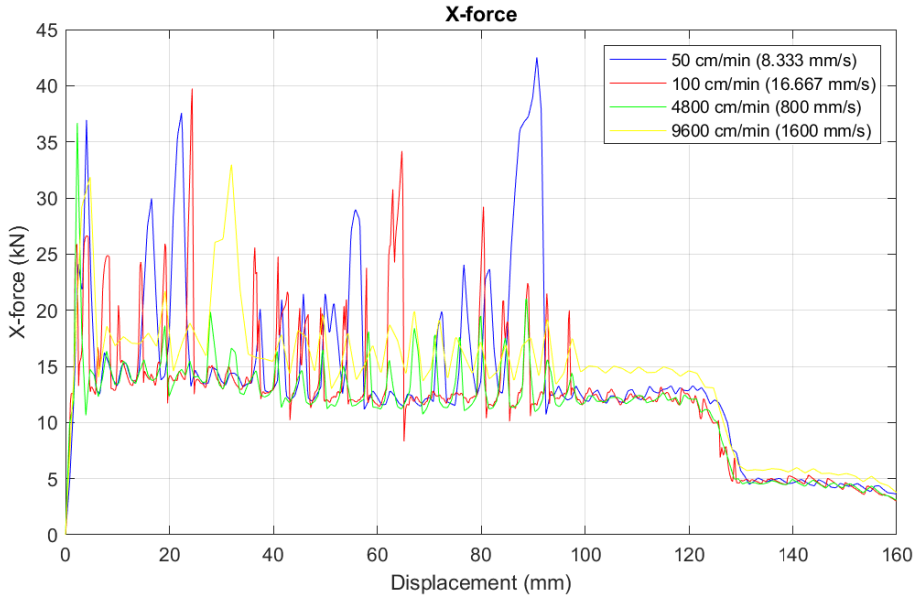

Figure 5.6: Feasibility test results regarding the influence of velocity on the numerical outcomes.

According to the results illustrated in Figure 5.6, it is possible to see that the difference in the plateau force for the three different velocities (50, 100, and 4800 cm/min) is not expressive and tends to be the same. The values of force tend to increase only with the 9600 cm/min velocity and can reach around 2 KN of difference. In Table 5.2, a comparison of the numerical results for the different speeds considered is presented.

Table 5.2: Comparison between numerical models with different velocities and the 50 cm/min (8.333 mm/s) numerical model.

	Average plateau force (kN)	50 cm/min (8.333 mm/s) (kN)	Error (%)
100 cm/min (16.667 mm/s)	14.76	15.04	1.91
4800 cm/min (800 mm/s)	13.02	15.04	13.47
9600 cm/min (1600 mm/s)	16.17	15.04	7.47

The difference in the values of force for the 9600 cm/min is not considered expressive and the numerical model is admitted to having a relatively good accuracy of the results for the same flat bar thickness. The conclusion that can be obtained from the feasibility test is that the velocity considered in the numerical model does not have expressive effects in the accuracy of the results and in the behavior of the proposed device, and the initial numerical model can be considered for further study in this master thesis.

The peaks of force are related to the contact between the flat bar and the walls and corners of the rectangular boxes, as explained before. The visible contact between the small side of the flat bar and the corner of the box wall is the cause of the visual peaks of force in the results, as described before. The consideration of different velocities can influence the way that the contact between the flat bar and the rectangular boxes is established. The different velocities can produce different peaks configurations. The visual force peaks for the different velocities considered in the numerical model traduce that fact. The non-existence of force peaks before the decrease in peak of the force is due to the final active length of the small side of the flat bar passing through the corner of the rectangular box, as described before. This phenomenon is the same for the different velocities' configurations, due to the active length considered for the small side of the flat bar being the same along the tests.

The influence that the rotation of the pin can impose on the numerical results was also studied for the considered values of friction. Therefore, the rotation of the pin on its axis was enabled in the initial numerical model. A small decrease in the plateau force is possible to observe for the consideration of rotation of the pin. A decrease in the force peaks is also described in the results. The numerical results are described in Figure 5.7, and the conclusion is that the rotation of the pin does not have much influence on the behavior of the mechanism and can be neglected for the considered friction coefficients. When comparing the average plateau force for both situations, the numerical results for the initial numerical model have an average percentage of error of 11% compared to the pin rotation.

The visible peaks at the beginning are related to the bending of the small side of the flat bar when contact with the rectangular box is established and increased force is reached. The lower peaks are related to the same justification described before for the initial numerical model.

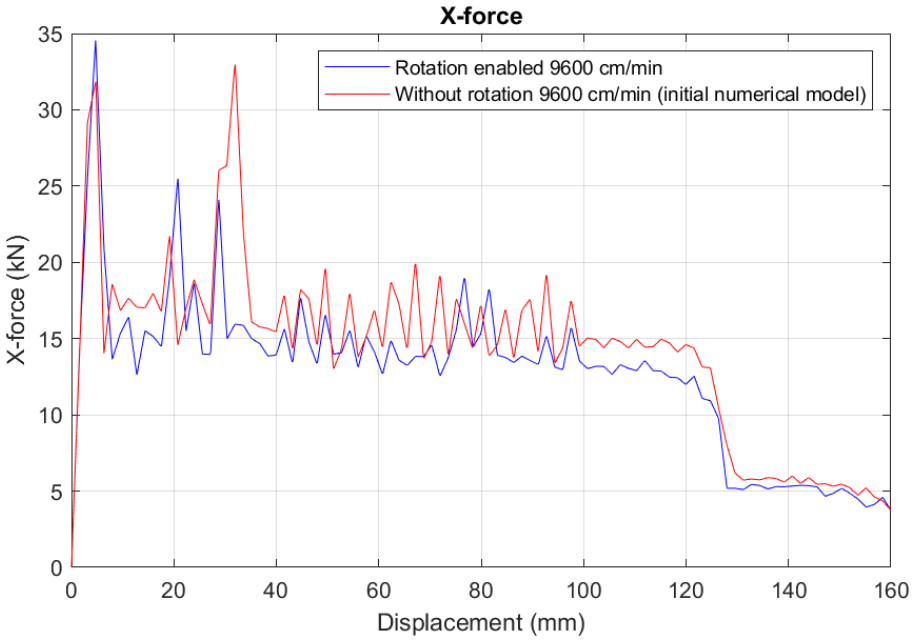

Figure 5.7: Numerical results with and without consideration of pin rotation.

A study of the numerical model considering a different thickness was also performed. The results for a 3 mm flat bar are illustrated in Figure 5.8. Despite the difference in values that can reach 3 MPa difference, it is possible to conclude that the numerical model continues to predict relatively well the behavior of the proposed mechanism. It is also possible to observe that the force peaks due to the contact between the corner of the rectangular box and the small side of the flat bar tend to be more softened when decreasing the flat bar's thickness. Given the diameter of the pin and the distance to the box walls is fixed, a smaller bar creates a bigger distance between the bar and the wall, which will impact the behavior, and the recorded peaks. The lower peaks tend also to decrease when decreasing the flat bar's thickness.

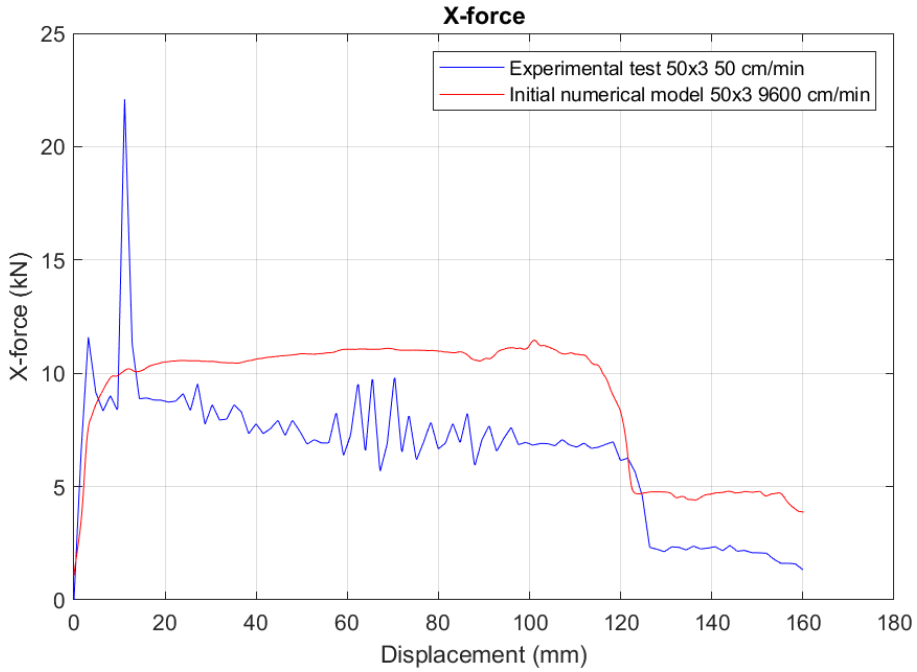

Figure 5.8: Numerical results for a 3-millimeter thickness and a comparison with an experimental result.

5.2.3 Strain rate effects - Steel

Different material models were considered to study the influence of strain rate effects on the results. The case study only considers the Cowper-Symonds and the Johnson-Cook material models.

The strain rate effects can be applied in the numerical model using the material model materialized by the keyword `024_PIECEWISE_LINEAR_PLASTICITY` by enabling the Viscoplastic Formulation (VP=1.0). This formulation considers the strain rate term of the Cowper-Symonds model [85]. The Viscoplastic Formulation to compute the dynamic yield stress in the function of the yield stress and the Cowper-Symonds term is illustrated in Equation 5.1,

$$\sigma_y(\varepsilon^p_{eff}, \dot{\varepsilon}^p_{eff}) = \sigma^s_y(\varepsilon^p_{eff}) + SIGY \times \left(\frac{\dot{\varepsilon}^p_{eff}}{C}\right)^{\frac{1}{p}} \tag{5.1}$$

Where, $\sigma^s_y\left(\varepsilon^p_{eff}\right)$ is the yield stress computed from the sum of the static stress, $SIGY$, the yield stress, $\dot{\varepsilon}^p_{eff}$, the strain rate, C and p, the Cowper-Symonds strain rate parameters from experimental data, and $\sigma_y(\varepsilon^p_{eff}, \dot{\varepsilon}^p_{eff})$, the dynamic yield stress [3].

For the case study, two different Cowper-Symonds parameters were chosen according to the literature: C = 40 (ms)-1 and P = 4 [90]; C=500 (ms)-1 and P = 4 [91]. The material properties of the standard steel used in the material model are described in Figure 5.3. The results for the two cases of the Cowper-Symonds parameter and a comparison with the results from two experimental tests are illustrated in Figure 5.9.

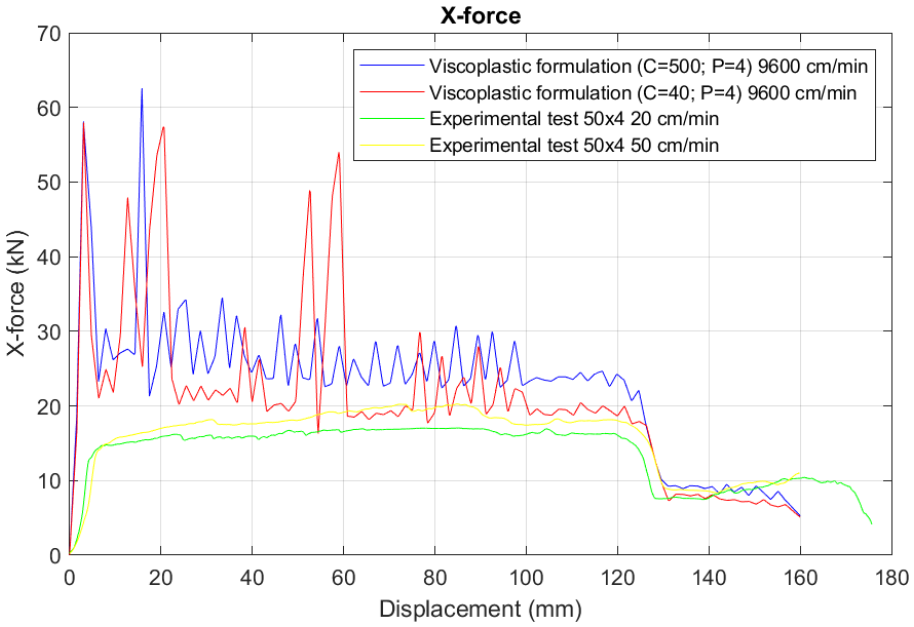

Figure 5.9: Numerical results considering two different cases of Copper-Symonds parameters and a comparison with two experimental results.

According to Figure 5.9, the Viscoplastic Formulation (C=500; P=4) predicts more accurately the experimental results when comparing to the Viscoplastic Formulation (C=40; P=4). The average plateau force for the numerical model with the Cowper-Symonds parameters C=500 and P=4 is 20.45 kN. In Table 5.3 is represented a comparison of the numerical results and the experimental ones for the same flat bar thickness.

Table 5.3: Comparison of numerical (Viscoplastic formulation (C=500; P=4)) and experimental results.

	Average plateau force (kN)	Viscoplastic formulation (C=500; P=4) (kN)	Error (numerical) (%)
Experimental test 50x4 20 cm/min	16.62	20.45	23.04
Experimental test 50x4 50 cm/min	18.86	20.45	8.46

It is possible to observe the difference in the results due to the consideration of strain rate effects. The values of force tend to increase and be approximate with the experimental results, as expected. It is possible to observe that, for the consideration of strain rate effects, the results tend to be more accurate for the final stage of the test, and in the average plateau force. The influence of the strain rate effects is visible in the numerical results when compared to the initial numerical model results without strain rate consideration represented in Figure 5.5. The peaks of force are related to the contact established between the small side of the flat bar and the corner of the wall during the process, as explained before.

The strain rate effects can also be considered using the Johnson-Cook material model. Using the keyword `098_SIMPLIFIED_JHONSON_COOK`, the simplified Johnson-Cook material model was applied for the numerical model. This material model considers the strain hardening and strain rate effects in flow stress. The thermal softening and adiabatic thermal effects are not considered in flow stress for this

material model. Equation 5.2 describes the material model considering, where A, B, C, and n are material parameters resultant from experimental data, $\bar{\varepsilon}^{p^n}$ the effective plastic strain, $\dot{\varepsilon}^*$ the normalized effective strain rate, and σ_y, the flow stress.

$$\sigma_y = (A + B\bar{\varepsilon}^{p^n})(1 + C \ln \dot{\varepsilon}^*) \tag{5.2}$$

The steel material properties for the simplified Johnson-Cook material model are based on existing literature [92] and are represented in Table 5.4.

Table 5.4: Steel material properties for the simplified Johnson-Cook material model [92].

$\rho[Kg/m^3]$	$E[GPa]$	$\nu[-]$	$A[GPa]$	$B[GPa]$	$n[-]$	$C[-]$
7850	210	0.30	280	667	0.72	0.071

The results from the simplified Johnson-Cook material and a comparison with experimental data are illustrated in Figure 5.10.

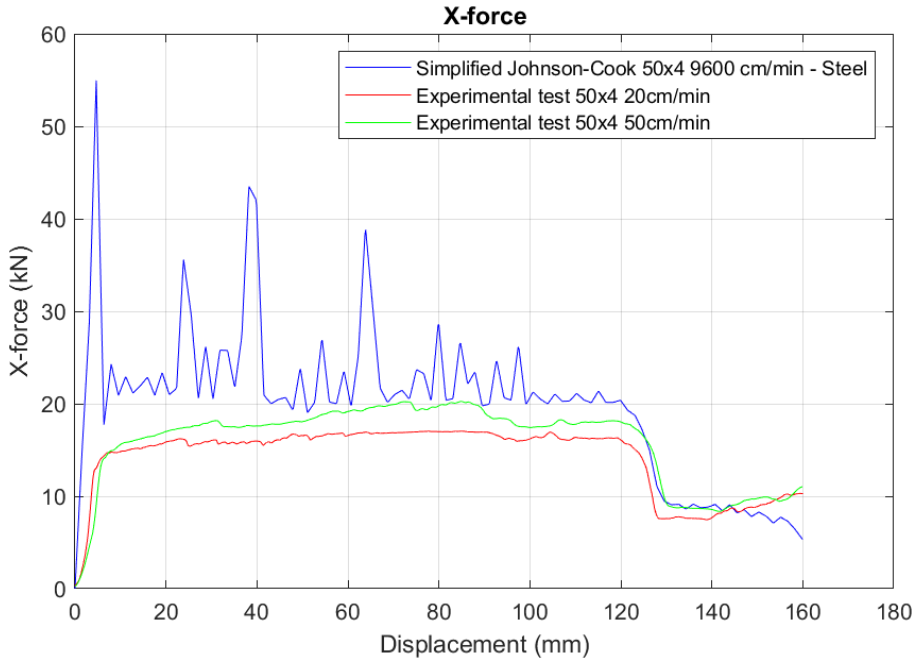

Figure 5.10: Numerical results for the simplified Johnson- Cook material model and a comparison with two experimental results.

From Figure 5.10, it is possible to observe that the numerical model can predict the behavior of the mechanism with a relatively good accuracy. The numerical model has a relatively good accuracy when comparing the numerical results with the experimental data. The plateau force from the numerical results is approximate with the experimental results. In Table 5.5 is represented a comparison of the numerical results and the experimental ones for the same flat bar thickness.

Table 5.5: Comparison of numerical (Simplified Johnson-Cook 50x4 - Steel) and experimental results.

	Average plateau force (kN)	Simplified Johnson-Cook 50x4 - Steel 9600 cm/min (kN)	Error (numerical) (%)
Experimental test 50x4 20 cm/min	16.62	20.53	23.60
Experimental test 50x4 50 cm/min	18.86	20.53	8.94

The influence of the strain rate effects is visible in the numerical results when compared to the initial numerical model results without strain rate consideration represented in Figure 5.5. For the consideration of strain rate effects, the results tend to be more accurate for the final stage of the test, and in the average plateau force. The peaks of force are related to the contact established between the small side of the flat bar and the corner of the wall during the process, as explained before.

According to the results mentioned in Figures 5.9 and 5.10, an increase of force can be observed due to the consideration of strain rate effects in the steel as expected. As referred before, the strain rate influences the material's yield stress and changes the material's stress-strain behavior in the plastic domain. The changes on the material's stress-strain behavior are reflected in the numerical results when compared to the numerical results without strain rate consideration from Figure 5.5.

The values are overestimated when compared to the experimental values. The effects of inertia remain negligible for quasi-static tests, as supported by the numerical results considering strain rates. In addition, no strain rate model was found in literature specifically for bending under tension. The plastic deformation mechanism for the UFBD is specific and therefore, the models selected might not reproduce accurately the phenomenon.

5.2.4 Initial numerical model – Aluminum

After verifying that the initial numerical model developed to reproduce the results extracted from the quasi-static tests made by Basto (Appendix A) can represent relatively well the behavior of the mechanism, it is valid to admit the use of the same numerical model to simulate the behavior of the mechanism when submitted to quasi-static and dynamic tests using an aluminum flat bar.

The initial modification made to the model in order to use an aluminum flat bar was changing the material properties and maintaining the same material model materialized by the Keyword `024_PIECEWISE_LINEAR_PLASTICITY` and the non-consideration of strain rate effects as a simplification. The results obtained for the aluminum and a comparison with the results from the initial model using steel are illustrated in Figure 5.11. The material properties of aluminum [83] and steel are also illustrated in Figure 5.11.

024_PIECEWISE_LINEAR_PLASTICITY (steel 50x4mm2)

Mass density (Kg/m3)	Young's modulus (MPa)	Poisson's ratio	Yield stress (MPa)	Tangent modulus %
7850	2.100e+005	0.30	304.00	540.00

024_PIECEWISE_LINEAR_PLASTICITY (aluminum 50x4mm2)

Mass density (Kg/m3)	Young's modulus (MPa)	Poisson's ratio	Yield stress (MPa)	Tangent modulus (MPa)
2987	6.900e+004	0.33	65.00	14.00

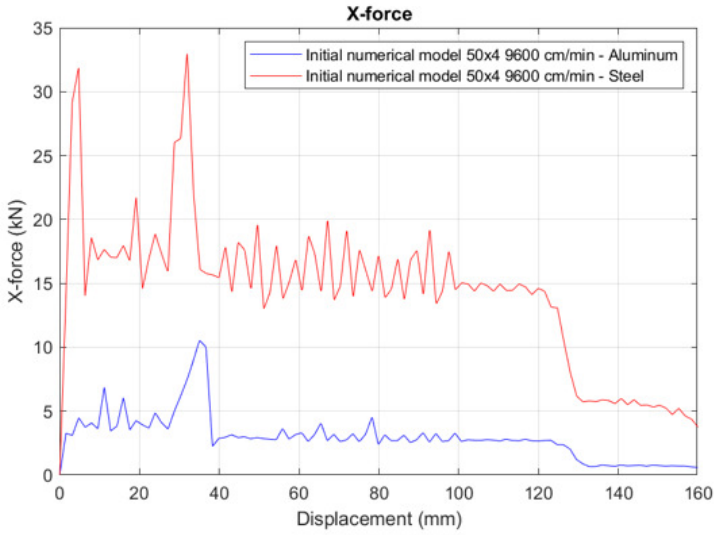

Figure 5.11: Comparison of the numerical results considering aluminum and steel flat bars.

The numerical models considered the use of a 50x4 mm^2 flat bar cross section. The force required for the aluminum flat bar during the process is much lower than the required values for steel, as expected. The visible force peaks due to the contact established between the active length of the small side of the flat bar and the corner of the rectangular box tend to decrease and disappear when considering an aluminum flat bar for the same conditions. The lower peaks due to the normal contact between the flat bar and the walls of the rectangular boxes tend also to decrease for the use of aluminum. According to the numerical results, using aluminum does not alter the behavior of the dissipative device, only its magnitude. Therefore, it can be considered an acceptable representative solution for a dynamic small scale laboratory test.

5.2.5 Strain rate effects - Aluminum

Since the main objective of this study is to simulate the proposed device under dynamic conditions using a blast load, using material models that consider the strain rate and temperature effects is important [72]. Therefore, a material model materialized by the Keyword `107_MODIFIED_JOHNSON_COOK` was applied.

The modified Johnson-Cook material model can account for calculating the strain rate, strain hardening, and thermal softening effects in flow stress. Adiabatic thermal effects are also considered in the calculation. The strain rate and temperature significantly influence flow stress and are assumed as coupled effects in flow stress in this material model. The equivalent flow stress depending on strain, strain rate, and temperature is given by:

$$\sigma(\varepsilon, \dot{\varepsilon}, T) = \left[A + B\varepsilon^n + \sum_{i=1}^{2} Q_i(1 - \exp(-L_i\varepsilon))\right]\left[1 + C\ln(\frac{\varepsilon}{\varepsilon_{\text{ref}}})\right]\left[1 - \left(\frac{T - T_0}{T_m - T_0}\right)^m\right] \tag{5.3}$$

Where A, B, C, m, n, Q_1, L_1, Q_2, and L_2 are material parameters, ε, the equivalent plastic strain, ε_{ref}, the strain reference, T, T_0, and T_m, represent the absolute, room and melting temperature respectively, and $\sigma(\varepsilon, \dot{\varepsilon},T)$, the equivalent flow stress depending on strain, strain rate and temperature [82, 83, 85].

The parameters applied in the modified Johnson-Cook mode are based on existing literature [82, 83] and are represented in Table 5.6.

Table 5.6: Modified Johnson-Cook parameters for the aluminum (EN AW-1050 H24) flat bar [82, 83].

$\rho[Kg/m^3]$	$E[GPa]$	$\nu[-]$	$XS1[-]$	$C_p[J/KgK]$	$\alpha[/K]$	$m[-]$	$T_m[K]$	$L_2[-]$
2710	69	0.33	0.9	899	$1.2e^{-5}$	1	293	533
$T_0[K]$	$A[GPa]$	$B[GPa]$	$n[-]$	$C[-]$	$Q_1[GPa]$	$Q_2[GPa]$	$L_1[-]$	
293	0.065	0.014	0.36	0.014	0.025	0.019	3324	

The parameters described in the present literature [82, 83] are referred to the commercial aluminum code EN AW-1050 H24. This type of aluminum is well known and studied by the authors for aluminum plates under dynamic conditions. The aluminum used in the experimental tests performed in this work is the same aluminum described in the literature. Therefore, this type of aluminum is adopted for the numerical study.

A numerical study of the system using this material was conducted by considering different thicknesses for the aluminum flat bar, and the results are illustrated in Figure 5.13. A comparison between the results without strain rate consideration and with the modified Johnson-Cook material model for the same thickness is illustrated in Figure 5.12.

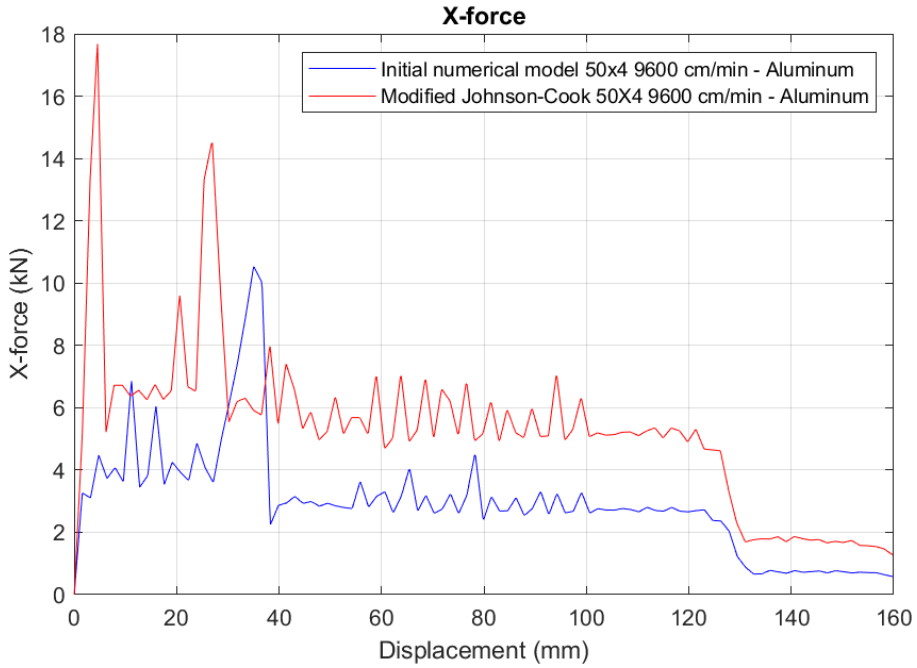

Figure 5.12: Comparison of the strain rate effects using the modified Johnson-Cook material model and without strain rate consideration for the same flat bar thickness.

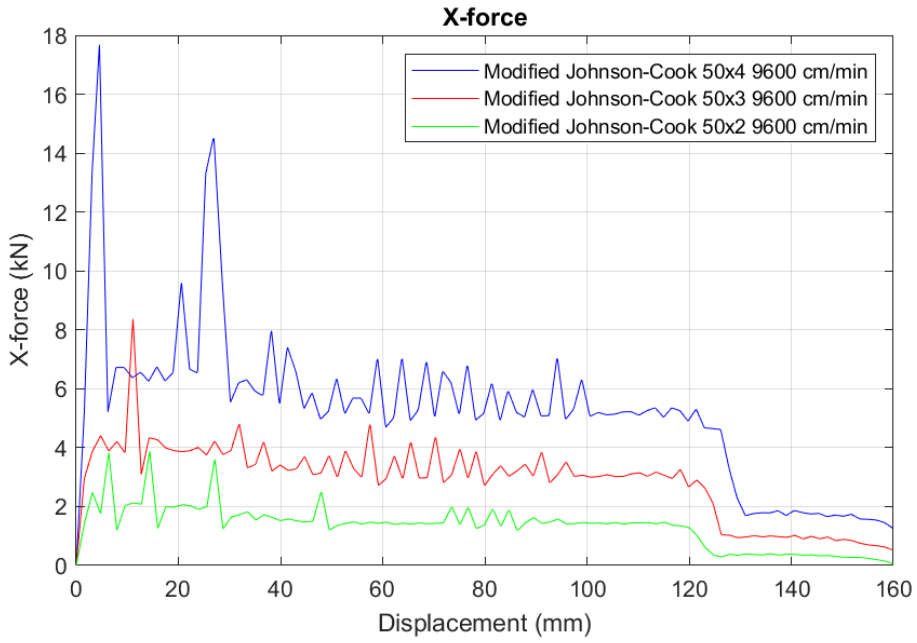

Figure 5.13: Numerical results for the modified Johnson-Cook material model considering lower thicknesses of the flat bar.

When considering the influence of strain rate effects on flow stress, the force values are relatively higher than those without strain rate consideration, as expected. The visible force peaks are due to the contact established between the active length of the small side of the flat bar and the corner of the rectangular box during the process, as explained before. The lower peaks are due to the normal contact between the flat bar and the walls of the rectangular boxes.

It is possible to observe that the required force for the unbending/bending mechanism is lower for lower thickness values. The force peaks tend to decrease and be more softener when decreasing the flat bar thickness, describing the same behavior, as observed for the steel flat bar.

According to the obtained numerical results for an aluminum flat bar, the force required for the unbending/bending mechanism is much lower when compared to the steel flat bar as expected. The device behavior does not change and it maintains a load-displacement curve typical of a Type I structure (according to Calladine and English), characteristic of energy dissipative devices.

The influence of the thickness of the flat bar in the resultant force is also studied, and it is possible to conclude that the force decreases for lower thicknesses. The force peaks tend also to decrease when decreasing the flat bar thickness, resulting in a more uniform force-displacement curve for the proposed device. The numerical study shows that the proposed device works relatively well for the proposed design.

These results are related only to quasi-static tests when the displacement applied to the flat bar is very small over time. When considering blast loading effects, the large amount of energy liberated in the form of an impulse leads to large displacements in a question of milliseconds.

5.3 Dynamic blast load numerical model

Considering the modifications implemented in the initial numerical model, a new numerical model has been developed to assess the design adapted for the UFBD under explosion loads. This new model follows a two-fold approach. Initially, it scrutinizes the behavior of the adapted mechanism through numerical simulations of quasi-static tests. Subsequently, the model is further adjusted to evaluate the performance of the UFBD under blast loading conditions.

5.3.1 Quasi-static test

Geometry

The specifications of the aluminum adapted device are explained in Chapter 4. The numerical model considers simplifications that save computational cost, without impacting the main objectives of the thesis. The numerical model considers the following parts (Figure 5.14):

- Flat bar: 2 mm thickness x 85 mm height x 311 (360 + 31+120) mm length;

- Pin: 20 mm radius x 100 mm height. The pin has been placed in direct contact with the flat bar since the beginning;

- 2 Rectangular boxes simulating the box walls: 5 mm thickness x 100 mm height x 60 mm length. These solid elements are placed with an 8 mm gap from the initial position of the flat bar.

- Rigid load applier: 2 mm thickness x 85 mm height x 8 mm length. The dimensions are not important for the case study as they do not affect the numerical results.

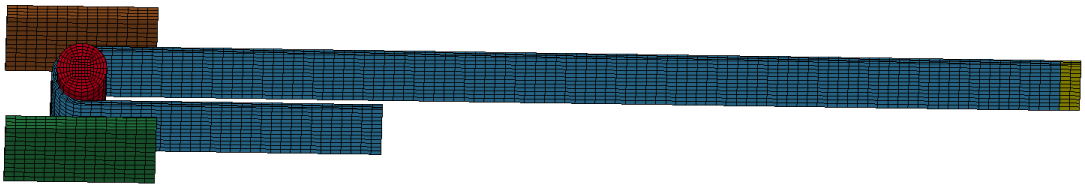

Figure 5.14: Red: Pin; Blue: Aluminum flat bar; Brown and green: Box walls; Yellow: Rigid load applier.

The proposed model considers 3D solid elements and a constant stress solid element with one integration point is used for modeling the following parts (ELFORM=1). For the deformable parts (flat bar), hourglass was defined, and Flanagan-Belytschko with exact volume integration form was applied. The model is made up of 13377 nodes, assembled in 9984 elements with a single interaction point.

Material models

The definition of the material models for the proposed model is based on the materials used in the experimental tests. The pin and the rectangular boxes are not supposed to deform permanently due to the plasticity phenomenon. Therefore, it is assumed that the rectangular boxes and the pin remain in the elastic region during the simulation, and the keyword `MAT_011_ELASTIC` is defined.

The aluminum used for the flat bar is the same in other studies for blast loading conditions [82, 83] with the commercial code EN AW-1050 H24. Therefore, the modified Johnson-Cook material model was applied using the Keyword `107_MODIFIELD_JOHNSON_COOK`. The present model is described before, and the parameters are based on existing literature [82, 83] and represented in Table 5.6.

Contact

The numerical model considers the Keyword `AUTOMATIC_SURFACE_TO_SURFACE` for the contact. In the contact definition, the aluminum flat bar is the ”Slave” entity, and the ”Master” is composed of rectangular boxes and the pin defined by the keyword `SET_PART`. Dynamic and static friction coefficients of 0.1 were applied for the contact between the considered parts for the same reasons described in the initial numerical model.

Boundary conditions and load

The mechanism needs to be fixed in all directions. Therefore, translational and rotational constraints were applied using the keyword `SPC_SET`.

The keyword `PRECRIBED_MOTION_RIGID` was defined to simulate the force applied in the flat bar during the quasi-static tests, and a 160 mm displacement in the X direction was applied to the rigid load applier. A time-displacement curve was defined using the keyword `DEFINE_CURVE`. In other words, a 160 mm displacement in the X direction was applied to the rigid load applier using a linear time displacement starting at zero and reaching 160 mm of displacement for 0.1 seconds. The model considers the time termination for the simulations to be 0.1 seconds.

Numerical results

The force-displacement curve resultant from the numerical model developed is illustrated in Figure 5.15.

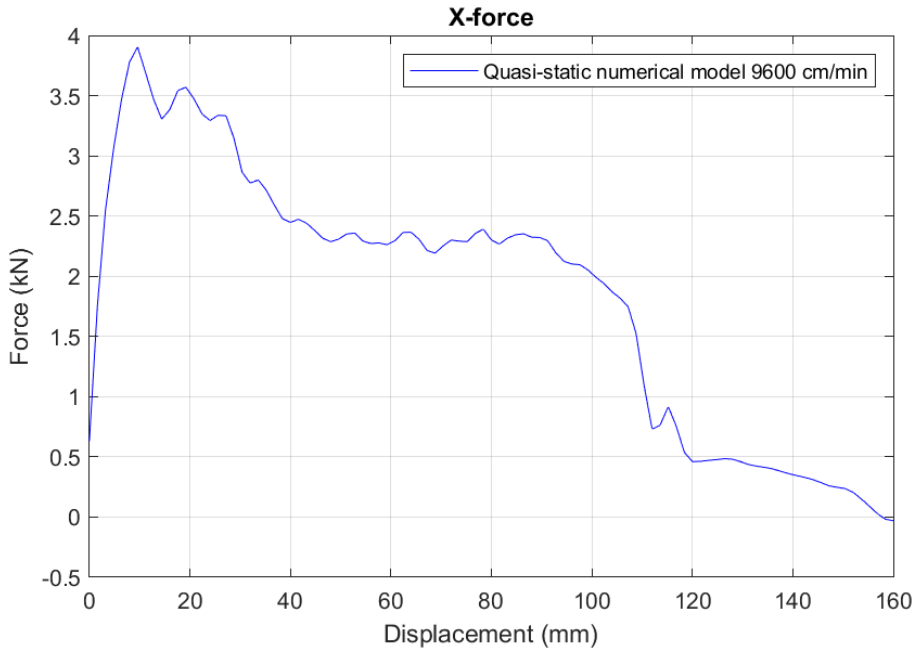

Figure 5.15: Force-displacement curve of the numerical model simulating the quasi-static tests.

The numerical results indicate a peak of force in the first 40 millimeters of displacement at the beginning of the bending/unbending mechanism, followed by a plateau force with an average value of 2.32 kN, and finally a decrease in peak in the resultant force reaching values close to zero. The decrease in peak of the resultant force is related to the final active length of the flat bar reaching the pin.

5.3.2 Blast loading

The numerical model was adapted to represent the behavior of the mechanism under dynamic conditions. The objective is to predict the behavior of the mechanism under blast loading conditions to evaluate and optimize the final solution chosen for the experimental campaign.

Set up

The concept of the numerical model is based on the solution described in Figure 5.16.

Figure 5.16: Experimental test of the device before the blast.

Geometry

As explained before, the specifications of the requirements for the proposed device are explained in Chapter 4. The numerical model considers simplifications since there is no need to represent all the specimens used in the experimental campaign. According to the requirements of Chapter 4, the numerical model considers the following parts (Figure 5.17):

- Aluminum flat bar: 2 mm thickness x 85 mm height x 511 (360 + 31+120) mm length;

- Pin: 20 mm diameter (20 mm steel) x 100 mm height. The pin has been placed in direct contact with the flat bar since the beginning;

- 2 Retangular boxes simulating the walls of the rectangular profile: 5 mm thickness x 100 mm height x 60 mm length. These solid elements are placed with a 8 mm gap from the initial position of the flat bar.

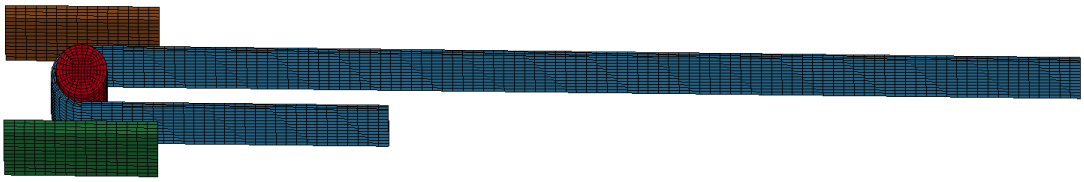

Figure 5.17: Red: Pin; Blue: Aluminum flat bar; Brown and green: Box walls.

The proposed numerical model considers 3D solid elements and a constant stress solid element with one integration point is used for modeling the following parts (ELFORM=1). For the deformable parts (flat bar), hourglass was defined, and Flanagan-Belytschko with exact volume integration form was applied. The model is made up of 13377 nodes, assembled in 9984 elements with a single interaction point.

The material models adopted are the same adopted for the previous model presented in Subsection 5.3.1.

The definitions established for the contact between the parts are also the same adopted for the previous model in Subsection 5.3.1.

Boundary conditions and load

The mechanism needs to be fixed in all directions. Therefore, translational and rotational constraints were applied using the keyword `SPC_SET`. To simulate the 60 mm piece of flat bar fixed on one side of the steel frame by using a piece of steel to clamp it, the Keyword `SPC_SET` was defined, and translational and rotational constraints in all directions were applied for the 60 mm of flat bar.

For the case study, the simulation of a blast wave reaching the surface of the flat bar using an EDST was performed considering a load curve. The experimental test described in Chapter 4 for blast loading considers using 10g of C4 positioned at 50mm from the entrance of an EDST with 80x80 mm^2 of square cross-section. A curve representing the reflected pressure measured at the end of the EDST for the same conditions can be found in the existing literature [84]. Based on the existing literature, the numerical model considers a load curve (Figure 5.18) for the reflected pressure at the end of the EDST.

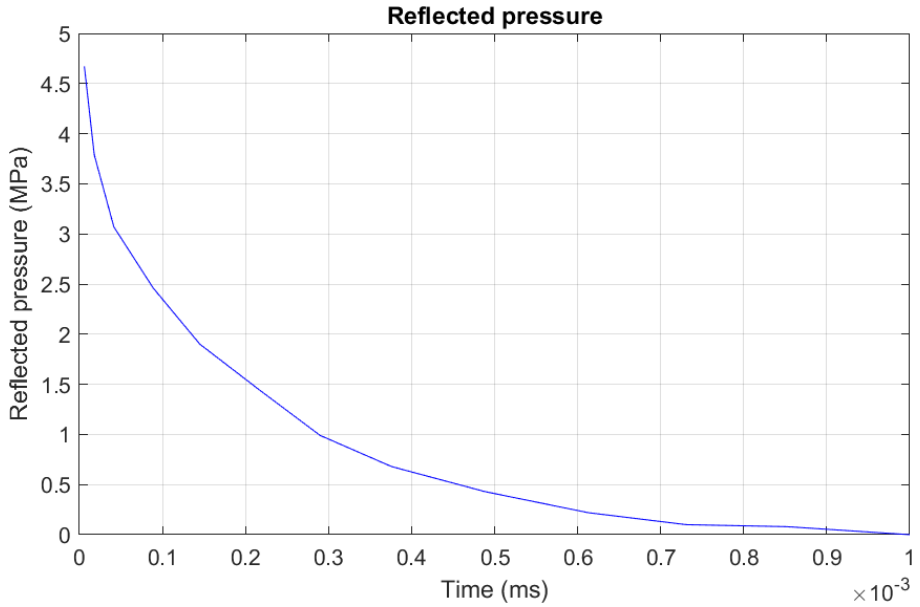

Figure 5.18: Reflected pressure at the end of the EDST (Adapted from [84]).

The load curve represented in Figure 5.18 is used in the numerical model to simulate the reflected pressure applied to the flat bar surface. The segments of the flat bar surface corresponding to the square cross-section of the EDST were defined using the Keyword `SET_SEGMENT`. The load curve was applied in the defined segments using the Keyword `LOAD_SEGMENT_SET`.

Numerical results

Sample deformation

A comparison of the samples a) before deformation and b) after deformation is illustrated in Figure 5.19.

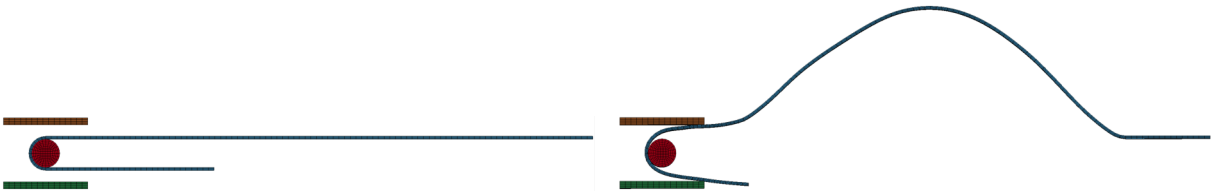

(a) Before deformation (b) After deformation

Figure 5.19: Sample deformation.

The active length of the small side of the flat bar at the beginning of the test is 120 millimeters. After the blast, the length decreased and a value around 65 millimeters is recorded. According to the active length and the sample's deformation after the blast illustrated in Figure 5.19, it is possible to conclude from the numerical model that the bending/unbending mechanism envisioned could work when subject to a blast loading test. According to the numerical results, it is expected that the flat bar can move between 50 to 60 millimeters around the pin. The sample's deformation after the blast provide a good indication of the behavior of the system, as the experimental tests in Chapter 6 depict.

Out-of-plane displacement

The experimental blast loading test performed and described in Chapter 6 uses high-speed cameras to measure the out-of-plane displacement of the flat bar. In the numerical model, the out-of-plane displacement is measured by extracting a displacement-time curve from the most distant element after the blast simulation. The numerical results for the out-of-plane displacement are represented in Figure 5.20.

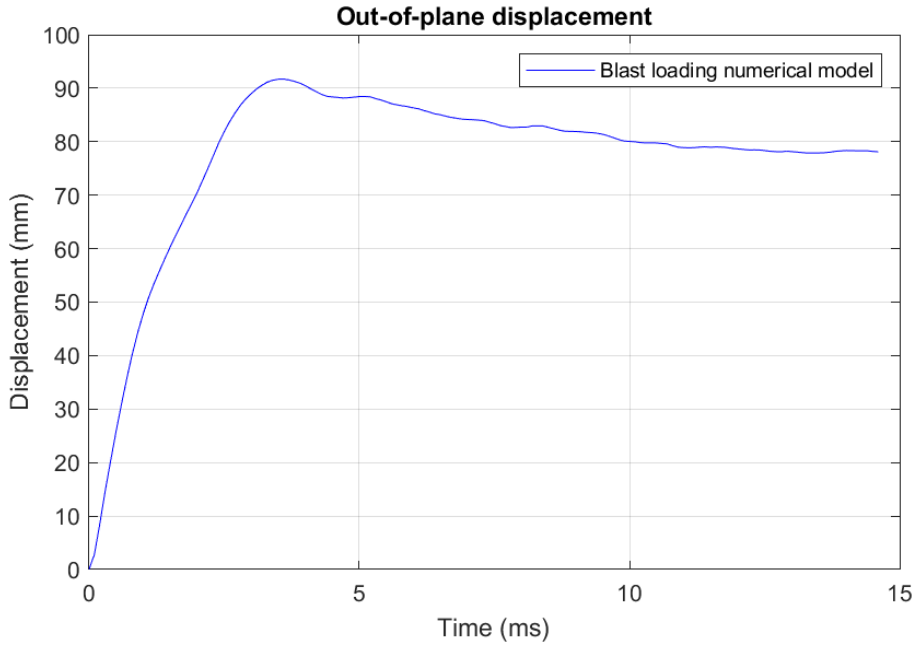

Figure 5.20: Numerical results for the maximum out-of-plane displacement.

According to the results from Figure 5.20, it is expected to have a maximum out-of-plane displacement around 90 millimeters. These values take into consideration the use of lubrification.

Chapter 6

Experimental Part

This chapter refers to the experimental tests developed for the UFBD. Aluminum samples tensile tests were performed to characterize the mechanical properties of the material used in the experimental tests. To perform the quasi-static and blast loading tests, a new adaption of the proposed device was considered to achieve the objectives of this thesis.

6.1 Tensile test

The aluminum is assumed to behave as an isotropic material and a tensile test was performed using two specimens cut in the same direction from an aluminum plate with two millimeters thickness. The objective is to characterize the mechanical properties of the aluminum such as tensile strength, yield strength and modulus of elasticity. The aluminum considered for the tests is the aluminum with the commercial code EN AW-1050 H24. According to the EN ISO 6892-1-2020 standard a “dog-bone” shape specimen was adopted for the tests. The dimensions of the specimen used are illustrated in Figure 6.1.

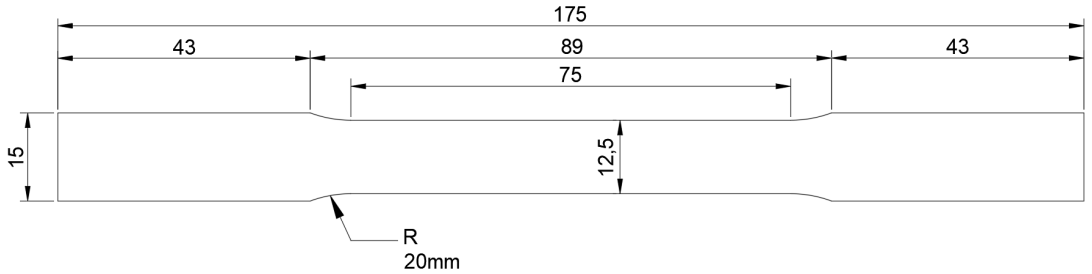

Figure 6.1: Drawing of the aluminum specimen according to the EN ISO 6892-1-2020.

The tensile tests were performed using a Zwick/Roell type test bench. To measure more accurately the Young’s modulus an extensometer was considered (Figure 6.2 (b)). The The set-up used for the experiments is represented in Figure 6.2. The tests were conducted using the test software Xpert by Zwick at a strain rate of 60 MPa/s (16.67 mm/min).

(a) without extensometer

(b) with extensometer

Figure 6.2: Tensile test of the aluminum specimen.

6.1.1 Results

The software Xpert by Zwick was used to extract the stress-strain curve of the respective specimens. As previously described, two aluminum specimens were utilized for the tensile tests, designated as Al10 and Al20. The stress-strain curves, characteristic of the aluminum specimens, are illustrated in Figure 6.3.

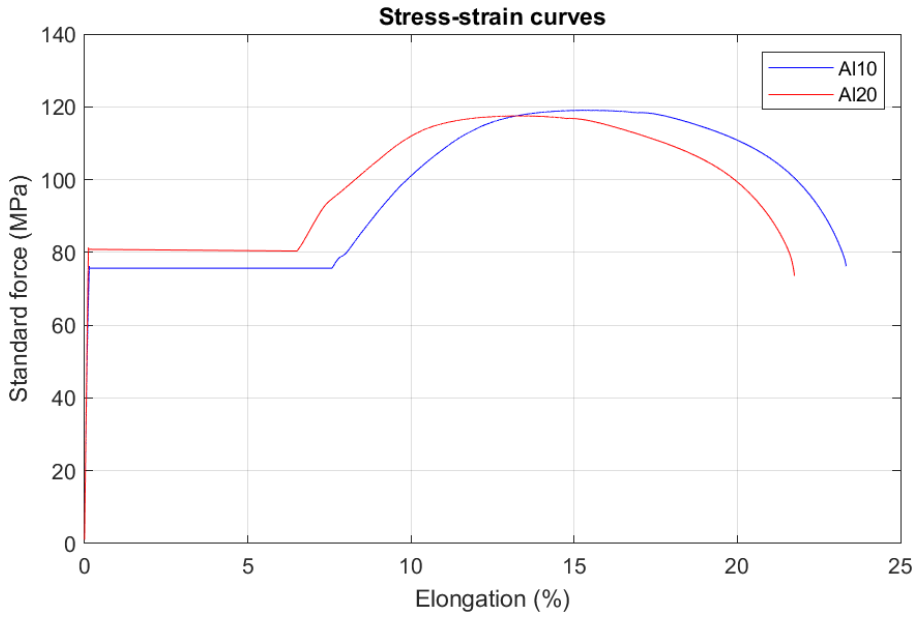

Figure 6.3: Stress-strain curves of the two specimens.

Based on the stress-strain curves presented above, it is possible to determine the mechanical prop-

erties of the aluminum specimens. Table 6.1 represents the mechanical properties of these aluminum specimens.

Table 6.1: Mechanical properties of a two millimeter thickness aluminum plate (EN AW-1050 H24).

$E[GPa]$	$67 \pm [64.63; 70.24]$	$\sigma_Y[MPa]$	$79 \pm [76.25; 81.34]$
$\sigma_M[MPa]$	$118 \pm [117.50; 119.10]$	$\sigma_B[MPa]$	$75 \pm [73.55; 76.17]$
$b[mm]$	12.42	$h[mm]$	1.98
$A_0[mm^2]$	24.59		

6.2 Quasi-static test

To characterize the design adopted to achieve the objectives of the thesis, quasi-static tests were performed.

Set-up

The quasi-static tests for the proposed device were performed using a Zwick/Roell type test bench. The whole set-up is illustrated in Figure 6.4 and 6.5. To help fix the mechanism box to the machine base, steel pieces suitable for this purpose were used. The pin was fixed to the mechanism box using two bolts and two circular pieces of steel to guarantee that the pin is well fixed to the mechanism. To apply a prescribed motion to one side of the flat bar is necessary to fix the flat bar to the machine. Two grooved pieces of steel needed to be considered to properly grip the flat bar to the machine, since it was not possible without it, due to the low thickness of the flat bar. The flat bar was submitted to a transverse velocity of 50 cm/min (500 mm/min equivalent), under normal temperature conditions (1 atm and 25 ºC). Before testing the flat bar samples, lubrication was considered to ensure the low friction required. The dimensions of the samples (flat bar) were measured and entered into the test software Xpert by Zwick before the tests to estimate the force applied and the sample's deformation.

(a) Detail of the grooved pieces of steel.

(b) Detail of the fixed box on the machine.

Figure 6.4: Details of the set-up for the qausi-static tests.

The experiment considers three repetitions of the tests using three similar flat bar samples to obtain the equivalent force-displacement curves.

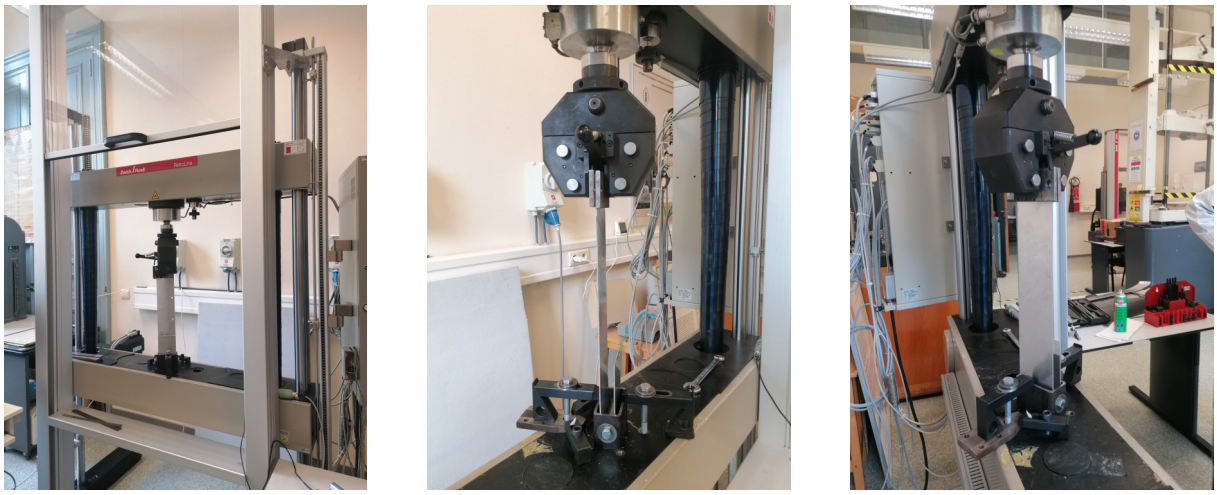

Figure 6.5: Quasi-static test configuration.

6.2.1 Results

As referred before, three tests were performed using lubrification. All three flat bar samples have the same measures, and a 50 cm/min prescribed motion was applied for each flat bar. The results for each test and a comparison with the numerical results are illustrated in Figure 6.6.

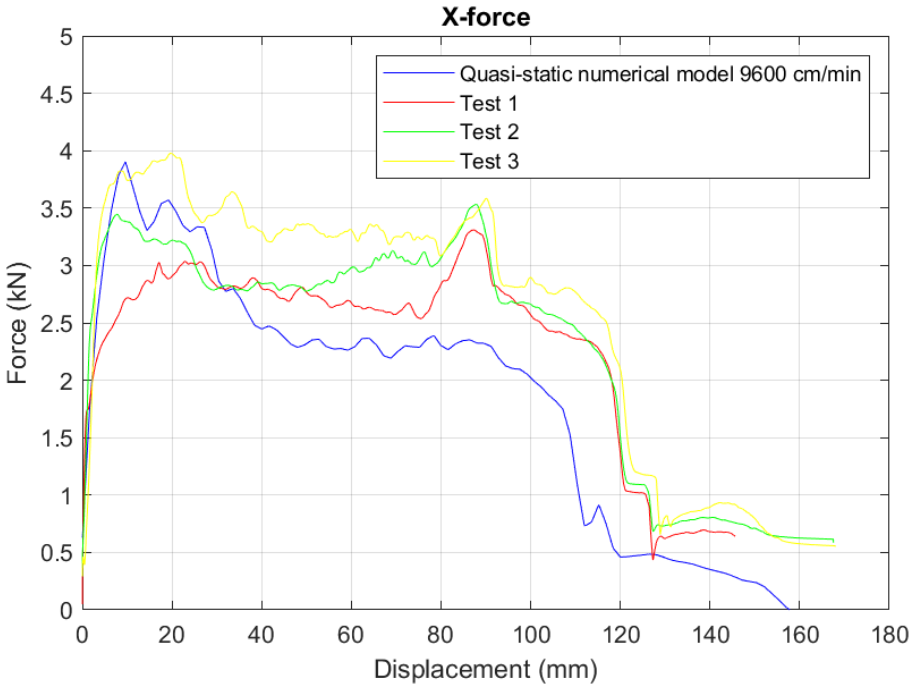

Figure 6.6: Experimental and numerical results of the quasi-static tests.

The results show that the mechanism has a “flat topped” static load-deflection curve, typical of a Type I structure.

According to the curves of to the experimental results, a peak of force is expected at the beginning of the test for the first 40 millimeters of displacement, when the flat bar is properly fixed to the machine and sliding does not occur. This phenomenon is more visible in the results of test 3 (Figure 6.6). During the repetition of each test, slippage of the grooved steel pieces responsible for gripping the flat bar to the machine during the initial phase of the displacement was observed. This results in measurement errors at the beginning of the displacement process, which are most noticeable in the results of tests 1 and 2, displaying a softer force peak for the first 40 millimeters.

The evidence illustrated in the literature related to the Continuous Bending Under Tension and described in Section 3.6 can be the justification for the initial peak of force when the flat bar starts to bend around the pin. The peak of force at the beginning of the tests can be justified with the increase of the material strength due to the accumulated strain during the pre-deformation of the material.

The experimental results show a small peak of force followed by a plateau force, corresponding to the plastic region due to the unbending/bending sliding mechanism of the flat bar. The high slope of the curve with the low values of force at the end corresponds to the final active length of the flat bar reaching the pin. The displacement corresponding to the final active length of the flat bar for the numerical model is different from the experimental samples. The numerical model considers a length of the small side of the flat bar of 120 millimeters. The samples used in the experimental tests have a length of the small side of the flat bar exceeding 120 millimeters, primarily due to the manual bending process applied to shape the flat bar around the pin. Given the manual nature of this process, the potential for measurement errors is notably elevated. Consequently, this underscores the necessity of commencing with a length of the small side of the flat bar exceeding 120 millimeters before the bending operation, ensuring a consistent 120 millimeters post-bending. However, after the bending process, the small side of the flat bar samples had a length higher than 120 millimeters. The experimental results for the three tests reflect this fact, as the high slope of the load-displacement curve occurs at displacements of more than 120 millimeters for the experimental results (Figure 6.6).

An average of the experimental results is represented in Figure 6.7 with a comparison with the numerical results.

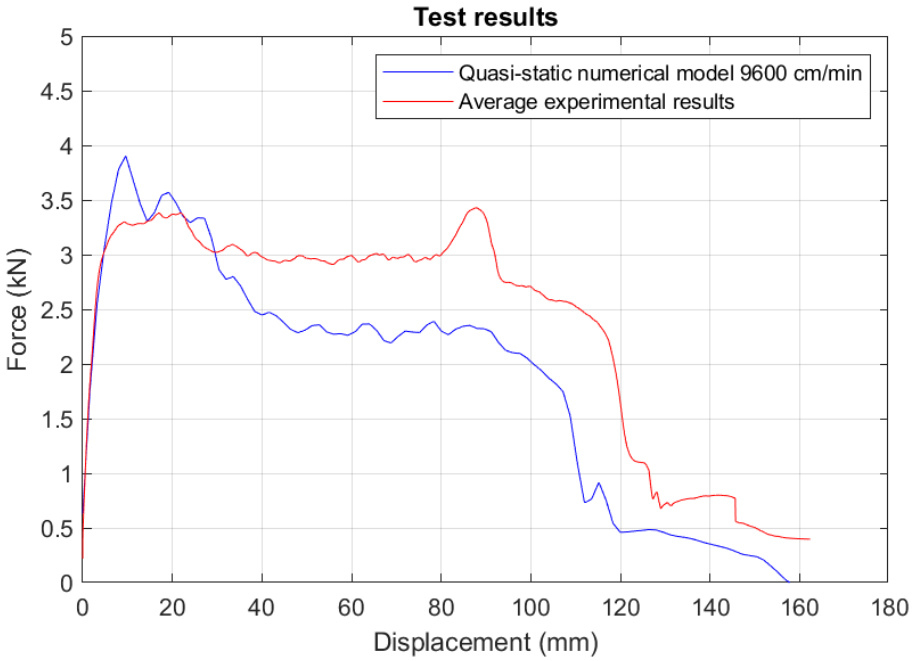

Figure 6.7: Comparison of the numerical results with the average of the experimental results.

From the average curve deduced from the experimental results, a plateau force of 2.86 kN is obtained. The corresponding value of plateau force from the numerical results is 2.32 kN. The numerical model can represent the experimental results with an error of 18.74 %. The percentage of error is relatively high when considering only the value, however, the numerical model can predict relatively well the behavior of the mechanism with around 1 kN difference on the plateau force. These results are illustrated in Table 6.2.

Table 6.2: Comparison between the numerical results (quasi-static numerical model) and the average of the experimental results.

	Average plateau force (kN)	Quasi-static numerical model 9600 cm/min (kN)	Error (numerical) (%)
Average experimental results	2.86	2.32	18.74

A comparison between the sample deformation and the numerical simulation is illustrated in Figure 6.8.

(a) Experimental sample deformation.

(b) numerical sample deformation.

Figure 6.8: Sample deformation.

It is possible to observe that the flat bar in the numerical model describes relatively well the real

behavior of the flat bar in the experiments. The deformation in the middle of the sample is different from the numerical model. The material model chosen, and the velocity considered in the numerical model (1600 mm/s = 9600 cm/min) can be the justification for the different deformation. The chosen velocity may introduce a plasticization configuration on the material that differs from what is expected at the actual velocity. Furthermore, as discussed in Chapter 3, the Johnson-Cook material model is particularly well-suited for extreme dynamic loading tests, where high strain rates induce significant changes in the material's plastic behavior. However, it may not be the most appropriate material model for quasi-static tests. It's worth noting that each material model accounts for the influence of strain rates on the material and its plastic behavior differently, making it potentially less ideal for this specific purpose. However, the numerical model can predict relatively well the load-displacement curve that characterizes the proposed mechanism.

6.3 Blast loading test

The numerical model shows a sample's deformation that can be acceptable as the expected deformation for the experimental tests.

Set-up

The set-up used for the tests is schematized in Figure 6.9. The set-up considered for the experiments can be divided into three main components. The first component refers to the whole elements used for the tests, namely the UFBD, steel frame and aluminum frame, the steel plates, the EDST, the explosive charge, the detonator, and the trigger. The second component is composed of the high-speed cameras and the LED lights. The cameras were defined to be synchronized for recording the footage simultaneously. Finally, the third component is the recording system needed to record data and the computer equipped with a data recording software (Photoron FASTCAM Viewer).

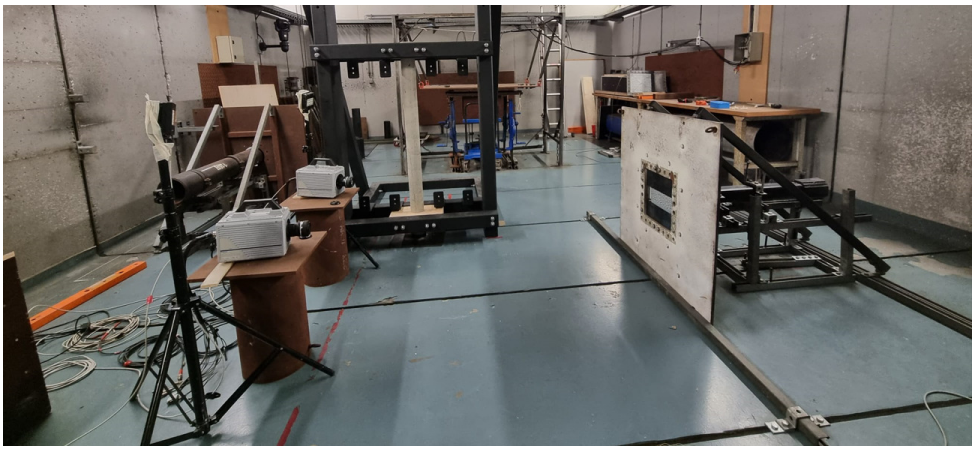

Figure 6.9: Overall view of the set-up.

The aluminum flat bar was painted with a speckle pattern on the side facing the cameras (Figure

6.10 (a)). This permits the cameras to exploit the images captured by Digital Image Correlation (DIC), and the deformation's calculation of the flat bar by color contrast. To measure the displacement inside the mechanism box, 2 cm distant lines were drawn on the small side of the flat bar (Figure 4.3 and 6.10 (b)).

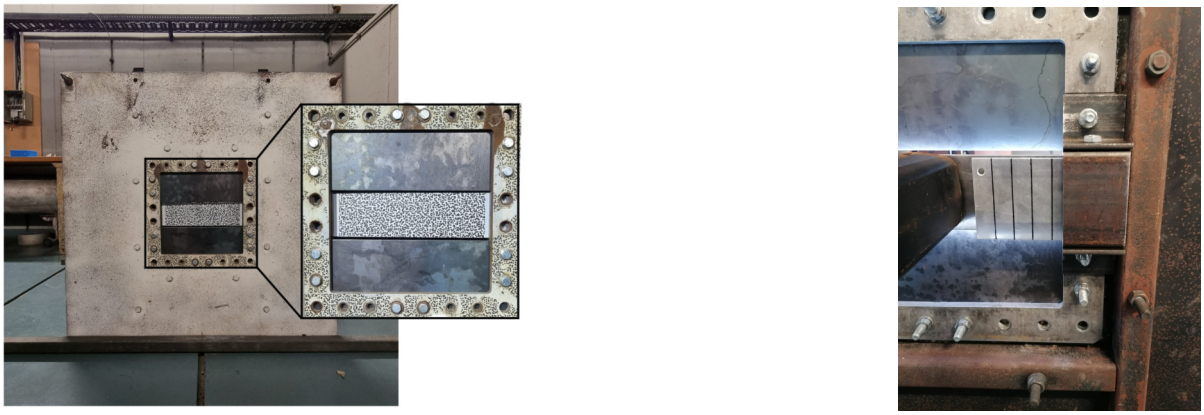

(a) Speckle pattern on the side facing the cameras.

(b) 2 cm distant lines.

Figure 6.10: Procedures to record data during the experiment.

A mass of 10g of C4 (equivalent to 13.4g of TNT) was prepared and positioned at 50 mm from the entrance of the EDST. For the case study, a 80x80 mm^2 square cross-section EDST was positioned perfectly in the middle of the flat at 4 mm distance from its end. The center of the EDST is positioned 45 mm from the ground. The cross-section of the tube is perfectly aligned with the flat bar surface. The small charge used is considered a good choice for this initial phase, when the objective is to avoid the risk of the flat bar possibly failing due to the high pressures.

To guarantee that the high-speed cameras capture correctly the imagines two steel plates were positioned to prevent blast's wave light and smoke from reaching the side facing the cameras (Figure 6.10 (a) and 6.11).

Figure 6.11: Different views of the set-up.

Three tests were performed: the first one without lubrification, and the second and the third with lubrification. Conducting a test without the use of lubrication is intended to analyze the impact of lubrication

on the mechanism's performance when subject to blast loading tests.

6.3.1 Results

1st Test

From the images (Figure 6.12) it is possible to observe that the flat bar deformed and there is no failure in the material. The 2 cm distant lines indicate that the flat bar moved around the pin inside the mechanism box. The small side of the flat bar moved around 40 mm inside the mechanism box. The maximum out-of-plane displacement registered from the cameras is 75 mm.

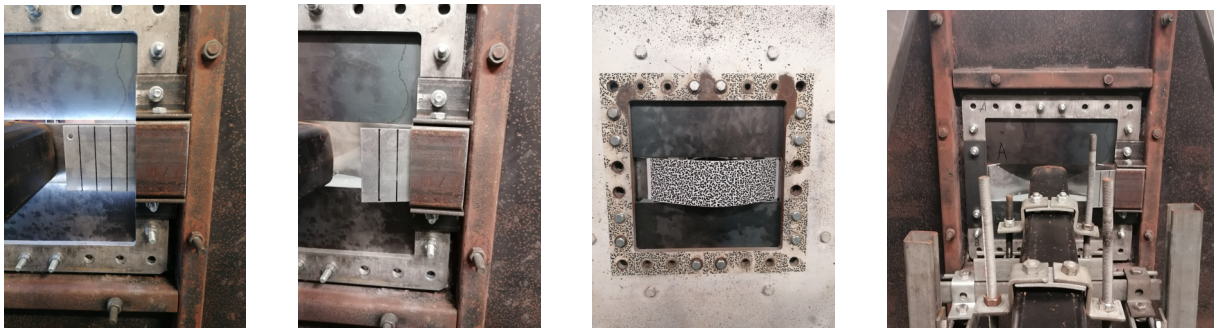

Figure 6.12: 1st Test results.

2nd Test

The small side of the flat bar moved around 60 mm inside the mechanism box (Figure 6.13), the maximum movement registered in the three tests. The maximum out-of-plane displacement registered from the cameras is 86 mm, also the maximum value registered in the three tests. A flat bar wear was also observed due to the contact between the flat bar and the sharp angle of the box walls.

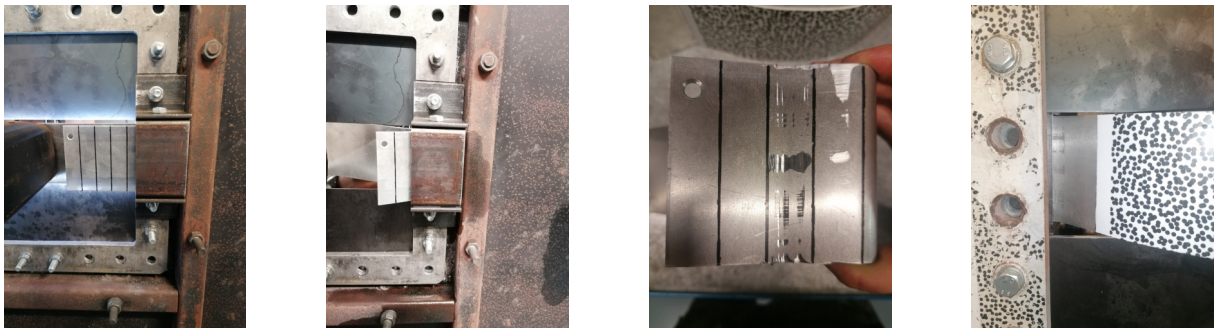

Figure 6.13: 2nd Test results.

3rd Test

The small side of the flat bar moved around 40 mm inside the mechanism box (Figure 6.14). The maximum out-of-plane displacement registered from the cameras is 75 mm. A flat bar wear was also observed due to the contact between the flat bar and the sharp angle of the box walls.

Figure 6.14: 3rd Test results.

Out-of-plane displacement

In Figure 6.15 is represented the respective curves obtained from each test using the images captured by Digital Image Correlation (DIC) and a comparison with the numerical model.

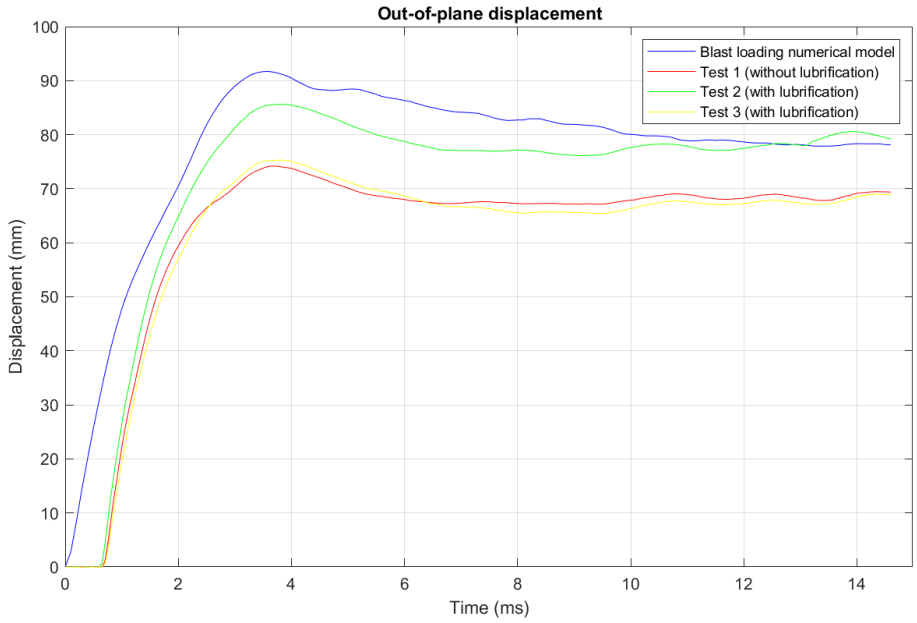

Figure 6.15: Out-of-plane displacement registered in the three tests.

In Table 6.3 are represented the maximum values of out-of-plane displacement for the first, second, and third tests, and also for the blast loading numerical model.

Table 6.3: Maximum values of out-of-plane displacement.

	Out-of-plane displacement (mm)
Test 1 (without lubrification)	75
Test 2 (with lubrification)	86
Test 3 (with lubrification)	75
Blast loading numerical model	92

The numerical model overestimates the results when compared to the experimental results. The reason for the lower values observed in the experimental results can be attributed to the sharp corners of the mechanism's walls, which contribute to the wear of the flat bar during the tests. This, in turn, results in increased friction within the mechanism, thus impeding the movement of the flat bar inside the mechanism. The friction resulting from the contact can increase the force needed for the flat bar to bend around the pin and decrease the out-of-plane displacement for the experimental results. The lubrification considered for the experiments can also be another justification for the lower values of out-of-plane displacements. The lubrification used is a simple spray that can be compared to a product similar to WD40 [93], which is not the best solution for the case, when a lot of contact between the surfaces occurs, and the spray can easily disappear.Moreover, considering the experimental results, it can be concluded that the application of lubrication to the mechanism did not influence its performance. This is evident from the fact that an identical maximum out-of-plane displacement result was achieved, both when lubrication was applied (test 3) and when it was not applied (test 1). It can be once again concluded that the considered lubrication is not ideal for the specific situation in question.

In Figure 6.16 is illustrated the average values of out-of-plane displacement for the experimental results of test 2 and 3 (with lubrification) and a comparison with the numerical results. Considering the maximum values, the numerical model represents the results with an error of 14.00%. The average value is 80.43 millimeters. According to the estimated error and the similarity of the curves, it is possible to consider that the numerical model can represent the proposed model with a relatively good accuracy.

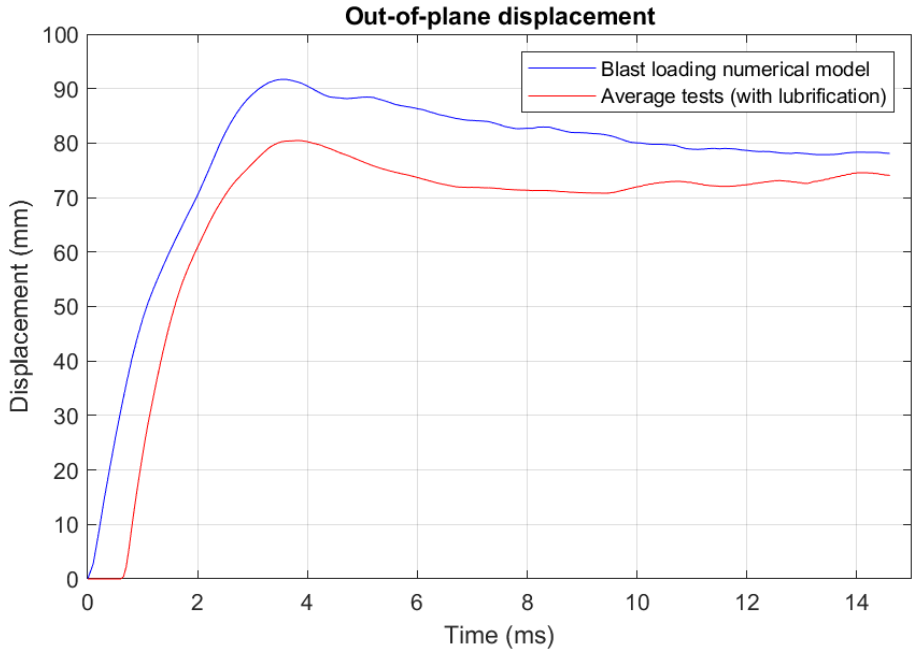

Figure 6.16: Comparison of the average experimental results with the numerical results.

The three sample's deformations are illustrated in Figure 6.17. A comparison of the sample deformations with the numerical results is also illustrated. It is possible to conclude that the numerical model can reproduce the behavior of the flat bar after the blast with a relatively good accuracy. The sample's

deformation shows that the failure of the aluminum flat bar does not occur.

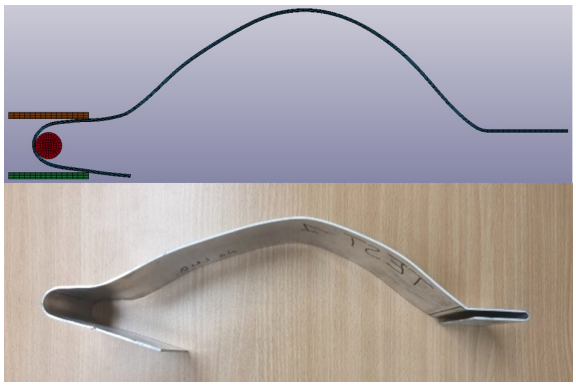

(a) Numerical sample deformation (above) and sample deformation (below).

(b) Three sample deformations.

Figure 6.17: Sample deformation after the blast.

Chapter 7

Concluding Remarks

7.1 Synthesis and main conclusions

The work developed under the present dissertation builds upon previous research conducted on blast resistance systems working under the principle of energy absorption or dissipation, through plastic deformation. It is an expanding area of research, drawing on the vast body of knowledge on energy absorbers.

The objective of the dissertation was to characterize and analyze the dynamic behavior of a U-shaped Dissipative Flat Bar Bending device (UFBD), when subject to blast loading. It's point of departure was the hypothesis supported by Calladine and English [9], that quasi-static tests of Type I dissipative devices are good predictors of their dynamic behavior, an hypothesis that was proved valid for the UFBD design.

The work conducted was initially based on numerical modelling and simulation, developed in the software Ls-Dyna. This allowed the development, experimentation, and optimization of a solution that could be tested at the Royal Military Academy (RMA) blast laboratory, resorting to a Shock Tube.

The numerical modelling phase allowed to analyze the effects of strain rate and friction in the behavior of the UFBD as well as the influence of certain design properties, such as the rotation of the pin and the variation in the thickness of the flat bar.

It confirmed, as expected, that strain rate effects influence the dynamic behavior the UFBD. Despite no specific models to consider strain rate effects on bending/unbending flat bars were found in literature, the modified Johnson-Cook strain rate models showed to reproduce well the effects of strain rate in numerical modelling, as the comparison of the numerical and experimental results reveal (error of 8.94%).

The numerical simulations also suggest that for the test velocity does not have relevant effects on the accuracy of the results, as the comparison with the experimental results depict (error of 1.22%). The numerical model developed considered a different velocity to represent the same results of the experimental campaign. The considered velocity, although high when compared to that used in the experimental tests, may fall within an acceptable range (9600 cm/min = 1.6 m/s) for the unbending/bending phenomenon of the mechanism without causing significant alterations to its operation. Additionally, this

revealed as a good solution to minimize the computational costs and improve the numerical work.

In order to execute experimental tests at the RMA blast laboratory, it was necessary to create a set up that could reproduce the UFBD mechanism when subject to the blast loading produced by the laboratory Shock Tube. Aluminum was adopted initially, for its greater ductility, and numerical simulations were conducted to evaluate the behavior of the UFBD when compared to the original steel design. It was verified that the aluminum design, compared with the steel design, replicates well the unbending/bending phenomenon and maintains a force-displacement curve typical of a Type I structure.

During the experimental campaign, quasi-static tests and dynamic tests were conducted and compared to their respective numerical simulations. The results from the numerical model developed to characterize the Aluminum design adopted were validated by the results from the quasi-static tests. The initial peak of force described in the numerical model is in accordance with the experimental results. The numerical results underestimate the value of plateau force from the experimental results by 18.74%, however, the numerical model can represent relatively well the behavior of the UFBD.

The dynamic blast load experimental tests confirmed that the UFBD works as intended when subject to blast load, producing the unbending/bending mechanism as well as an out-of-plane displacement. These indicate that the UFBD can dissipate energy from the blast into the form of plastic deformation due to the unbending/bending phenomenon of the flat bar around the pin.

A feature explored during the experimental campaign was the use of lubrication in the system. While in quasi static tests, lubrication reduces the net value of the plateau force, as the tests previously conducted in steel design depict, in blast loading tests, higher (14.66%) out-of-plane displacement was registered using lubrification.

Lastly, the numerical model for the UFBD subject to blast load was validated by the experimental tests. It overestimates the maximum out-of-plane displacement by 14.00%, however, this error is not considered expressive, and it can be assumed that the numerical model predicts well the dynamic behavior of a UFBD subject to a blast load.

By demonstrating by numerical simulation and experimental tests that the dynamic behavior of the UFDB can produce the unbending/bending mechanism for which it was designed, maintaining a force-displacement curve typical of a Type I structure, the objectives of this theses were successfully achieved.

7.2 Recommendations for future work

During the research work, some aspects that could be improved were identified:

- Due to the out of plane displacement produced in the flat bar, the design of the box walls should be revised by softening the box edges in contact with the flat bar to facilitate the unbending/bending phenomenon inside the mechanism box and prevent the wear and possible rupture of the flat bar;

- Based on the existing numerical models, parametric study of the UFBD could be performed to identify the optimal design considering the influence of the diameter of the pin, mechanism box dimensions, gap considered, and flat bar dimensions;

- Strain rate effects during the unbending/bending phenomenon inside the mechanism box could be

further investigated in order to more accurately predict the behavior of the UFBD when subject to blast loads;

- Analysis of the shear failure of the bar should be further investigated, to understand the limitations of the system design.

Bibliography

[1] G. S.R. Shipping out: Iso-based deployment systems. https://www.defensemedianetwork.com/stories/shipping-out-iso-based-deployment-systems/, june 2010.

[2] Minusca - mission intégrée pour la stabilisation en république centrafricaine. https://untalent.org/jobs/camp-manager-6, may 2023.

[3] Global terrorism index 2023. https://reliefweb.int/report/world/global-terrorism-index-2023, 2023.

[4] G. T. Database. https://www.start.umd.edu/gtd/, 2023. Accessed on 15/10/2023.

[5] A.-H. S., D. H. R., M. S., K. H., K. F., and D. R. Beirut ammonium nitrate blast: Analysis, review, and recommendations. *Front. Public Health*, 9, 2021. doi: https://doi.org/10.3389/fpubh.2021.657996.

[6] G. M. D. Cornie and P. Smith. *Blast effects on buildings*. ICE Publishing, London, 2009.

[7] M. Walker. An energy-dissipating system for blast mitigation in structures. Master's thesis, University of Toronto, 2012.

[8] M. V. Seica, J. A. Packer, M. G. Walker, and M. I. Gow. Mitigation of blast effects through novel energy-dissipating connectors. *International Journal of Protective Structures*, 13(2):236–272, 2022. doi: 10.1177/20414196221074058.

[9] C. R. Calladine and R. W. English. Strain-rate and inertia effects in the collapse of two types of energy-absorbing structure. *International Journal of Mechanical Sciences*, 26(11-12):689–701, 1984. doi: 10.1016/0020-7403(84)90021-3.

[10] J. Basto. Performance assessment of a u-shaped dissipative flat bar bending device for blast protection. Research project, Departament of Civil Engineering of NOVA University, 2022.

[11] A. G. T. D. Ngo, P. Mendis and J. O. Ramsay. Blast loading and blast effects on structures – an overview. *Electronic Journal of Structural Engineering*, Jan. 2007. doi: 10.56748/ejse.671. URL `https://doi.org/10.56748/ejse.671`.

[12] A. L. H. J. S. Keller, M. Gresho and A. V. Tchouvelev. What is an explosion? *International Journal of Hydrogen Energy*, 39(35), Dec. 2014. doi: 10.1016/j.ijhydene.2014.04.199. URL v.

[13] G. Gomes. *Reutilizção de edificios correntes para fins operacionais - Blast assessment*. Instituto Universitário Militar, 2016.

[14] U. 3-340-02. Structures to Resist the Effects of Accidental Explosions. *Struct. Congr. 2011*, page 1867, dec 2008.

[15] P. F. Acosta. Overview of UFC 3-340-02 Structures to Resist the Effects of Accidental Explosions. *Structures Congress*, page 1454–1469, 2011.

[16] E. Yandzio and M. Gough. Protection of buildings against explosions. *SCI Publ. 244*, page 110, 1999.

[17] S. B. Janney. Blast resistant design of steel structures. Master's thesis, University of Tennessee - Knoxville, 2007.

[18] S. R., A. C., E. M., and K. M. *Reference Manual to Mitigate Potential Terrorist Attacks Against Buildings*. Fema, 2011.

[19] L. A. and A. F. Blast resistant design with structural steel. common questions answered. *American Institute of Steel Construction*, 43(10):61–66, 2008.

[20] G. F. Kinney and K. J. Graham. *Explosive Shocks in Air*. Springer Berlin, Heidelberg, 1985.

[21] D. O. Dusenberry. *Handbook for blast-resistant design of buildins*. John Wiley and Sons, Inc., New Jersey, 2010.

[22] *14 TM 5-1300 Structures to resist the effect of accidental explosions*. U.S.Department of the Army, Navy, and Air Force, Washington, D.C, 1990.

[23] G. Karlos, V. Solomos. Calculation of blast loads for application to structural components. Technical report, European Commission, 2013.

[24] V. Karlos, G. Solomos, and M. Larcher. Analysis of the blast wave decay coefficient using the kingery–bulmash data. *International Journal of Protective Structures*, 7(3):409–429, 2016. doi: 10.1177/2041419616659572.

[25] C. E. Needham. *Blast Waves. Shock Wave and High Pressure Phenomena*. Springer Berlin, Heidelberg, 2010.

[26] UNODA. International ammunition technical guideline (united nations saferguard). page 21, 2011.

[27] H. Ousji, B. Belkassem, M. A. Louar, D. Kakogiannis, B. Reymen, L. Pyl, and J. Vantomme. Parametric study of an explosive-driven shock tube as blast loading tool. *International Journal of Mechanical Sciences*, 40(4):1307–1325, 2016. doi: 10.1007/s40799-016-0128-3.

[28] M. A. Louar, B. Belkassem, H. Ousji, K. Spranghers, D. Kakogiannis, L. Pyl, and J. Vantomme. Explosive driven shock tube loading of aluminium plates: experimental study. *International Journal of Impact Engineering*, 86:111–123, 2015. doi: 10.1016/j.ijimpeng.2015.07.013.

[29] A. Caçoilo. Blast wave propagation in confined spaces and its action on structures. Phd thesis, The University of Edinburgh, 2018.

[30] J. Renshaw and L. Sanicola. U.s. meets with refiners on high pump prices; no plan yet -sources. https://www.reuters.com/markets/commodities/us-oil-refiners-meet-biden-officials-high-stakes-price-talks-2022-06-23/, june 2022.

[31] H. Hao and L. Z. *Advances in Protective Structures Research*. CRC Press, 2012.

[32] I. McGrath RentCorp. From barracks to bedrooms: Understanding military shipping container housing. https://www.mobilemodularcontainers.com/blog/barracks-bedrooms-understanding-military-shipping-container-housing, 2022.

[33] E. I. S. LTD. Ban-air. http://ban-air.com/products/deployables/container-optimization, 2023.

[34] T. Børvik, A. G. Hanssen, S. Dey, H. Langberg, and M. Langseth. On the ballistic and blast load response of a 20 ft iso container protected with aluminium panels filled with a local mass — phase i: Design of protective system. *Engineering Structures*, 30(6):1605–1620, 2008. doi: 10.1016/j.engstruct.2007.10.010.

[35] T. Børvik, A. G. Hanssen, M. Langseth, and L. Olovsson. Response of structures to planar blast loads – a finite element engineering approach. *Computers and Structures*, 87(9):507–520, 2009. doi: 10.1016/j.compstruc.2009.02.005.

[36] G. A. Hegemier, L. K. Stewart, and B. J. Durant. Blast resistant module development and testing. Technical report, Protective Technologies, 2013.

[37] T. Børvik, A. Burbach, H. Langberg, and M. Langseth. On the ballistic and blast load response of a 20ft iso container protected with aluminium panels filled with a local mass — phase ii: Validation of protective system. *Engineering Structures*, 30(6):1621–1631, 2008. doi: 10.1016/j.engstruct.2007.10.011.

[38] T. Anderson, B. J. Horn, J. K. Thomas, and L. Magenes. Deflagration load generator blast load testing of an iso shipping container and blast resistant wood building. In *American Society of Civil Engineers Structures Congress*, 2017.

[39] L. Changzhou Magindustry Co. Blast-proof shelter. https://www.magindustry.com/product/Blast-Proof-Shelter.html, 2023.

[40] E. I. M. B. Solutions. Ebtech container manufacturing: Blast and ballistic protected. https://www.ebtechindustrial.com/blast-ballistic-containerized-buildings-bunkers/, 2023.

[41] A. A. A. Alghamdi. Collapsible impact energy absorbers: an overview. *Thin-Walled Structures*, 39 (2):189–213, 2001. doi: 10.1016/s0263-8231(00)00048-3.

[42] W. Johnson and S. R. Reid. Metallic energy dissipating systems. *Applied Mechanics Reviews*, 31 (3):277–288, 1978.

[43] S. Guruprasad and A. Mukherjee. Layered sacrificial claddings under blast loading part i — analytical studies. *International Journal of Impact Engineering*, 24(9):957–973, 2000. doi: 10.1016/s0734-743x(00)00004-x.

[44] A. G. Hanssen, L. Enstock, and M. Langseth. Close-range blast loading of aluminium foam panels. *International Journal of Impact Engineering*, 27(6):593–618, 2002. doi: 10.1016/s0734-743x(01)00155-5.

[45] G. S. Langdon, D. Karagiozova, M. D. Theobald, G. N. Nurick, G. Lu, and R. P. Merrett. Fracture of aluminium foam core sacrificial cladding subjected to air-blast loading. *International Journal of Impact Engineering*, 37(6):638, 2010.

[46] X. Li, P. Zhang, Z. Wang, G. Wu, and L. Zhao. Dynamic behavior of aluminum honeycomb sandwich panels under air blast: Experiment and numerical analysis. *Composite Structures*, 108:1001–1008, 2014. doi: 10.1016/j.compstruct.2013.10.034.

[47] Y. Ding, Y. Zheng, Z. Zheng, Y. Wang, S. He, and F. Zhou. Blast alleviation of sacrificial cladding with graded and uniform cellular materials. *Materials*, 13(24):5616, 2020. doi: 10.3390/ma13245616.

[48] N. Kambouchev, L. Noels, and R. Radovitzky. Nonlinear compressibility effects in fluid-structure interaction and their implications on the air-blast loading of structures. *Journal of Applied Physics*, 100(6):063519, 2006. doi: 10.1063/1.2349483.

[49] S. K. Maiti, L. J. Gibson, and M. F. Ashby. Deformation and energy absorption diagrams for cellular solids. *Acta Metallurgica*, 32(11):1963–1975, 2006. doi: 10.1016/0001-6160(84)90177-9.

[50] S. Ouellet, D. Cronin, and M. Worswick. Compressive response of polymeric foams under quasi-static, medium and high strain rate conditions. *Polymer Testing*, 25(6):731–743, 2006. doi: 10.1016/j.polymertesting.2006.05.005.

[51] D. Whisler and H. Kim. Experimental and simulated high strain dynamic loading of polyurethane foam. *Polymer Testing*, 41:219–230, 2006. doi: 10.1016/j.polymertesting.2014.12.004.

[52] B. Langhorst, C. Cook, J. Schondel, and H. Chu. Material systems for blast-energy dissipation implast 2010. *International Journal of Impact Engineering*, 2010.

[53] R. Edwin Raj, V. Parameswaran, and B. S. S. Daniel. Comparison of quasi-static and dynamic compression behavior of closed-cell aluminum foam. *Materials Science and Engineering: A*, 526(1-2):11–15, 2009. doi: 10.1016/j.msea.2009.07.017.

[54] R. P. Merrett, G. S. Langdon, and M. D. Theobald. The blast and impact loading of aluminium foam. *Materials and Design*, 44:311–319, 2013. doi: 10.1016/j.matdes.2012.08.016.

[55] K. Stöbener, D. Lehmhus, M. Avalle, L. Peroni, and M. Busse. Aluminum foam-polymer hybrid structures (apm aluminum foam) in compression testing. *International Journal of Solids and Structures*, 45(21):5627–5641, 2008. doi: 10.1016/j.ijsolstr.2008.06.007.

[56] M. D. Theobald, G. S. Langdon, G. N. Nurick, S. Pillay, A. Heyns, and R. P. Merrett. Large inelastic response of unbonded metallic foam and honeycomb core sandwich panels to blast loading. *Composite Structures*, 92(10):2465–2475, 2010. doi: 10.1016/j.compstruct.2010.03.002.

[57] M. D. Theobald and G. N. Nurick. Experimental and numerical analysis of tube-core claddings under blast loads. *International Journal of Impact Engineering*, 37(3):333–348, 2010. doi: 10.1016/j.ijimpeng.2009.10.003.

[58] S. Palanivelu, W. Van Paepegem, J. Degrieck, S. De Pauw, J. Vantomme, J. Wastiels, D. Kakogiannis, and D. Van Hemelrijck. Low velocity axial impact crushing performance of empty recyclable metal beverage cans. *International Journal of Impact Engineering*, 38(7):622–636, 2011. doi: 10.1016/j.ijimpeng.2011.02.008.

[59] L. Blanc, T. Schunck, and D. Eckenfels. Sacrificial cladding with brittle materials for blast protection. *Materials*, 14(14):3980, 2021. doi: 10.3390/ma14143980.

[60] R. B. Shinde and K. D. Mali. An overview on impact behaviour and energy absorption of collapsible metallic and non-metallic energy absorbers used in automotive applications. *IOP Conference Series: Materials Science and Engineering*, 346:012054, 2018. doi: 10.1088/1757-899x/346/1/012054.

[61] C. J. Wesselski. Mechanical energy absorber. 1993. URL `https://ntrs.nasa.gov/citations/19940011493`.

[62] D. Taylor and C. C. M. Fluid dampers for applications of seismic energy dissipation and seismic isolation. Technical report, State University of New York at Buffalo, 2010.

[63] M. Monteiro. Energy dissipation systems for buildings. Technical report, Department of Civil Engineering, Architecture and Georesources, Instituto Superior Técnico, Technical University of Lisbon, 2011. https://fenix.tecnico.ulisboa.pt/downloadFile/395143135967/Extended

[64] D. Taylor. Fluid dampers for applications of seismic energy dissipation and seismic isolation. *Eleventh World Conference on Earthquake Engineering*, 1996. URL `https://www.iitk.ac.in/nicee/wcee/article/11_798.PDF`.

[65] H. Miyamoto and D. Taylor. Structural control of dynamic blast loading. *Advanced Technology in Structural Engineering*, 2000. doi: 10.1061/40492(2000)116.

[66] T. G. Zhang and T. X. Yu. A note on a 'velocity sensitive' energy-absorbing structure. *International Journal of Impact Engineering*, 8(1):43–51, 1989. doi: 10.1016/0734-743X(89)90030-4.

[67] T. Y. Reddy, S. Reid, and R. G. Barr. Experimental investigation of inertia effects in one-dimensional metal ring systems subjected to end impact — i. fixed-ended systems. *International Journal of Impact Engineering*, 1(1):85–106, 1983. doi: 10.1016/0734-743x(83)90014-3.

[68] L. L. Tam and C. R. Calladine. Inertia and strain-rate effects in a simple plate-structure under impact loading. *International Journal of Impact Engineering*, 11(3):349–377, 1991. doi: 10.1016/0734-743x(91)90044-g.

[69] X. Y. Su, T. X. Yu, and S. R. Reid. Inertia-sensitive impact energy-absorbing structures part ii: Effect of strain rate. *International Journal of Impact Engineering*, 16(4):673–689, 1995. doi: 10.1016/0734-743x(94)00062-2.

[70] X. Y. Su, T. X. Yu, and S. R. Reid. Inertia-sensitive impact energy-absorbing structures part i: Effects of inertia and elasticity. *International Journal of Impact Engineering*, 16(4):651–672, 1995. doi: 10.1016/0734-743x(94)00061-z.

[71] B. Han, L. Yan, B. Yu, Q. Zhang, C. Chen, and T. Lu. Collapse mechanisms of metallic sandwich structures with aluminum foam-filled corrugated cores. *International Journal of Impact Engineering*, 9(4):397–425, 2014. doi: 10.2140/jomms.2014.9.397.

[72] A. Škrlec and J. Klemenc. Estimating the strain-rate-dependent parameters of the cowper-symonds and johnson-cook material models using taguchi arrays. *Journal of Mechanical Engineering*, 62(4):220–230, 2016. doi: https://doi.org/10.5545/sv-jme.2015.3266.

[73] N. K. Singh, E. Cadoni, M. Singha, and N. Gupta. Mechanical behavior of a structural steel at different rates of loading. *Springer eBooks*, pages 859–868, 2012. doi: 10.1007/978-81-322-0757-3_57.

[74] S. T. Marais, R. B. Tait, T. J. Cloete, and G. N. Nurick. Material testing at high strain rate using the split hopkinson pressure bar. *Latin American Journal of Solids and Structures*, 1(3):219–339, 2004. doi: 10.1007/978-81-322-0757-3_57. URL `https://www.lajss.org/index.php/LAJSS/article/view/53`.

[75] E. Markiewicz, P. Ducrocq, and P. Drazetic. An inverse approach to determine the constitutive model parameters from axial crushing of thin-walled square tubes. *International Journal of Impact Engineering*, 21(6):433–449, 1998. doi: 10.1016/s0734-743x(98)00004-9.

[76] G. Belingard, G. Chianduss, and A. Ibba. Identification of strain-rate sensitivity parameters of steel sheet by genetic algorithm optimisation. *WIT Press*, pages 201–210, 2006. doi: 10.2495/HPSM060211.

[77] W. K. Rule. A numerical scheme for extracting strength model coefficients from taylor test data. *International Journal of Impact Engineering*, 19(9-10):797–810, 1997. doi: 10.1016/s0734-743x(97)00015-8.

[78] A. Mauko, B. Nečemer, and Z. Ren. Inverse computational determination of johnson-cook parameters using the shpb test apparatus. *Acta Polytechnica CTU Proceedings*, 25(18):64–67, 2019. doi: 10.14311/app.2019.25.0064.

[79] T. Trzepiecinski and H. G. Lemu. Effect of lubrication on friction in bending under tension test-experimental and numerical approach. *Metals*, 10(4):544, 2020. doi: 10.3390/met10040544.

[80] Q. Lian, C. Yang, and J. Cao. Experimental study on the transition between static and kinetic frictions of steel/shale pairs. *Shock and Vibration*, 2021, 2021. doi: 10.1155/2021/2764803.

[81] T. J. Barrett and M. Knezevic. Modeling material behavior during continuous bending under tension for inferring the post-necking strain hardening response of ductile sheet metals: Application to dp 780 steel. *International Journal of Mechanical Sciences*, 174:105508, 2020. doi: 10.1016/j.ijmecsci.2020.105508.

[82] O. Atoui, A. Maazoun, B. Belkassem, A. Jonet, L. Pyl, and D. Lecompte. Numerical investigation of aluminium plates subjected to blast loading using arbitrary lagrangian eulerian and lagrangian approaches. *SILOS proceedings (13th Shock and Impact Loads on Structures 2019)*, pages 155–164, 2019. URL https://cris.vub.be/ws/portalfiles/portal/49564227/ATOUI_OUSSAMA_SILOS_CONFERENCE_PAPER.pdf.

[83] A. Aminou, B. Belkassem, O. Atoui, D. Lecompte, and L. Pyl. Numerical modeling of brittle mineral foam in a sacrificial cladding under blast loading: Congrès français de mécanique cfm 2022. *Vrije Universiteit Brussel*, 67(3):4540–4550, 2022. URL https://researchportal.vub.be/en/publications/numerical-modeling-of-brittle-mineral-foam-in-a-sacrificial-cladd.

[84] D. A. Braz. Brittle mineral foam in a sacrificial cladding solution for blast loading mitigation. Masters dissertation, AM - Academia Militar, 10 2022.

[85] *LS-DYNA ® KEYWORD USER'S MANUAL VOLUME II Material Models*. LIVERMORE SOFTWARE TECHNOLOGY CORPORATION (LSTC), ls-dyna r10.0 edition, 2017.

[86] C. V. Nielsen, B. N. Legarth, C. F. Niordson, and N. Bay. A correction to the analysis of bending under tension tests. *Tribology International*, 173:107625, 2022. doi: 10.1016/j.triboint.2022.107625.

[87] D. Wiklund, B.-G. Rosén, and A. Wihlborg. A friction model evaluated with results from a bending-under-tension test. *Tribology International*, 42(10):1448–1452, 2022. doi: 10.1016/j.triboint.2009.05.008.

[88] P. Groche and G. Nitzsche. Reduction of friction in deep drawing of aluminium alloys by generating local hydrostatic-pressure lubrication. *Proceedings of the Institution of Mechanical Engineers, Part B: Journal of Engineering Manufacture*, 2006. doi: 10.1243/095440505x32391.

[89] *LS-DYNA ® KEYWORD USER'S MANUAL VOLUME I August 2012 Version 971 R6.1.0 LIVERMORE SOFTWARE TECHNOLOGY CORPORATION (LSTC).* Livermore Software Technology Corporation, version 971 r6.1.0 edition, 2012. https://www.dynamore.de/en/downloads/manuals/ls-dyna-manuals/R6.1.0-Vol1.

[90] L. Malag and L. Kukiełka. Numerical analysis of the states of deformation and stress in the compact tension specimen (ct). *Proceedings in applied mathematics and mechanics*, 8(1):10443–10444, 2008. doi: 10.1002/pamm.200810443.

[91] K. Niklas and A. Bera. The influence of selected strain-based failure criteria on ship structure damage resulting from a collision with an offshore wind turbine monopile. *Polish Maritime Research*, 28(4):42–52, 2021. doi: 10.2478/pomr-2021-0048.

[92] M. Grazka, M. Klosak, W. Mocko, and L. Kruszka. Perforation analysis of s235 steel sheets up to 573 k using experimental and numerical methods. *Archives of Civil Engineering*, 67(3):639–659, 2021. doi: 10.24425/ace.2021.138075.

[93] W.-. C. Limited. Wd-40. https://wd40.pt/, 2023.

Appendix A

Experimental data available

Experimental data available related to the quasi-static tests performed by José Basto for the UFBD.